UNIVERSITY OF SOUTHAMPTON

Faculty of Engineering and Physical Sciences

EPSRC Centre for Doctoral Training in Next Generation Computational Modelling

Multimodal Simulations of Fibre Optical Parametric Amplifiers and Oscillators

by

Ioannis Begleris

ORCID ID 0000-0003-0702-3101

Thesis for the degree of Doctor of Philosophy

February 2020

"The most important step a man can take, it's not the first one is it? It's the next one. Always the next step." From Oathbringer by Brandon Sanderson.

"The same stands for fibre optical parametic oscillators." Ioannis Begleris.

UNIVERSITY OF SOUTHAMPTON

ABSTRACT

FACULTY OF ENGINEERING AND PHYSICAL SCIENCES
EPSRC Centre for Doctoral Training in Next Generation Computational Modelling

Doctor of Philosophy

Multimodal Simulations of Fibre Optical Parametric Amplifiers and Oscillators

by Ioannis Begleris

Systems that are capable of converting light between frequencies are attractive since they can produce output at wavelengths other than those provided by conventional laser sources. These wavelength conversion devices can then be utilised in a variety of applications that require light at unconventional frequencies. Such systems are also useful in the telecommunications industry to convert energy between channels within wavelength division multiplexing fibre systems. Furthermore, since the channels of fibres used within telecommunications are being increased by using multi-mode fibres, mechanisms that can convert energy between these modes are also favourable. To seamlessly apply these converters to the telecommunications fibre network and to maintain the advantages that fibres provide it is preferable for the energy conversions to occur within optical fibres.

Fibre optical parametric amplifiers are all-fibre optical systems where the nonlinearity of the materials is utilised for energy conversion between wavelengths and fibre modes. The conversion efficiency of these devices can however be reduced by non-uniformities of parameters along the propagation direction. This adverse effect can though be controlled by enhancing the amplifier system into a fibre optical parametric oscillator. Fibre based amplifiers and oscillators whose purpose is to convert energy between wavelengths and fibre modes are investigated throughout this thesis.

The wavelength and mode conversion within these amplifiers and oscillators occurs when light is transmitted through an optical fibre. Pulse propagation through these devices is numerically simulated throughout this study by using the multi-mode generalised nonlinear Schrödinger equation. This model is therefore used to investigate wavelength and mode conversion. Furthermore, the frequency banded generalised nonlinear Schrödinger equation is derived and validated as part of this study. This equation allows the effective and accurate simulation of wavelength conversion over ultra-large bandwidths.

Numerical methods that describe the fibre optical parametric amplifiers and oscillators are detailed throughout this thesis. These highly optimised models are then simulated

over a multitude of parameters to calculate the efficiency and noise of the parametric systems. Initially, mode conversion using a multi-mode fibre optical parametric amplifier is investigated. Attention is then drawn upon the operation and inner workings of a single-mode fibre optical parametric oscillator. Finally, the research study culminates with the, to the best of the author's knowledge, first investigation into a multi-mode fibre optical parametric oscillator whose purpose is to convert energy between modes.

Contents

List of Figures

List of Tables

UNIVERSITY OF Southampton

Academic Thesis: Declaration Of Authorship

I, Ioannis Begleris declare that this thesis and the work presented in it are my own and has been generated by me as the result of my own original research.

Multimodal Simulations of Fibre Optical Parametric Amplifiers and Oscillators

I confirm that:

1. This work was done wholly or mainly while in candidature for a research degree at this University;
2. Where any part of this thesis has previously been submitted for a degree or any other qualification at this University or any other institution, this has been clearly stated;
3. Where I have consulted the published work of others, this is always clearly attributed;
4. Where I have quoted from the work of others, the source is always given. With the exception of such quotations, this thesis is entirely my own work;
5. I have acknowledged all main sources of help;
6. Where the thesis is based on work done by myself jointly with others, I have made clear exactly what was done by others and what I have contributed myself;
7. Parts of this work have been published. These publications are listed in Appendix A.

Signed: .....

Date: .....

Acknowledgements

Before undertaking the PhD, I was not aware of how vital the supervisor was for the completion of a thesis. I want to express my sincere gratitude to Dr Peter Horak for his supervision and support throughout all these years. Never was I turned away when I had questions, and he always went the extra mile for me and the research project. His patience and guidance throughout these years where invaluable and without him this thesis would not be what it is today. I would also like to thank Dr Massimilanno Guassoni for his input and help. Even though he became part of my supervision team in the later years of this PhD project his contribution was pivotal to the completion of this work.

I would like to express my appreciation to Hans Fanghour for teaching me Python in the first week of this PhD and continuously trying to get me to adopt correct software practices. These have been invaluable not just during this research but also in my career afterwards.

I want to thank my family for their support. To my father who got me fixing computers over summer vacations where I would have rather done other things. I didn't realise it at the time, but the foundations for the problem solving skills used during this thesis were created there. To my mother for supporting me no matter what, I always felt it was alright to fail because of her support, and somehow this made everything easier to deal with. Also to Konstantina and Iliana for showing me there is more to life than a thesis, I promise I will implement this now.

I would also like to thank Dong Wu for her support throughout the writing and completion of this thesis. She was able to help me unwind and also never turned me away when I kept talking about oscillators.

I want to express my gratitude to Lieke Van Putten (and Nell) for their support through over some of the bleakest days of this PhD. Their ability to make me laugh while I was chasing a bug is something I will always be grateful for. Emergency cookies were also beneficial.

I would also like to thank Sarah Ashleigh Moore for her support throughout the years of this PhD.

Last but not least I would like to thank all my friends for their support throughout all these years. Sometimes even listening to me talk about my research was helpful.

Chapter 1

Introduction

1.1 Motivation

Optical fibres are typically glass wires that have a small, hundred of micron thin, diameter where light can be propagated through the core of that fibre. Their ability to transmit light over kilometres with an attenuation of around 0.2 dB/km has made their application attractive to telecommunications [1]. Their utilisation within this industry has contributed to the expansion and wide adoption of the internet in recent decades [2]. Furthermore, these fibres allow data to be transmitted through them at the speed of light, and this has aided in the increase of internet connection speeds over the past decades. Fibres used within telecommunications have relatively small optical power transmitted through them, typically of the order of milliwatts.

Optical fibres have also been utilised in fibre lasers systems where high output powers (typically of the order of kilowatts) are propagated through the fibre [3]. Fibre lasers are systems where a gain medium is doped into the optical fibre. The desired output of the laser is then amplified as the waves propagate within that fibre. The mechanical flexibility that fibres provide allows the laser to be movable, which can be beneficial to manufacturing applications [4, 5]. Furthermore, long doped fibres can be fabricated over kilometres and thus high gain can be achieved throughout those lengths. Also, the surface area of the fibre allows for cooling of the material. This limits the heat damage done to the laser and allows higher optical power to be passed through it. While these benefits are favourable to the application of high power fibre laser to the manufacturing sector [3] and medical applications [6] their function is limited to the spectral range that their gain medium operates in. Therefore systems that can convert the high output power from the operational bandwidth of the laser to other wavelengths are required.

Optical wavelength conversion can be achieved with a number of methods. One of these is the optoelectronic approach where the optical energy is converted into electronic. The

desired signal is then amplified, reconverted into the optical domain and retransmitted. This approach, however, can be inefficient since optical power needs to be converted to electric and also high optical powers can be detrimental to the optoelectronic converters [3]. Furthermore, these devices require microseconds to perform the amplification of the optical pulse. This is very large when compared to the time required by an all-optical approach that is almost instantaneous [1]. This reduces the applicability of these converters for the telecommunications industry since this time is added to the latency of the data packets. An all-optical approach that is used to convert energy between wavelengths is frequency-mixing within nonlinear crystals [7]. Within these crystals, the nonlinear effect of the material is used to achieve the conversion. Their application to fibre systems is however limited since losses occur when light is coupled between the nonlinear crystal and the fibre. An all-optical and all-fibre approach is achieved by using Raman amplifiers. These systems are used for wavelength conversion within the fibre and like the nonlinear crystals operate using the nonlinear effect of the material [8]. The operational bandwidth of these amplifiers, however, is subject to the Raman gain bandwidth of the material used and therefore limits the range where wavelength conversion can occur.

An alternative nonlinear effect that is used for wavelength conversion within a fibre is Four Wave Mixing (FWM). The systems that use FWM for wavelength conversion are termed in the literature (and within this thesis) as Fibre Optical Parametric Amplifiers (FOPA). A low noise (as low as 0 dB [9]) output characterises these all-fibre systems and they also allow wavelength conversion to occur over a theoretically infinite bandwidth [10]. Within these amplifiers, when pumps and a signal are propagated through the fibre, under specific configurations, energy is converted from the pumps to the signal and to a wave at another wavelength, the idler. The operational efficiency of these energy conversions, however, is greatly dependent upon the parameters of the fibre. Due to fabrication imperfections, these parameters can vary along the propagation axis of the fibre. This variation reduces the efficiency of the FOPAs and can be detrimental to their applications [11]. To combat this, shorter length fibres with higher input wave powers are used. Alternatively, the refractive index profile of the fibres is designed to enhance the conversion efficiency [10]. In addition to this, the signal wave outputted from the fibre can be recirculated to the start of the fibre, combined with the pump and re-propagated through the same fibre essentially forming a Fibre Optical Parametric Oscillator (FOPO). In such a system, the power of the oscillating signal is amplified at every round trip, and this oscillating wave mediates conversion to the idler that forms the desired output of the system. Because of the build-up of the oscillating wave regimes exist where the signal can be amplified from noise and does not need to be seeded into the oscillator with the pumps. This can be advantageous to the application of FOPOs since laser sources at the required signal wavelength may not be available to seed an equivalent FOPA. Finally, it is worth mentioning that both FOPAs and FOPOs can be

used for wavelength conversion of light that is created from an arbitrary type of laser given that the light can be coupled efficiently into the fibre systems.

As previously mentioned, optical fibres are widely used within the telecommunications industry. The reason they are preferred to copper cables is because they offer fast (at the speed of light), low loss (0.2 dB for silica fibres) and high bandwidth (10 Gbps for single-mode fibres) data transmission over distances larger than a *km* [12]. Over the decades, with the worldwide adoption of the internet to almost every part of society, there has been an ever-increasing demand for high capacity in the optical fibre telecommunication systems [13]. While this need for capacity could be fulfilled by installing ever more fibre optic cables, the cost associated with such a venture makes this approach unfeasible [13].

In addition to installing optical fibres, a substantial amount of research has been conducted on increasing the channels that an individual optical fibre can support [13]. The application of Wavelength Division Multiplexing (WDM) systems where each wavelength is used as a channel has contributed to expanding the capacity of a single fibre [14]. However, the bandwidth where these wavelengths/channels can operate is limited to the telecommunications C band. This is because the widely used Erbium Doped Fibre Amplifier (EDFA) is limited to this bandwidth [15].

The limitation of the operational bandwidth that the EDFAs dictate make the exclusive use of WDM systems insufficient to combat the ever-increasing need for higher data transfers [2]. A way that has been employed to extend the capacity of a fibre further is Space Division Multiplexing (SDM) [16]. In this approach, data is encoded in the transverse spatial coordinates which can multiply the channels supported by a WDM system [17]. Two types of fibres are used for such systems, multi-core and multi-mode fibres. The first type has multiple cores fabricated within the fibre with light being transmitted through each core [18]. The multi-mode fibres, on the other hand, have data encoded into the modes of the fibre [19]. Both these SDM systems are required to operate in conjunction with WDM systems in order for them to increase the capacity of single optical fibres. Therefore systems are required that are capable of converting energy between the spatial and wavelength channels.

As stated above, FOPAs can be used as fibre systems capable of converting energy between wavelengths. Multi-Mode Fibre Optical Parametric Amplifiers (MM-FOPA) have also recently been used to convert energy between wavelengths and modes within the telecommunication C band [20, 21]. Furthermore, the non-uniformity of the fibre parameters along the propagation direction of the fibre has been shown to reduce the efficiency of MM-FOPAs [22]. Therefore, for the same reasons as stated above, Multi-Mode Fibre Optical Parametric Oscillators (MM-FOPO) could be considered as potential systems for efficient wavelength and mode conversion within the telecommunication industry. Additionally, MM-FOPAs and MM-FOPOs could be used to generate ad-hoc spatial beams whose shape is different from that of the conventional fundamental mode. This

will allow these systems to be applied to laser applications that may take advantage of non-uniform beam shapes.

Wavelength conversion within optical fibres is not only attractive within the telecommunications industry. As stated earlier, specific applications may require light at wavelengths other than those that the gain medium operates within. Additionally, wavelength conversion over a tunable range may be called for in some use cases. An example of this is coherent anti-Stokes Raman scattering spectroscopy where highly tunable lasers are used to map the chemical compounds of specimens [23]. The tunability that FOPAs and FOPOs provide make them attractive to such application.

Along with analytical and experimental research, computational modelling has been used as a method to investigate optical systems. These numerical methods are regularly used as a connection between analytical models and experimental results. By utilising this link, experimental results can be validated against the underlying theory and *vice versa*. Numerical studies can also be conducted independently of experimental ones. In such investigations, the mathematical methods that describe physical processes are used to create a numerical method capable of simulating the system of interest. The increase in low-cost computational power seen in recent decades also allows the inexpensive, swift and accurate simulation of these computational models over multiple parameters. These models can also be more versatile than experimental studies on equivalent systems. For example, during numerical investigations on optical fibres, the geometry of the system can be easily altered allowing for conclusions to be drawn at a relatively short time and minimal cost. Such an investigation would be a challenge to accomplish with an equivalent experimental study. Furthermore, numerical studies can have a bird's eye view of the entire system that is investigated. Therefore results and conclusions can be drawn from the entirety of the apparatus that is simulated. This feature makes computational modelling an attractive research method for investigating closed systems like FOPOs.

1.2 Research Achievements of this Thesis

As described in the previous section the capacity of the optical fibres that are used in the telecommunications industry can be extended by using multi-mode fibres. MM-FOPAs have been identified as all-fibre systems that can convert the energy between modes and wavelengths. Within this thesis, the efficiency of such conversions within a Two Mode Fibre (TMF) is characterised for varying pump and signal wavelengths. This study was done in conjunction with Dr Francesca Parmigiani and Dr Søren Friis who oversaw the experimental part of the research. In conjunction with the experimental investigation, a numerical model capable of simulating pulse propagation through the fibre was implemented by the author of this thesis. The model was then validated

against the experimental results that were provided. Furthermore, the model was used to find the signal bandwidth where the Conversion Efficiency (CE) remains relatively high. Finally, the physical principles behind the variation of the CE were identified and are presented in this thesis.

Pulse propagation through an optical fibre is usually simulated using the Generalised Nonlinear Schrödinger Equation (GNLSE) [9]. The equation incorporates dispersive and nonlinear interactions due to the Kerr and Raman effects. This equation, however, is not suitable for simulating these effects between narrowband waves that are separated over large bandwidths. This is because a fine frequency grid is required to accurately resolve the narrowband waves, but the Fast Fourier Transform (FFT) (which is used to solve the GNLSE) requires uniform spacing over the entire frequency range, thus leading to an unfeasibly large number of grid points. As a result, this limits the bandwidth where wavelength conversion can be simulated. To address this, Coupled Nonlinear Schrödinger Equations (CNLSE) are used where the bandwidth is split into small frequency bands that incorporate the waves of interest while neglecting the frequencies between them. Nonlinear and dispersive interactions are then simulated between those bands. Therefore, simulations of wavelength conversion over any bandwidth becomes feasible through this approach. However, studies that use these equations either did not incorporate the Raman interaction between the waves, specified that the frequency bands needed to be equally spaced from each other or required the model to operate with a non-depleted pump [24]. As is illustrated later within this thesis not incorporating the Raman interaction between the frequency bands can result in inaccurate results. Additionally, requiring the waves frequency bands to be spaced equally from each-other or the pumps to be undepleted reduces the applicability of the CNLSEs. This challenge was addressed as part of this research project by the derivation and validation of the Banded Nonlinear Schrödinger Equation (BNLSE) that incorporates Raman interaction, allows the frequency bands to be spaced arbitrarily in the frequency domain and is also not confined by the undepleted pump approximation. This equation is then further used to simulate the pulse propagation section of a FOPO in later chapters.

As stated earlier FOPOs could be considered as alternatives to FOPAs as fibre systems for wavelength conversion. While various experimental studies have been conducted that investigate Single-Mode Fibre Optical Parametric Oscillators (SM-FOPO) not many numerical studies are found within the field. In this thesis, an extensive part of the research is focused upon modelling and simulating such an all-fibre SM-FOPO. The optical system along with the numerical method capable of simulating it were conceived and are detailed and validated within this thesis. The model is then used to simulate energy conversion between wavelength hundreds of nanometres apart. By making use of the model, each part of the oscillator could be monitored. For example, the power of the oscillating signal per oscillation is calculated, and it is shown that the power of the output idler is dependent upon that of the signal. The CE of this wavelength

conversion along with the Relative Intensity Noise (RIN) is also calculated for multiple pump powers. Finally, a seeded SM-FOPO is simulated and regimes where high CE and low RIN can be achieved are identified.

The conclusions that are drawn from simulating the SM-FOPO are then used in conceiving and simulating, to the best of the author's knowledge, the first MM-FOPO whose purpose is to convert energy between modes. The fibre parameters and inputs of the MM-FOPA simulated previously are used such that the efficiency of the two systems can be compared. The oscillator is simulated to investigate the behaviour of the CE and RIN. In the final part of this research, the length of the fibre is varied, and it is found that the MM-FOPO can produce similar CEs to the MM-FOPA for the same input parameters but by using a smaller fibre. It was also found that as the fibre length decreases the bandwidth where the CE is maintained increases.

All the studies presented in this thesis are numerical and the models that have been created to conduct these investigations have source codes associated with them. These computational models were created by adhering to some principles of software engineering *i.e.* unit-testing, version control, continuous integration *etc.* In the case of the oscillator models in particular, great lengths where taken into minimising their execution time. The source codes that were created and used within this research project have been open sourced and released freely. This is done such that they can be used, in part or fully, in future studies of FOPAs and FOPOs.

1.3 Outline

A large part of the background knowledge that this thesis is based upon is presented in Chapter 2. The chapter is divided into two sections; the first focuses on the theoretical background while the second concentrates upon the computational modelling. Within the first section, Maxwell's equations are used as a starting point to derive the propagation equations for silica fibres. The propagating fibre modes are then introduced before the presentation of the Multi-Mode Generalised Nonlinear Schrödinger Equation (MM-GNLSE) [25]. This equation and its single fibre mode form, the Single-Mode Generalised Nonlinear Schrödinger equation (SM-GNLSE), are the key numerical methods used to simulate pulse propagation within this thesis. Following this, a description of the dispersive and nonlinear phenomena simulated by the MM-GNLSE is given. Both of these physical effects are principal to the operation of the FOPAs and FOPOs described in the rest of the thesis. The second section of this chapter encompasses the fundamental numerical modelling tools and techniques employed within this research. Initially, focus was drawn upon the scientific computing tools utilised throughout this thesis. Following this, the best practices kept throughout scientific software engineering are described. In addition, the symmetrised Split Step Fourier Method (SSFM), which is

the numerical model used to solve the MM-GNLSE throughout this thesis, is presented. Finally, it is shown how the execution times of this model can be reduced by selecting and accelerating the models that encompass it.

Simulations conducted upon a MM-FOPA are presented in Chapter 3. The TMF used within the study facilitates energy conversion between modes and wavelengths. Within the main body of the chapter, the approximations that were taken to simulate pulse propagation through the fibre are initially described. Following this, the operation of the numerical method is presented. Furthermore, the simulated results are compared to those provided by the experimental group to validate the computational model. Finally, the numerical method is used to investigate the behaviour of the CE of the MM-FOPA over a range of wavelengths.

Within Chapter 4 the SM-GNLSE is used to derive an accurate and efficient BNLSE that is capable of simulating nonlinear and dispersive interaction between waves over an ultra-large bandwidth. Throughout the chapter, this equation is validated against the SM-GNLSE by comparing the phase modulation and FWM between the waves. Through this validation, it is shown that incorporating the Raman factors into the model is critical to the accurate simulation of the nonlinear phenomena. Finally, the execution times of the BNLSE and SM-GNLSE are compared, and it is shown that the first can provide the same accuracy as the second for a fraction of the execution time.

As stated earlier the efficiency of FOPAs can be limited by fabrication imperfections along the length of the fibre, and in order to limit this short length fibres need to be utilised. These short fibres can also be part of a FOPO where the recirculation of part of the spectrum could increase the CE. A detailed study of such an optical apparatus is the subject of Chapter 5. The FOPO simulated in this chapter is single mode since the fibre used within it supports one mode over the frequency bandwidth investigated. Within the chapter initially each subsystem that the SM-FOPO is comprised of is presented. Following this, the numerical models capable of simulating the SM-FOPO are described and validated. The numerical method of the oscillator is then simulated for different input pump wavelengths and powers for a single pump input and with the addition of a seed. Finally, CE and the RIN of the oscillator are evaluated for these input parameters and configurations.

In Chapter 6 the pulse propagation model of the TMF described in Chapter 3 is combined and expanded with the conclusions drawn from Chapter 5 to simulate a MM-FOPO. Like in Chapter 3 the motivation behind the apparatus is to convert energy between fibre modes and wavelengths. Within the main body of the chapter, the numerical model used to simulate the optical system is presented. Following this, the behaviour of the CE and RIN of the oscillator are investigated. Finally, the length of the fibre used is varied, and it is shown that high-efficiency mode conversion can occur over a larger bandwidth than an equivalent MM-FOPA.

Conclusions, along with recommendations for future work that this research could lead to are discussed in Chapter 7.

Chapter 2

Fundamentals of Simulating Pulse Propagation within Optical Fibres

This chapter serves as an introduction to the fundamental theoretical and numerical models used in this research. In the first section, the propagation equations for silica fibres are derived from Maxwell's equations. The mathematical reasoning behind key physical processes such as dispersion and nonlinear optics are discussed throughout the derivation. In addition, the model used to describe the propagation of light in fused fibre couplers is derived. Further from this, the principal MM-GNLSE, which forms an essential mathematical basis for the entirety of this thesis, is introduced and its components described. In the second section, the techniques and tools used in producing the scientific software used in this research are presented. Furthermore, special consideration is taken in optimising the numerical method used to solve the MM-GNLSE. In the final section of this chapter, fibre optical parametric converters are discussed and results of noteworthy fibre amplifiers are presented.

2.1 Theoretical Background

2.1.1 Beam Propagation in Optical Fibres

2.1.1.1 Maxwell's Equations

Electromagnetic waves propagating through a non-magnetic dielectric medium like an optical fibre can be described by Maxwell's equations in the form of [9]:

$$\nabla \times \boldsymbol{E} = -\mu_0 \frac{\partial \boldsymbol{H}}{\partial t} \tag{2.1}$$

$$\nabla \times \boldsymbol{H} = \epsilon_0 \frac{\partial \boldsymbol{E}}{\partial t} + \frac{\partial \boldsymbol{p}}{\partial t} \tag{2.2}$$

$$\nabla \cdot (\epsilon_0 \boldsymbol{E} + \boldsymbol{p}) = 0 \tag{2.3}$$

$$\nabla \cdot \boldsymbol{H} = 0 \tag{2.4}$$

where $\boldsymbol{E}$, $\boldsymbol{H}$ and $\boldsymbol{p}$ are the electric, magnetic and polarisation field vectors respectively (the spatial and time dependence has been omitted for clarity). Finally, μ_0 is the magnetic permeability of free space and ϵ_0 the vacuum electric permittivity.

By applying the curl operator upon both sides of (2.1) and substituting (2.2) the propagation equation becomes:

$$\nabla \times \nabla \times \boldsymbol{E} = -\mu_0 \epsilon_0 \frac{\partial^2 \boldsymbol{E}}{\partial t^2} - \mu_0 \frac{\partial^2 \boldsymbol{p}}{\partial t^2}. \tag{2.5}$$

In isotropic and homogeneous materials the assumption can be made that the polarisation vector is proportional to the electric field vector. This results in (2.3) being reduced to $\nabla \cdot \boldsymbol{E} = 0$ [26]. One can then apply the now simplified vector identity $\nabla \times \nabla \times \boldsymbol{E} = -\nabla^2 \boldsymbol{E}$ to (2.5) resulting in the beam propagation equation:

$$\nabla^2 \boldsymbol{E} = \frac{1}{c^2} \frac{\partial^2 \boldsymbol{E}}{\partial t^2} + \mu_0 \frac{\partial^2 \boldsymbol{p}}{\partial t^2} \tag{2.6}$$

where $c = 1/\sqrt{\epsilon_0 \mu_0}$ is the speed of light in vacuum.

2.1.1.2 Polarisation

Light propagating through a material will electromagnetically influence the molecules of the said material. As a consequence, the material will affect the propagating beam. This phenomenon is represented in (2.6) by the polarisation vector. In symmetric materials like silica the polarisation can be described as [9]:

$$\boldsymbol{p}(\boldsymbol{r}, t) = \boldsymbol{p}_L(\boldsymbol{r}, t) + \boldsymbol{p}_{NL}(\boldsymbol{r}, t), \tag{2.7}$$

where the linear part is

$$\boldsymbol{p}_L(\boldsymbol{r}, t) = \epsilon_0 \int_{-\infty}^{\infty} \boldsymbol{\chi}^{(1)}(t - \tau) \boldsymbol{E}(\boldsymbol{r}, \tau) \, d\tau, \tag{2.8}$$

the nonlinear part

$$\begin{aligned}\boldsymbol{p}_{NL}(\boldsymbol{r},t) = \epsilon_0 \int_{-\infty}^{\infty}\int_{-\infty}^{\infty}\int_{-\infty}^{\infty} \boldsymbol{\chi}^{(3)}(t-\tau_1, t-\tau_2, t-\tau_3) \\ \vdots \boldsymbol{E}(\boldsymbol{r},\tau_1)\,\boldsymbol{E}(\boldsymbol{r},\tau_2)\,\boldsymbol{E}(\boldsymbol{r},\tau_3)\,d\tau_1 d\tau_2 d\tau_3\end{aligned} \tag{2.9}$$

and $\boldsymbol{\chi}^{(1)}$, $\boldsymbol{\chi}^{(3)}$ are the first and third order susceptibilities respectively. Both the susceptibilities are tensors. However glasses like silica are amorphous, therefore $\boldsymbol{\chi}^{(1)}$ can be represented as a scalar quantity $\chi^{(1)}$. Additionally in isotropic materials the $\boldsymbol{\chi}^{(3)}$ tensor is reduced to three independent tensor elements. If the electric field vector can be considered proportional to the direction of one of these elements then $\boldsymbol{\chi}^{(3)}$ can also be considered as a scalar quantity $\chi^{(3)}$ [7].

One can identify that (2.8) can also be considered as the convolution of the first order susceptibility and hence the polarisation can be written as:

$$\boldsymbol{p}_L(\boldsymbol{r},t) = \epsilon_0 \chi^{(1)}(t) \otimes \boldsymbol{E}(\boldsymbol{r},t)\,. \tag{2.10}$$

At this stage it is of interest to introduce the physical phenomena that arise from the susceptibilities. Both the first and third order susceptibilities are complex quantities. In particular $\mathrm{Re}\left(\chi^{(1)}\right)$ is related to the dielectric constant of the material and $\mathrm{Im}\left(\chi^{(1)}\right)$ to the material loss. $\mathrm{Im}\left(\chi^{(3)}\right)$ is connected to the two-photon absorbtion which in materials like silica can be neglected [9]. Finally, $\mathrm{Re}\left(\chi^{(3)}\right) = \chi_K^{(3)} + \chi_R^{(3)}$, where the two terms are responsible for the Kerr and Raman nonlinear effects respectively [26].

The Kerr nonlinearity is inherently an electronic phenomenon and can be assumed to be instantaneous allowing the time-dependent part of the Kerr susceptibility to be expressed by a product of Dirac-Delta functions [9]:

$$\chi_K^{(3)}(t-\tau_1, t-\tau_2, t-\tau_3) = \chi_K^{(3)}\delta(t-\tau_1)\,\delta(t-\tau_2)\,\delta(t-\tau_3) \tag{2.11}$$

In contrast to the Kerr nonlinearity, the Raman effect mediates a transfer of energy from the propagating field to the molecules of the medium. By extension, it cannot be considered instantaneous and is affected by a time delay. Hence the Raman part of the nonlinear susceptibility can be expressed as [9, 27]:

$$\chi_R^{(3)}(t-\tau_1, t-\tau_2, t-\tau_3) = \chi_R^{(3)}\delta(t-\tau_3)\,\delta(t-\tau_2)\,h(t-\tau_1)\,, \tag{2.12}$$

where $h(t)$ is the Raman response function.

By applying (2.11), (2.12) to (2.9) the nonlinear polarisation can be expressed as [26]:

$$\boldsymbol{p}_{NL}(\boldsymbol{r},t) = \epsilon_0 \left(\chi_K^{(3)} |\boldsymbol{E}(\boldsymbol{r},t)|^2 + \chi_R^{(3)} \int_{-\infty}^{\infty} h(t-\tau) |\boldsymbol{E}(\boldsymbol{r},\tau)|^2 d\tau \right) \boldsymbol{E}(\boldsymbol{r},t). \tag{2.13}$$

Finally, the integral term in (2.13) forms a convolution as in (2.10) hence the nonlinear polarisation becomes

$$\boldsymbol{p}_{NL}(\boldsymbol{r},t) = \epsilon_0 \left(\chi_K^{(3)} |\boldsymbol{E}(\boldsymbol{r},t)|^2 + \chi_R^{(3)} h(t) \otimes |\boldsymbol{E}(\boldsymbol{r},t)|^2 \right) \boldsymbol{E}(\boldsymbol{r},t). \tag{2.14}$$

2.1.1.3 Beam Propagation Equation

By applying (2.7), (2.10), (2.14) to (2.6) the propagation equation in the time domain is given as:

$$\nabla^2 \boldsymbol{E} = \frac{1}{c^2} \frac{\partial^2}{\partial t^2} \Bigg(\boldsymbol{E}(\boldsymbol{r},t) + \chi^{(1)}(t) \otimes \boldsymbol{E}(\boldsymbol{r},t) + \Big(\chi_K^{(3)} |\boldsymbol{E}(\boldsymbol{r},t)|^2 + \chi_R^{(3)} h(t) \otimes |\boldsymbol{E}(\boldsymbol{r},t)|^2 \Big) \boldsymbol{E}(\boldsymbol{r},t) \Bigg). \tag{2.15}$$

Each term within the parentheses of (2.15) adds extra complexity to the light propagation within the medium. If the susceptibilities are disregarded then the equation is reduced to free space propagation. The linear susceptibility introduces the concept of the linear, with respect to the electric field, reaction of the material to the propagation of light. In particular, the frequency-dependent linear dielectric constant of the material is defined by [9]:

$$\epsilon(\omega) = 1 + \chi^{(1)}(\omega). \tag{2.16}$$

As previously mentioned $\chi^{(1)}(\omega)$ is complex where the real part is related to the refractive index of the material and the imaginary part to the extinction of light throughout propagation. The relation is defined by

$$\epsilon(\omega) = (n(\omega) + j\psi(\omega))^2, \tag{2.17}$$

where $n(\omega)$ is the refractive index and $\psi(\omega)$ the extinction coefficient of the material.

The speed of light within a material is dependent upon the refractive index. As can be seen in (2.17) the refractive index depends on frequency. This leads to waves at different frequencies propagating at different speeds within the medium. This phenomenon is known as chromatic dispersion and is discussed further in Section 2.1.5.

The last term in the propagation equation has the distinction of the nonlinear dependence on the modulus square of the electric field. In other words, the magnitude of its effect is proportional to the intensity of the field. As discussed earlier the third order susceptibilities are considered real in silica fibres. Hence this nonlinear term will apply an intensity dependent change upon the refractive index of the material. In particular one can write this nonlinear effect upon the refractive index as:

$$\tilde{n} = n + n_2 \left|\boldsymbol{E}\right|^2, \tag{2.18}$$

where n_2 is the nonlinear index of the material. It is this mathematical and by extension physical implication that gives rise to the phenomena primarily exploited throughout this research.

2.1.2 Fibre Modes

The previous section foresaw the investigation of beam propagation within an optical fibre. However, an abstract view was taken on the distribution of the electric field vector within the fibre. In this section, it will be discussed how the geometrical and material properties of the fibre confine light in the transverse direction and how light is distributed into discrete guided fibre modes.

A standard optical fibre is essentially a waveguide whose geometry is circularly symmetric in the transverse direction. In the radial direction, the refractive index of the material varies with usually higher numerical values exhibited in the centre (core). For example, a special case of this is the step-index fibre where there is a discontinuity between the higher core refractive index and that of the cladding. This type of fibre primarily confines light within the core of the fibre and allows it to propagate along the axial direction.

By ignoring the nonlinearity and loss of (2.15) the propagation equation becomes:

$$\nabla^2 \tilde{\boldsymbol{E}} = \frac{\omega^2 n^2 \left(x, y, \omega\right)}{c^2} \tilde{\boldsymbol{E}}, \tag{2.19}$$

where $\tilde{\boldsymbol{E}} \rightarrow \boldsymbol{E}\left(r, \omega\right)$ is the Fourier transform of the electric field vector, ω the angular frequency and the refractive index of the material has been assumed to be uniform along the propagating axis z. Upon the boundaries between media of different refractive index, the tangential components of the electric and magnetic fields must be continuous. Solving (2.19) at a given frequency and imposing these constraints leads to discrete solutions for the electric field. The modes of the fibre are defined as these solutions. In addition, the modes whose electric field tends to zero at $r \rightarrow \infty$ are called guided modes *i.e.* they are guided along the propagation direction whereas modes who do not exhibit

this attribute are radiative modes. For the purposes of this thesis only guided modes are investigated and they will be referred to as modes hereafter.

The modes are distinguished by both having a different spatial distribution $\boldsymbol{F}(x, y, \omega)$ and by their eigenvalues (propagation constants) β. If as stated earlier the refractive index distribution is uniform along the z-axis then the transverse distribution of the mode will propagate unaltered along the fibre and the mode will experience a phase change dependent upon the propagation constant. The electric field can be expressed as a summation of these modes:

$$\tilde{\boldsymbol{E}}\left(x, y, z, \omega\right) = \sum_{n} A_n(z, \omega) \left(\boldsymbol{F}_n\left(x, y, \omega\right) e^{\mathrm{j}\beta_n(\omega) z} \right), \tag{2.20}$$

where $A(z, \omega)$ is the longitudinal propagating amplitude of a mode.

While analytical solutions exist for step-index fibres [19] and for parabolic index fibres, [28] usually numerical methods like Finite Element Methods are used to calculate these modes [29].

The mode distributions, particularly for the purposes of this research, are important when modes nonlinearly interact with each other. The size of the interaction can usually be expressed by the overlap integrals. For interacting modes the overlap integral can be calculated from [9]:

$$\eta_{\mathrm{iklm}} = \frac{\int \left(\boldsymbol{F}_i^* \boldsymbol{F}_k^*\right) \left(\boldsymbol{F}_l \boldsymbol{F}_m\right) dxdy}{\left(\int \left|\boldsymbol{F}_i\right|^2 dxdy \int \left|\boldsymbol{F}_k\right|^2 dxdy \int \left|\boldsymbol{F}_l\right|^2 dxdy \int \left|\boldsymbol{F}_m\right|^2 dxdy \right)^{1/2}}. \tag{2.21}$$

Finally when the overlap integral is calculated for the same mode function (the indices of η are all equal) then this results in the inverse of the effective area of the mode A_{eff}.

2.1.3 Fibre Couplers

As reviewed in the previous section light in optical fibres is confined in the transverse direction by the refractive index profile. In a variety of application, need arises to couple energy between fibres. For example in this research fibre couplers are used in the FOPO systems investigated in Chapter 5 for spectrally dependent optical power recirculation.

There are a plethora of fibre coupler designs available in literature [19]. For the purposes of this study, 2×2 fused fibre couplers are considered. In such a system two optical fibres are fused together over a length of L as shown in Figure 2.1(d). Light is inputted into the fibre coupler from ports 1 and 2. The electric fields from those ports interact over the fused length L and are outputted through ports 3 and 4.

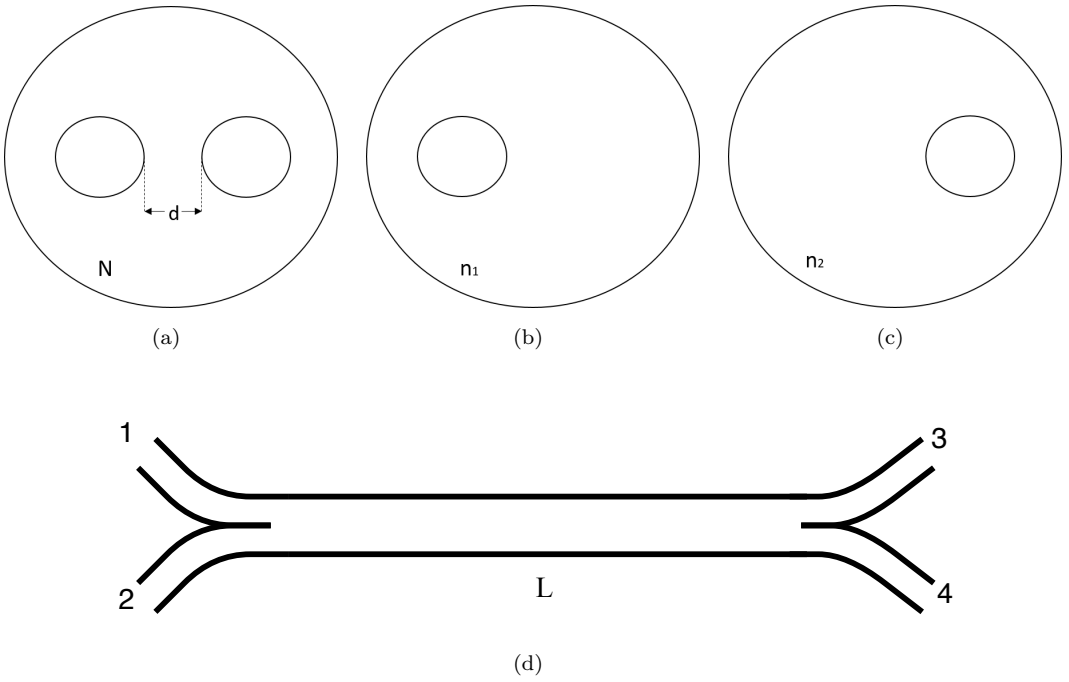

FIGURE 2.1: Fibre coupler apparatus schematics and refractive index profiles. Full refractive index of the fused fibre coupler shown in (a) and the equivalent profiles without the presence of each of the fibre cores (b), (c). The diagram of the fused coupler along fused length L is depicted (d).

.

Within the fused part of the coupler the electric field can be approximated as a sum of the electric field of the two fibres as [19]:

$$\tilde{\boldsymbol{E}}(x,y,z,\omega) = \sum_{i=1}^{2} A_i(z,\omega)\boldsymbol{F}_i(x,y,\omega)e^{\mathrm{j}\beta^{(i)}(\omega)z}, \tag{2.22}$$

where $A_i(z)$ are the propagating amplitudes, $\boldsymbol{F}_i(x,y,\omega)$ the transverse electric field distributions and β_i the eigenvalues for the modes within each fibre.

The electric field of the fused part of the coupler should be a solution of the linear propagation equation for the refractive index profile shown in Figure 2.1(a) as:

$$\nabla^2\left(\sum_{i=1}^{2} A_i(z,\omega)\boldsymbol{F}_i(x,y,\omega)e^{\mathrm{j}\beta^{(i)}z}\right) = \frac{\omega^2 N^2(x,y,\omega)}{c^2}\left(\sum_{i=1}^{2} A_i(z,\omega)\boldsymbol{F}_i(x,y,\omega)e^{\mathrm{i}\beta^{(i)}z}\right). \tag{2.23}$$

In addition each of the $i = 1, 2$ modes should fulfil (2.19) for the equivalent refractive index profiles shown in Figures 2.1(b), 2.1(c) respectively:

$$\nabla^2\left(\boldsymbol{F}_i(x,y,\omega)e^{\mathrm{j}\beta^{(i)}z}\right) = \frac{\omega^2 n_i^2(x,y,\omega)}{c^2}\left(\boldsymbol{F}_i(x,y,\omega)e^{\mathrm{j}\beta^{(i)}z}\right), i = 1,2. \tag{2.24}$$

By expanding (2.23), taking the slowly varying amplitude approximation

$$\frac{\partial^2 A_j}{\partial z^2} \ll \frac{\omega}{c}\frac{\partial A}{\partial z}$$

and asserting (2.24) the coupled equations that describe the propagating amplitudes are shown to be

$$\frac{\partial A_1}{\partial z} = \mathrm{j}\kappa_{12} A_2 e^{\mathrm{i}\Delta z} \qquad (2.25) \qquad\qquad \frac{\partial A_2}{\partial z} = \mathrm{j}\kappa_{21} A_1 e^{-\mathrm{i}\Delta z} \qquad (2.26),$$

where $\Delta = \beta^{(2)} - \beta^{(1)}$, the coupling coefficients are

$$\kappa_{12} = \mathrm{j}\frac{\pi f}{c n_{\mathrm{eff}_1}} \frac{\int \left(N^2 - n_2^2\right) \boldsymbol{F}_1^* \boldsymbol{F}_2 dxdy}{\int |\boldsymbol{F}_1|^2 dxdy}, \qquad (2.27)$$

$$\kappa_{21} = \mathrm{j}\frac{\pi f}{c n_{\mathrm{eff}_2}} \frac{\int \left(N^2 - n_1^2\right) \boldsymbol{F}_1 \boldsymbol{F}_2^* dxdy}{\int |\boldsymbol{F}_2|^2 dxdy}, \qquad (2.28)$$

$n_{\mathrm{eff_i}} = c\beta_i/\omega$ for $i = 1, 2$ are the effective indexes and $f = \omega/2\pi$. The spatial and frequency dependencies have been omitted for clarity.

The coupler could also be made by fusing identical fibres which, assuming the respective cores are smaller than the fused cladding, would lead to $n_{\mathrm{eff}_1} = n_{\mathrm{eff}_2} = n_{\mathrm{eff}}$ and $\Delta = 0$. Disregarding losses, during propagation through the fused part of the coupler the total energy must be conserved, ergo:

$$\frac{\partial}{\partial z}\left(|A_1|^2 + |A_2|^2\right) = 0. \qquad (2.29)$$

Applying (2.25) - (2.26) to (2.29) yields that the coupling coefficients must satisfy $\kappa_{12} = \kappa_{21}^*$. In addition, the coupling coefficient of most couplers can be considered real, therefore $\kappa_{12} = \kappa_{21}^* = \kappa$ [19]. These approximations vastly simplify (2.25) - (2.26) to:

$$\frac{\partial A_1}{\partial z} = \mathrm{j}\kappa A_2 \qquad (2.30) \qquad\qquad \frac{\partial A_2}{\partial z} = \mathrm{j}\kappa A_1 \qquad (2.31).$$

Equations (2.30) - (2.31) can then be analytically solved over the propagating distance z as

$$\begin{pmatrix} A_1(z,\omega) \\ A_2(z,\omega) \end{pmatrix} = \begin{pmatrix} \cos(\kappa z) & \mathrm{j}\sin(\kappa z) \\ \mathrm{j}\sin(\kappa z) & \cos(\kappa z) \end{pmatrix} \begin{pmatrix} A_1(0,\omega) \\ A_2(0,\omega) \end{pmatrix}. \qquad (2.32)$$

Applying (2.32) to the optical coupler model shown in Figure 2.1(d) the output field at ports 3 and 4 can be calculated using:

$$\begin{pmatrix} A_{p3}(\omega) \\ A_{p4}(\omega) \end{pmatrix} = \begin{pmatrix} \cos(\kappa L) & \mathrm{j}\sin(\kappa L) \\ \mathrm{j}\sin(\kappa L) & \cos(\kappa L) \end{pmatrix} \begin{pmatrix} A_{p1}(\omega) \\ A_{p2}(\omega) \end{pmatrix}. \tag{2.33}$$

This expression is known as the Scattering Matrix Representation (SMR) and can be applied to model 2×2 optical fibre couplers [12].

If the variation of the refractive index and mode functions along the longitudinal direction and frequency are ignored then the coupling coefficient is only linearly dependent upon frequency. Since the fused length of the coupler is fixed the spectral variation of the transfer matrix is only frequency dependent. This results in the percentage of optical power outputted at ports 3 and 4 being different for each frequency. Therefore such a system can be used for outputting certain wavelengths to different paths of an optical system and will hereafter be dubbed a WDMC.

2.1.4 Generalised Nonlinear Schrödinger Equations

While (2.15) describes the electric field propagation through a homogeneous optical fibre, it is a three-dimensional propagation equation and is computationally intensive to solve and therefore a simplified approach is needed. As shown previously the electric field propagating through an optical fibre along the z direction can be broken down to individual transverse modes. The electric field can be represented as a summation over modes p as [25]:

$$\boldsymbol{E}(x,y,z,t) = \sum_p \int Re\left[\frac{\boldsymbol{F}_p(x,y,\omega)}{N_p(\omega)} e^{j\left(\beta^{(n)}(\omega)-\omega t\right)} A_p(z,\omega)\right] d\omega, \tag{2.34}$$

where $N_p(\omega)$ is mode normalisation and $A_p(z,\omega)$ the propagating envelope.

Applying (2.34) to (2.15) (and after some algebraic manipulation) results in the MM-GNLSE [25]:

$$\frac{\partial A_p(z,t)}{\partial z} = \mathcal{D}_p(z,t) + \mathcal{N}_p(z,t), \tag{2.35}$$

where $\mathcal{D}_p(z,t)$ and $\mathcal{N}_p(z,t)$ are the dispersion and nonlinear functions respectively.

The dispersion term can be calculated using [25]:

$$\mathcal{D}_p(z,t) = j(\beta_0^{(p)} - \beta_0)A_p(z,t) - \frac{\alpha}{2}A_p(z,t) - (\beta_1^{(p)} - \beta_1)\frac{\partial A_p(z,t)}{\partial t} + j\sum_{n\geq 2}\frac{\beta_n^{(p)}}{n!}\left(j\frac{\partial}{\partial t}\right)^n A_p(z,t). \tag{2.36}$$

Within this expression, the term α represents the attenuation of the fibre related to the extinction coefficient shown in (2.17). The dispersion is also primarily dependent upon the propagation constants of the mode p. In particular $\beta_n^{(p)}$ represents the n^{th} Taylor expansion coefficients around reference angular frequency ω_0 and β_0, β_1 are usually taken as the equivalent expansion coefficients of one particular mode. The physical significance of the coefficients is discussed further in Section 2.1.5.

The nonlinear term is given by [25]:

$$\begin{aligned}\mathcal{N}_p(z,t) = j\frac{n_2\omega_0}{c}\sum_{l,m,n}\Bigg[&\left(1 + j\tau_{plmn}^{(1)}\frac{\partial}{\partial t}\right)Q_{plmn}^{(1)}(\omega_0)\,2A_l(z,t)\times \\ &\int R(\tau)A_m(z,t-\tau)A_n^*(z,t-\tau)d\tau + \left(1 + j\tau_{plmn}^{(2)}\frac{\partial}{\partial t}\right)Q_{plmn}^{(2)}(\omega_0)\,A_l^*(z,t) \\ &\int R(\tau)\,A_m(z,t-\tau)A_n(z,t-\tau)e^{2j\omega_0\tau}d\tau\Bigg]\end{aligned} \tag{2.37}$$

where the shock time constants are

$$\tau_{plmn}^{(1,2)} = \frac{1}{\omega_0} + \left[\frac{\partial}{\partial\omega}ln\left(Q_{plmn}^{(1,2)}(\omega)\right)\right], \tag{2.38}$$

the Q factors are found by:

$$Q_{plmn}^{(1)} = \frac{\epsilon_0 n_0^2 c^2}{12}\frac{\int\left(\boldsymbol{F}_p^*(x,y,\omega)\cdot\boldsymbol{F}_l(x,y,\omega)\right)\left(\boldsymbol{F}_m(x,y,\omega)\cdot\boldsymbol{F}_n^*(x,y,\omega)\right)dxdy}{N_p(\omega)\,N_l(\omega)\,N_m(\omega)\,N_n(\omega)}, \tag{2.39}$$

$$Q_{plmn}^{(2)} = \frac{\epsilon_0 n_0^2 c^2}{12}\frac{\int\left(\boldsymbol{F}_p^*(x,y,\omega)\cdot\boldsymbol{F}_l^*(x,y,\omega)\right)\left(\boldsymbol{F}_m(x,y,\omega)\cdot\boldsymbol{F}_n(x,y,\omega)\right)dxdy}{N_p(\omega)\,N_l(\omega)\,N_m(\omega)\,N_n(\omega)} \tag{2.40}$$

and n_0 is the refractive index of the core material the modes are propagated in. The nonlinear time response shown here is set to incorporate both the Kerr and Raman effects and is found by

$$R(t) = (1 - f_R)\,\delta(t) + \frac{3}{2}f_R h(t), \tag{2.41}$$

where f_R is the fraction contribution of the Raman effect to the total third order nonlinearity and $h(t)$ the Raman response function. The next subsections discuss the physical interpretation of each of the effects the MM-GNLSE simulates.

2.1.5 Dispersion

The propagation constants of fibre modes provide a plethora of information regarding the propagating wave. However, in many practical situations, the refractive index profile of the fibre is unknown which results in the inability to explicitly calculate these eigenvalues. In these cases, parameters related to the eigenvalue can usually be measured by experimental means. To highlight these parameters β is expanded around a reference frequency ω_0.

$$\beta^{(p)}(\omega) = \beta_0^{(p)} + \beta_1^{(p)}(\omega - \omega_0) + \beta_2^{(p)}(\omega - \omega_0)^2 + \beta_3^{(p)}(\omega - \omega_0)^3 \ldots \tag{2.42}$$

where

$$\beta_n^{(p)} = \left.\frac{d^n \beta^{(p)}}{d\omega^n}\right|_{\omega=\omega_0}. \tag{2.43}$$

The coefficient $\beta_1^{(p)}$ is inversely proportional to the group velocity. This represents the speed at which the pulse envelope propagates through the medium. $\beta_1^{(p)}$ is also dependent upon frequency which results in distinct frequencies of a pulse propagating at different speeds. The derivative of $\beta_1^{(p)}$ is the Group Velocity Dispersion (GVD) parameter $\beta_2^{(p)}$. If it is positive then lower frequencies travel at a lower velocity. This is termed normal dispersion. On the other hand, if it is negative then lower frequencies travel at higher speeds and this is called anomalous dispersion. The wavelength where $\beta_2^{(p)}$ is zero is termed the zero dispersion wavelength. However, this does not necessarily mean that the total dispersion of the waveguide is zero. In this case higher order terms play a dominant role in the calculation of the dispersion [9].

The eigenvalues of the modes $\beta^{(p)}$ are usually different for each mode. This in turn leads to these different modes exhibiting different $\beta_n^{(p)}$ coefficients. This is known as modal dispersion. For example, different modes can travel at different speeds within the fibre and this can prove problematic in applications where the time of arrival of modes is paramount.

Finally, the expansion coefficients are sometimes provided in units of wavelength. Hence it is useful to write down the conversion between wavelength and frequency units.

Around a central wavelength λ_0 [9]:

$$\beta_2(\omega_0) = \frac{-\lambda_0^2}{2\pi c} D, \tag{2.44}$$

$$\beta_3(\omega_0) = \frac{\lambda_0^4}{4(\pi c)^2} S + \frac{\lambda_0^3}{2(\pi c)^2} D, \tag{2.45}$$

where the dispersion coefficient and dispersion slope are defined as

$$D = \left.\frac{d\beta_1}{d\lambda}\right|_{\lambda=\lambda_0}, S = \left.\frac{d^2\beta_1}{d\lambda^2}\right|_{\lambda=\lambda_0}. \tag{2.46}$$

2.1.6 Kerr Effects

At high intensities along with dispersion phenomena, nonlinear processes due to the instantaneous Kerr part of $\chi^{(3)}$ become significant. The nonlinear effect can be interpreted as the intensity-dependent change in the refractive index of the material as seen in (2.18). This in turn results in the nonlinear refraction of the pulse propagating through the optical fibre. This phenomenon is responsible for the intensity-dependent modification of the propagating pulse discussed in this subsection.

The first influence applies an intensity dependent perturbation to the group velocity owing to dispersion [9]. This is described in the MM-GNLSE by (2.38) and can result in asymmetric pulse broadening particularly for a pulse that is distributed over a large frequency bandwidth.

A wave propagating through a fibre can also, through the Kerr nonlinearity, induce a nonlinear phase shift upon itself called Self Phase Modulation (SPM). This can cause broadening of the pulse spectrum. Furthermore, when multiple spectral waves are propagating within the same medium the modification of the refractive index by one induces a phase shift upon other waves propagating within the medium. This process is labelled Cross Phase Modulation (XPM).

The final and most paramount effect to this research is the process of FWM. The essence of this is the transfer of energy between wavelengths and modes within a fibre. Figure 2.2(a) shows the most common FWM process. Two pumps and a signal, set at separate frequencies, are inputted into the fibre. As they propagate, power is transferred from the pumps to the signal and also a fourth idler wave is created at a frequency of:

$$\omega_i = \omega_{p_1} + \omega_{p_2} - \omega_s, \tag{2.47}$$

where ω_{p_1}, ω_{p_2} are the first and second pump frequencies and, ω_s is the signal frequency. The efficiency of the process depends upon the nonlinear coefficient of the fibre n_2,

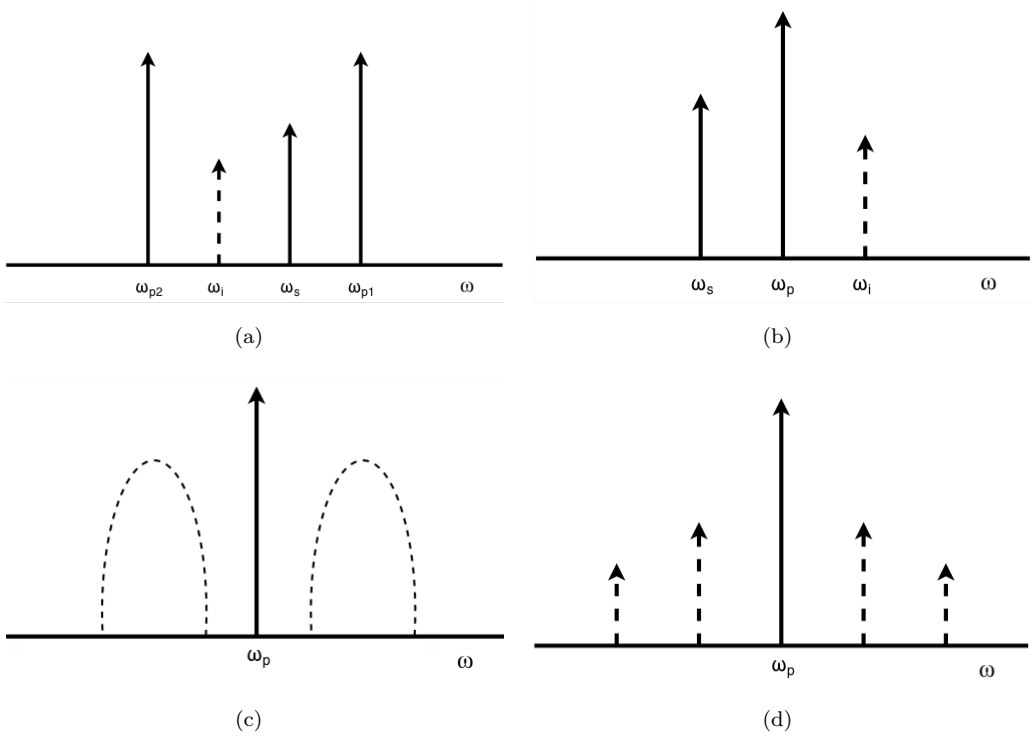

FIGURE 2.2: Four wave mixing (FWM) diagrams showing the input (full lines) and generated (dashed lines) waves. In particular, the figures show: a) seeded FWM, b) degenerate FWM, c) modulation instability, d) cascade FWM

.

the input power of the waves involved and finally upon the phase-mismatch parameter defined as:

$$\Delta\beta = \beta_s(\omega_s) + \beta_i(\omega_i) - \beta_{p_1}(\omega_{p_1}) - \beta_{p_2}(\omega_{p_2}), \tag{2.48}$$

where β are the propagation constants of the respective waves. The smaller the magnitude of the parameter $\Delta\beta$ is the more efficient the process is.

Contrary to the term FWM it is not necessary to have four waves for energy to be transferred. The definition stems from the fact that four photons are involved in the process [10]. Figure 2.2(b) shows what is termed in literature as Degenerate FWM. In this case, a single pump is depleted to transfer energy from the pump to the signal and the newly formed idler. Equations (2.47), (2.48) are then modified by taking $\omega_{p_1} = \omega_{p_2}$ and $\beta_{p_1} = \beta_{p_2}$. Likewise, as is shown in Figure 2.2(c) there is no need for the signal to be inputted into the fibre for FWM to occur. The signal and the idler can, in fact, be amplified from the noise that exists within a medium. In this case, side-bands in the frequency domain are amplified; the size and position of which primarily dependent upon the magnitude of the phase-mismatch parameter $|\Delta\beta(\omega)|$.

It is useful to mention that the labels of pump, signal and idler are set within the literature as convention and can form a misguided view that power transfer only occurs from a strong pump to weaker signals and idlers. In fact, any wave regardless of the

power can act as a pump, signal or idler. This can lead to multiple waves being created within the spectrum which, in turn, can form FWM partners with the already existent waves. A prime example of this is shown in Figure 2.2(d). After the signal is created it acts as a pump with the original pump as a signal and a newly formed cascade signal. This equivalently occurs on the side of the original idler creating cascade idlers. The cascades themselves can act as pumps and so on. This can continue indefinitely subject however to phase matching and material transmittance.

Finally, it is worth mentioning that waves situated upon a frequency spectrum throughout propagation are usually subject to dynamic multiple FWM processes. As a result, all the power variations throughout all the frequency spectrum need to be calculated simultaneously. While modelling unitary FWM processes can be insightful in describing the behaviour of propagating waves it does not provide an accurate depiction of dynamic FWM. The MM-GNLSE however does give a synchronous depiction of all effects of interest at every propagating step.

2.1.7 Raman Effect

As discussed previously the Raman effect is described as a time-delayed nonlinear process in conjunction to the Kerr effect. A quantum mechanical explanation of the effect is that a pump photon excites the medium's molecules to a virtual state which in turn decays to a vibrational state resulting in a photon of a lower frequency (or lower energy) being produced [9]. Within a frequency spectrum, this will lead to new waves being created at lower frequencies than initially pumped. This is known as Spontaneous Raman Scattering (SRS). One could also propagate a signal at those lower frequencies inherently amplifying said signal emanating a process called stimulated Raman scattering.

Due to the material nature of the Raman effect, it stands to reason that the gain and position of these shifted wavelengths will be material dependent. In particular for silica, which is the primary material considered throughout this research, the Raman response function $h(t)$ has been experimentally measured in [30]. The Fourier transform of which reveals details of how the Raman effect affects the propagating spectrum. The real and imaginary components of $\tilde{h}(f)$ are shown in Figure 2.3 (normalised such that $\int_{-\infty}^{\infty} h(t) = 1$). The real part affects the refractive index of the material and the imaginary part is responsible for the Raman gain [9]. Raman gain has a maximum at approximately $\Delta f = -13.2\,\text{THz}$ and tends to zero after $|\Delta f| = 60\,\text{THz}$. The real part is symmetric around the y-axis ergo the perturbation of the refractive index is mirrored around the central frequency. On the other hand, the imaginary part is antisymmetric in frequency. Therefore if a Continuous Wave (CW) is pumped into a silica fibre, neglecting the influence of FWM, this will result in a spectrum of waves being created down-shifted upon the spectrum and also additional energy (if present) from the larger frequencies will be converted to the CW pulse.

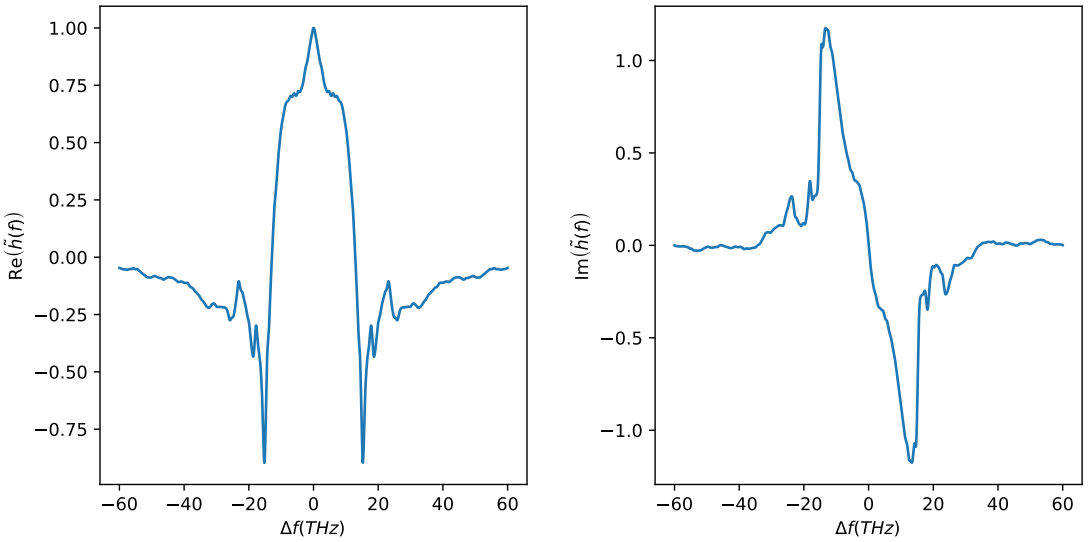

FIGURE 2.3: Real (left) and imaginary (right) parts of the Fourier transform of the Raman response function for silica.

.

During propagation throughout a non-linear medium, the Raman and Kerr effects influence the pulse and need to both be incorporated into a numerical model like in (2.41). Even though the effects are physically distinct they are incorporated together within the equation. The higher the fractional contribution of the Raman effect, the lower that of the Kerr effect. For silica the fractional contribution is set to be $f_R = 0.18$ [9]. While the MM-GNLSE does incorporate both effects coupled (in terms of selected frequency bands) pulse propagation equations often neglect the Raman effect when investigating Kerr effects [9, 10, 24]. This is discussed further in Chapter 4 along with a derivation and proof of Raman effect included coupled pulse propagation equations.

2.1.8 Noise Floor

In optical fibres as in every system there is a limited amount of noise permitted by quantum mechanics [31]. The presence of this noise is significant for simulating various fundamental phenomena investigated in this thesis, for example SRS and modulation instability. This quantum noise floor is calculated for every discrete frequency vector as:

$$\nu\left(f\right) = \Theta(f)\sqrt{\frac{h}{4\pi}\mathrm{df}\sum_{i=1}^{\mathrm{N}}\omega_i}, \tag{2.49}$$

where h is Planks constant [28], N is the number of grid points sampled, df the frequency step and $\Theta(f)$ a complex Gaussian random number function added to generate a random phase. Within this thesis the noise floor is added to the amplitude for every frequency band or mode.

2.2 Numerical Modelling

2.2.1 Scientific Computing Tools

An imperative part of scientific research is the numerical modelling of the physical phenomena of interest. This need has resulted in the creation of a plethora of tools and philosophies that enhance and guide the way numerical tools are created and operated in science. There are a variety of scientific software that are used for modelling. While there are some like Comsol Multiphysics [32] that can be used with minimal knowledge of the underlying mathematical model and source code, usually a more dedicated approach is needed. Throughout this research, a number of software tools have been used to meet the needs of the project with selected ones discussed here.

The core programming language used during this research is Python while making use of the Python scientific stack [33]. Python is a dynamically typed, interpreted language whose source code is relatively easy to read, write and by extension maintain. While the core execution times are larger than compiled languages there are a number of libraries dedicated to scientific computing that enhance the speed of programs. Fundamental among these is Numerical Python (NumPy) which adds multidimensional arrays and a large number of functions that are compiled in either C or FORTRAN providing the enhanced speed [34]. An extensive set of scientific functions and methods is also provided by Scientific Python (SciPy) [35]. On the other hand Symbolic Python (SymPy) is used for symbolic algebra calculations [36]. For data exportation the H5Py library [37] is used which is a wrapper around the HDF5 library [38]. This allows complex data structures to be efficiently exported and imported when needed. Finally, for graphical visualisation purposes, the Matplotlib library is used [39].

All previous libraries stated are highly optimised, but in some cases, further enhancement is possible and required. A first step approach of doing so is by utilizing the Intel distribution for Python. By making use of Intel math kernel library (MKL) the distribution allows significant acceleration of NumPy and SciPy functions [35]. However, situations arise where additional speed-up is required. Within this research two approaches have been implemented. The foremost is to make use of the Numba compiler which compiles selected parts of the source code just before execution [40]. The second is to compile the entirety or selected parts of the Python code using Cython which translates the source code into optimised C code [41].

Parallelisation of source code can provide a decrease in execution times of numerical methods [42]. However, in this research project, the variation of the output parameters with respect to different variables is usually of interest. Therefore the parallel implementation applied to it is done with respect to different inputs. When implementing parallel computations on single Desktop multi-core Central Processor Units (CPU) the

Python library joblib was used which is a wrapper around the Python Multiprocessing library [43].

For some numerical models, like the ones described in Chapters 3, 5, 6, computation can be further accelerated by using High Performance Computing (HPC) facilities. The acceleration is established by the introduction of multiple computing nodes as well as multi-core CPU. To implement hybrid multi-core and multi-node computations on HPC facilities the mpi4py [44] module was used which is a wrapper around the Message Passing Interface (MPI) library [42].

Computation throughout this project was conducted on both a desktop and HPC facilities. The desktop comprises of a 4-core Intel i7-4790 CPU at 3.60 GHz frequency with an 8 MB cache. The Random Access Memory (RAM) is at 32 GB size with a frequency of 1600 MHz. The supercomputers used are the IRIDIS 4 and IRIDIS 5 provided by the University of Southampton. IRIDIS 4 comprises of 750 computing nodes with each node comprising of an Intel 8-core Xeon E5-2670 processor at 2.6 GHz and was used in producing the results shown in Chapter 3. IRIDIS 5 is the most modern of the two HPCs with 464 computing nodes, each node having two 20 core Intel Xeon E5-2670 processors and was pivotal in producing the results in Chapters 5, 6.

2.2.2 Scientific Software Engineering

Software engineering in scientific research can be organic in its implementation because the output of the research may not be necessarily clear from the onset. Therefore cases arise where enhancements of numerical models need to be appended to the software throughout development. Also, versions of it need to be kept on record in cases where reverting to a previous iteration is required. The software used to keep records of the source code within this research project is Git [45]. In addition to this, the software revisions are hosted on Github [46] to establish a focal point when developing over multiple machines. Finally, when development is complete the software can be assigned a DOI (Digital object identifier) by using the Zenodo platform [47] to make the software freely available and citable. Lists of the software published this way throughout this research project can be found in Appendix A.3.

The numerical models created in this research, like many in scientific software engineering, can become very large and be comprised of many subroutines. This creates a difficulty in constantly establishing the validity of the model throughout development. A way to combat this is, along with the source code, to write separate tests on each subroutine, a methodology known as unit-testing. These tests can be simple, for example establishing that energy is conserved in a subsystem. By establishing these tests one can reduce the possibility of further iterations of the software producing non-physical results.

Finally, since the numerical methods produced in this research rely upon various external libraries it is important to make sure that operation is maintained for future updates of those libraries. This is done by making use of the continuous integration software, Travis [48]. This program remotely installs the required libraries used in the numerical model and executes the unit-tests to confirm that the software is functioning. Each of the published software of this research has this function attached to it.

2.2.3 Numerical Evaluation of the Generalised Nonlinear Schrödinger Equation

Numerically evaluating the MM-GNLSE is the most computationally challenging part of this research. It is therefore imperative that the numerical method chosen to solve it is as efficient and accurate as possible.

The GNLSE (2.35) is a partial differential equation with respect to time and space with the time derivatives being of arbitrary order because of the Taylor expansion of the dispersion. The n_{th} order of the time derivatives make partial differential equation solvers like the Crank-Nicolson method incapable of solving the equation unless high order derivatives are neglected. A more dedicated approach is therefore required. The numerical method used to solve the GNLSE throughout this report is the symmetrized SSFM whose premise is detailed below.

The MM-GNLSE can be applied in the form of [9]:

$$\frac{\partial A_\mu(z,t)}{\partial z} = \left(\hat{\mathcal{D}}_\mu + \hat{\mathcal{N}}_\mu\right) A_\mu(z,t), \tag{2.50}$$

where $\hat{\mathcal{D}}_p = \mathcal{D}_p/A_p(z,t)$ and $\hat{\mathcal{N}}_p = \mathcal{N}_p/A_p(z,t)$. Therefore the amplitude at a step size h for mode μ can be found by:

$$A_\mu(z+h,t) = \exp\left(h\left(\hat{\mathcal{D}}_\mu + \hat{\mathcal{N}}_\mu\right)\right) A_\mu(z,t). \tag{2.51}$$

Since the operators within the exponential term are non-commuting the need arises to approximate the equation. The envelope can be approximated by [9]:

$$A_\mu(z+h,t) = \exp\left(\frac{h}{2}\hat{\mathcal{D}}\right) \exp\left(\int_z^{z+h} \hat{N}(\psi)\, d\psi\right) \exp\left(\frac{h}{2}\hat{\mathcal{D}}\right) A_\mu(z,t) + \mathcal{O}\left(h^3\right). \tag{2.52}$$

Inherently (2.52) describes a propagation where half a step is taken using the dispersion operator, a full step using the nonlinear operator and finally another half a step with the

dispersion. Using the FFT of the symmetrized SSFM premise a step of the MM-GNLSE is achieved by:

$$A_\mu(z+h,t) = F^{-1}\left(\exp\left(\tilde{\mathcal{D}}\frac{h}{2}\right)F\left(\int_z^{z+h}\hat{N}F^{-1}\left(\exp\left(\tilde{\mathcal{D}}\frac{h}{2}\right)F\left(A_\mu\right)\right)d\psi\right)\right), \quad (2.53)$$

where $\tilde{\mathcal{D}} = F\left(\hat{\mathcal{D}}\right)$, F represents a Fourier transform and F^{-1} the inverse Fourier transform.

It is worth mentioning that an alternative to solving (2.50) using the symmetrized SSFM one could write it using the non-symmetrized SSFM [9]. For this method half a step is taken using the nonlinear and half using the dispersion operator. As can be expected this method would exhibit faster execution times since less arithmetics would be required at every step. However, the error at each step for this method is second order with respect to h as opposed to the symmetrized SSFM which is third order. Therefore, to maintain a higher accuracy the symmetrized SSFM is used in this thesis.

The step size h is paramount to the success of the algorithm. Also, the nonlinear term holds a somewhat complex dependence upon the envelope function A which changes at every step. Henceforth one can employ a widely used RK adaptive step algorithm [49] with a predetermined error tolerance to the integral at the nonlinear step. Over one step of the symmetrized SSFM firstly the half dispersion step is taken. Following this, the integral is estimated at fourth and fifth order. If the difference between these orders is higher than the predetermined error tolerance then the step size is lowered and the process repeated until the tolerance is met. Afterwards, the rest of the half step with dispersion is taken. Finally, in preparation for the next step, if the difference between the orders is less than the tolerance the following step size is increased. This way in simulations where the nonlinear integrand is more complex the algorithm will take smaller steps and hence conserve the accuracy. On the other hand, if the opposite occurs the algorithm will have much shorter execution times.

As can be expected the selection of which RK method to use is paramount to the efficiency of the symmetrized SSFM. As a result, multiple adaptive stepping RK methods where considered. The testing was conducted upon the single-mode fibre used in Chapters 4, 5 for 100 m propagation. The input pulse has a pump at a wavelength of 1048 nm with $10W$ of power and a seed at 1200 nm with 100 mW. These parameters result in Degenerate FWM as shown in Figure 2.2(b). Equation (2.35) is solved using the symmetrized SSFM for the aforementioned parameters with different adaptive RK methods in the nonlinear step. The methods considered are the Runge-Kutta Fehlberg [50], Runge-Kutta Cash-Karp [51] and Runge-Kutta Dormand-Prince [52]. Execution time was measured on the desktop described in Section 2.2.1. Figure 2.4 shows the average execution time (over 1000 iterations) against the predetermined error tolerance.

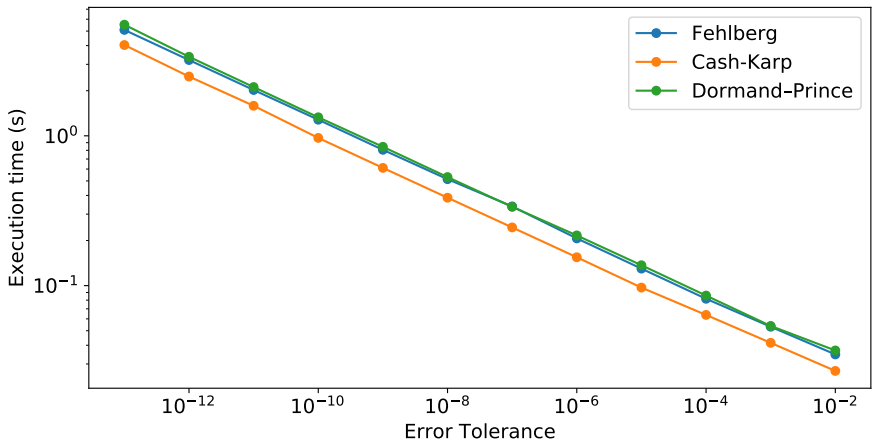

FIGURE 2.4: Comparison of execution times of the symmetrized SSFM using multiple RK schemes.

The Dormand-Prince and the Fehlberg method have very similar execution times even though the first has an extra function evaluation. However, the Cash-Karp method consistently exhibits lower execution times than the other two showing a speedup of $20 - 30\%$. This can be expected since the Cash-Karp integrator was created for integrands that are fast varying which is an attribute exhibited by the nonlinear step of the symmetrized SSFM [51]. As a result of this test, the Cash-Karp method was used to evaluate the nonlinear step in the symmetrized SSFM throughout all research conducted in this research project.

While the RK method decides the step of the symmetrized SSFM its efficiency is greatly dependent upon the execution time of the FFT and its inverse. It is therefore important that the underlying libraries of the Python program are effective. As stated earlier the Intel distribution for Python is used throughout this research for the increased speed that the MKL libraries provide. To prove the point the average execution speed of the FFT is measured while using these libraries and compared to the equivalent timings for when they are not used. As with the RK test case execution time was measured on the desktop described in Section 2.2.1. Figure 2.5 depicts the average speed-up (over 1000 iterations) for the FFT and its inverse when using MKL libraries with respect to the number of points considered. The speed-up initially starts at 150% and increases greatly to approximately 350% for larger size arrays. The increase in speed is because of the optimisation that the MKL libraries provide when using Intel CPU. It is important to mention that these tests were conducted with a single MKL thread and therefore the speed-up is not attributed to multi-core computations.

The symmetrized SSFM, along with the above numerical and computational enhancements, is an efficient method for simulating the GNLSE. However, as the number of grid points is increased (which is required when a large frequency bandwidth is considered) the algorithm slows down dramatically because of the slowdown of the FFT algorithm

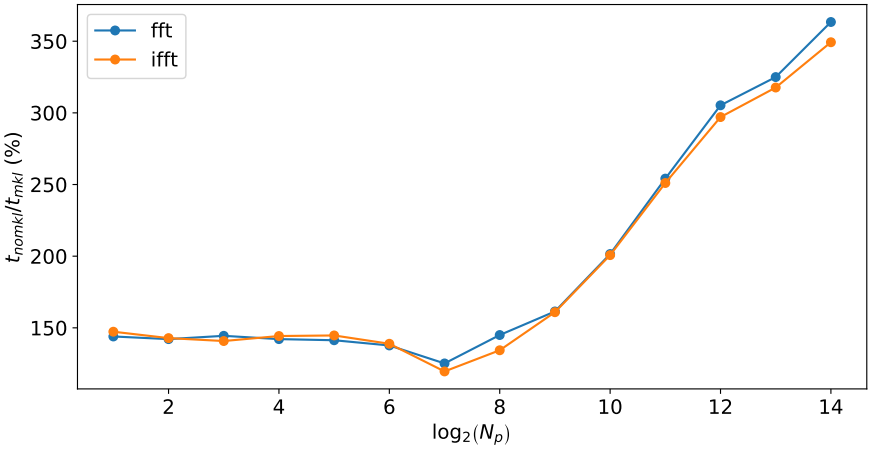

FIGURE 2.5: Percentage speedup of the FFT and IFFT algorithms with the inclusion of MKL libraries.

and the matrix arithmetics. This issue was primarily found in the research of Chapter 5 and led to the derivation and implementation of the BNLSE presented in Chapter 4.

2.3 Fibre Optic Parametric Converters

Within this thesis, single and multi mode FOPAs and FOPOs are investigated for energy conversion between wavelengths and modes. As discussed above, wavelength conversion can be achieved within an optical fibre by utilising nonlinear effects within the optical fibre. The two nonlinear effects used for wavelength and mode conversion within optical fibres are the Kerr and Raman effect.

Fibre Optic Parametric Converters that utilise the Raman effect for wavelength conversion are called Raman amplifiers. These systems provide efficient and tunable wavelength conversion of light from shorter to longer wavelengths. Such a system was demonstrated by Chen et al. [53]. In their study they exhibit a CE of 78.8 % over a wavelength range of 42 nm. Raman amplifiers are also widely used within the telecommunications industry for long-haul amplification of WDM systems [9].

While Raman amplifiers are used for tunable wavelength conversion and amplification, energy conversion can only occur to longer wavelengths (with respect to the pump) and within the Raman gain bandwidth. This is not the case for FOPAs where energy can be transferred to longer and shorter wavelengths (with respect to the pump) over a theoretically infinite bandwidth.

FOPAs have been investigated as fibre systems capable of amplification and wavelength conversion since they were first reported in [54]. The materials of the fibres used as the gain medium for these amplifiers have ranged from Silica [9] to novel highly nonlinear materials [55] and recently, Silicon [56]. These FOPAs can be pumped by a single (as

shown in Figure 2.2(a)) [57] or two pumps (as shown in Figure 2.2(b)) [58]. In both of these cases, a signal is inserted into the fibre along with the pumps for efficient parametric conversion to occur, this is not a requirement for the operation of FOPOs as will be discussed later in the thesis.

The waves involved in the parametric process within a FOPA can be pulsed or CW [9]. However, since the fibre amplifiers and oscillators discussed within this thesis are pumped by CWs it is worth mentioning some noteworthy studies whose FOPA is pumped by waves of the same type. Also, is worth mentioning that only studies whose primary focus is wavelength conversion within a FOPA are mentioned here (*i.e* the focus is drawn upon the CE of the idler instead of the amplification of the signal). Within their study, Tourounidis et al. report a maximum CE of 1.5 % over ≈ 200 nm from the pump which is set at ≈ 1550 nm [59]. A higher CE was achieved recently by Ahmad et al. In detail, they report a CE of ≈ 40 % over a 20 nm bandwidth (from the pump of ≈ 1590 nm) [60]. Within the afformentioned studies, it is indicated that the efficiency is dependent upon the input power, fibre length and nonlinearity of the fibre.

Finally, it is worth mentioning that the the gain of FOPAs and FOPOs can be negatively impacted by Polarisation Mode Dispersion (PMD). This effect has been shown to introduce signal fluctuations that depend upon environmental variations [10]. PMD is neglected throughout this thesis when simulating FOPAs and FOPOs. To incorporate PMD into the simulations of single-mode parametric devices a two-mode version MM-GNLSE could be used. The two modes would represent the polarisations of the fundamental mode. By introducing a random variation of the dispersions of the modes the fluctuations of PMD could be modelled. However, a Polarisation Mainting Fibre (PMF) is used as the gain medium for the single-mode parametric devices simulated within this thesis. Therefore PMD is neglected hereafter and the SM-GNLSE is used to model these devices.

2.4 Conclusion

The key physical principles and numerical models used in this research have been outlined in this chapter. By using Maxwell's equations as a starting point, the equations that describe the behaviour of light within a silica optical fibre were derived and the approximations taken at each step outlined. The model of fibre modes was presented as solutions to Maxwell's equations and their behaviour during propagation along the longitudinal direction was discussed. The SMR equation was derived and used to describe WDMCs which is an integral part of the FOPO system simulated in Chapter 5. Further from this, the widely used in this research MM-GNLSE, was presented and each of the physical processes it simulates such as dispersion, SPM, XPM, FWM and Raman effects were discussed in detail. The equation is simulated in every chapter of this thesis

for either one or two modes. In Chapter 4 the equation is modified to apply to multiple frequency bands to accurately and efficiently simulate spectra over large bandwidths.

In the second section of this chapter, the philosophies and tools used in the development of the software of this research were discussed. An extended description of the symmetrized SSFM was presented and the efficiency of the numerical methods used was tested. The efficiency of numerically evaluating the MM-GNLSE may not be as vital when investigating FOPAs but is paramount when simulating FOPOs since the equation needs to be evaluated over thousands of round trips. Further optimisation of the source code of each model is outlined in their corresponding chapters.

In the final section of this chapter, a brief overview of the latest fibre optic parametric converters was given. Additionally, the adverse effect of PMD has on single-mode FOPAs and FOPOs was discussed along with how it is countered within the wavelength converters presented in this thesis.

Chapter 3

Inter-modal Four Wave Mixing in a Two-mode Fibre

One of the objectives of the fibre telecommunications industry is to expand the capacity of fibre systems to combat the ever increasing need for data transfer that is exhibited in today's society. Primarily to avoid modal dispersion and high attenuation mostly single mode fibres have been employed within the industry. Within these fibres, multiple channels of data can be transferred along separate wavelengths within the fibre forming WDM systems. However, the number of channels within each single mode fibre are not expected to suffice to combat the need for data leading to a predicted capacity crunch [2]. A potential alternative to this is introducing spatial channels with multiple modes which, in combination with WDM systems, could multiply the number of channels that a single fibre will support.

If multimode WDM systems are to be used for long propagation, then systems for transferring energy between the spatial modes and wavelengths need to be employed. It can also be beneficial if this energy transfer occurs during propagation. An attractive option to achieve this is the nonlinear effect of FWM between modes, dubbed Inter-modal Four Wave Mixing (IM-FWM).

The first time IM-FWM was presented was Stolen et al. in [54] who phase matched the conversion between multiple spatial modes using cm long silica fibres as a propagation medium. The particularly small length of the fibres used was primarily due to non-uniformity of the dispersion along the propagating direction. The spectral efficiency of a TMF was investigated by Chen et al. [61]. Within this research, it was demonstrated that despite IM-FWM, the number of channels the TMF supports approaches three times those of an equivalent Single Mode Fibre (SMF). Henceforth it can be estimated that IM-FWM can be used for mode/wavelength conversion without inadvertently affecting the spectral efficiency of a telecommunications system. Following from this [62] analytically described the phase matching condition for IM-FWM and applied their theory on

a 55 mode parabolic index fibre. Within the research however only up to the second order expansion coefficients of the dispersion were considered, which at large frequency bandwidth would not provide an adequate representation of the system. Xiao et al. [63] discuss the theory behind IM-FWM using two models. They used the propagation equations found in [64] to simulate IM-FWM when linear coupling is considered and when it is not. In particular, they emphasise that random mode coupling and fluctuations in the fibre can lead to substantial reductions in CE. Essiambre et al. [20, 65] experimentally demonstrated IM-FWM over a 5 km TMF. They, in turn, argue that IM-FWM is mainly dependent upon the difference between the group velocities of the two modes. Hence for IM-FWM to occur, opposed to Single Mode Four Wave Mixing (SM-FWM), it is not required for the fibre to operate close to the zero dispersion wavelength for high conversion efficiencies to occur. The fibre lengths used in [20, 65] point out that contrary to the work conducted in [54, 63] improved fabrication processes today have resulted in a better uniformity of dispersion throughout propagation. Therefore IM-FWM ought to be investigated for long propagation mode-wavelength conversion.

In this Chapter, the simulations of FWM that were conducted upon a Two-Mode Graded Index Fibre (TM-GIF) are presented. This study was conducted in collaboration with Dr Francesca Parmigiani and Dr Søren Friis who were experimentally investigating IM-FWM upon the same fibre. Firstly the physical and mathematical approximations taken upon the fibre parameters are presented. Following this, the inner workings of the computational model are discussed. Finally, results along with conclusions drawn upon this system are laid out. The results from this study have been presented in three conferences (listed 1-3 in Appendix A.2) and a journal article (listed 1 of Appendix A.1).

3.1 Theoretical Modelling

3.1.1 Fundamental Premise

The primary objective of the system is to convert energy from the fundamental LP_{01} mode at a certain wavelength, to the LP_{11} higher order mode at another wavelength. This is achieved by making use of IM-FWM within a 1 km TM-GIF.

The waves at the input of the fibre are shown in Figure 3.1(a). The first pump (P_1) and the signal (S) are situated in the LP_{01} mode while the second pump (P_2) is in the LP_{11} mode. At the output of the fibre, newly formed waves are observed. As is shown in Figure 3.1(b) these waves are the idler (I) in the LP_{01} mode, the Phase Conjugation (PC) idler and the Bragg Scattering (BS) idler in the LP_{11} mode. The later two are the waves directly investigated within this study with particular interest taken on the CE bandwidth of these processes.

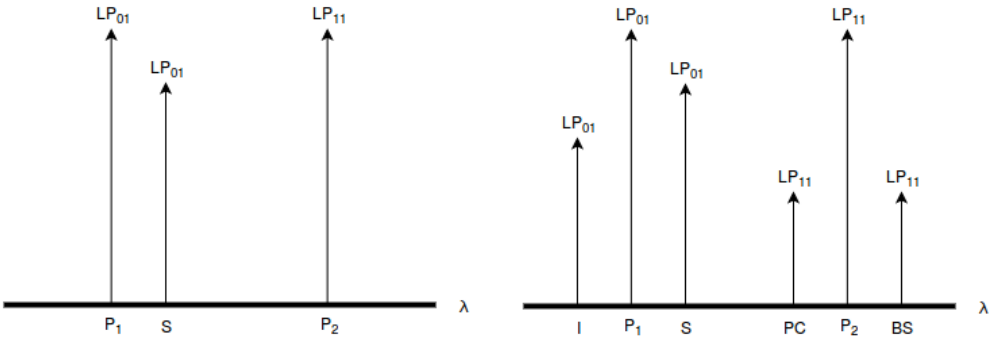

FIGURE 3.1: Graphical representation of input (a) and output (b) continuous waves of IM-FWM.

Even though, as stated in the previous chapter, multiple dynamic FWM processes occur throughout propagation it is of interest to identify and characterise the efficiency of the leading FWM process that creates each idler. By adopting the premise of the seeded FWM case as shown in Figure 2.2(a) one sees that the PC is principally the product of P_1, P_2 acting as the pumps and S as the signal. In contrast, the dominant FWM combination of the BS is S, P_2 acting as the pumps and P_1 as the signal. The angular frequency of the two idlers can be found by using (2.47) for both configurations. The CE in each case is subject to phase matching which is characterised by the phase mismatch parameter. By denoting the pumps P_1, P_2, signal S, and idler PC as the integers $1, 2, 3, 4$ respectively the phase mismatch parameter for the PC can be found by:

$$\begin{aligned}\Delta\beta \approx \Delta\beta_1\left(\omega_3-\omega_1\right)+\frac{\beta_2^{(01)}}{2}\left(\Delta\omega_3^2-\Delta\omega_1^2\right)+\frac{\beta_2^{(11)}}{2}\left(\Delta\omega_4^2-\Delta\omega_2^2\right)\\ +\frac{\beta_3^{(01)}}{6}\left(\Delta\omega_3^3-\Delta\omega_1^3\right)+\frac{\beta_3^{(11)}}{6}\left(\Delta\omega_4^3-\Delta\omega_2^3\right),\end{aligned} \tag{3.1}$$

where $\Delta\omega_i = \omega_i - \omega_0$ for $i = 1, 2, 3, 4$ and $\Delta\beta_1 = \beta_1^{(01)} - \beta_1^{(11)}$. The same premise can be used to calculate the phase-mismatch of the BS by setting $\omega_4 = \omega_{BS}$, $\omega_3 = \omega_{P_1}$ and $\omega_1 = \omega_S$.

As discussed previously in Section 2.1.6 the dynamic nature of FWM upon a spectrum cannot be entirely ignored. Therefore a suitable model to simulate multiple waves and modes propagating in a nonlinear medium is the MM-GNLSE. However, the refractive index profile of the particular fibre simulated, while identified as approximately a parabolic profile, was not known. This led to the inability of explicitly calculating the mode profiles and eigenvalues of the fibre. Nevertheless by making use of data provided about the fibre by the collaborative experimental group and by taking some approximations a model was formed to qualitatively describe the CE of the two idlers. In the next

two subsections the approximations taken to calculate the nonlinear and dispersion part of the MM-GNLSE are discussed.

3.1.2 Nonlinear operator

Supported by the conjecture that the refractive index profile can be considered parabolic the tranverse mode functions are assumed as Hermite-Gaussian modes which are given by [28]:

$$F_{(01)}(x,y) = \exp(-\frac{x^2+y^2}{w_{(01)}^2}) \tag{3.2}$$

$$F_{(11x)}(x,y) = 2\sqrt{2}\frac{x}{w_{(11)}}\exp(-\frac{x^2+y^2}{w_{(11)}^2}) \tag{3.3}$$

$$F_{(11y)}(x,y) = 2\sqrt{2}\frac{y}{w_{(11)}}\exp(-\frac{x^2+y^2}{w_{(11)}^2}) \tag{3.4}$$

where w_i is the width of the respective modes. The effective area of both modes was provided by the fibre manufacturer and are quoted to be:

$$A_{\text{eff}}^{(01)} = 161\,\mu\text{m}^2, \quad A_{\text{eff}}^{(11)} = 170\,\mu\text{m}^2.$$

By applying (3.2) and (3.3) to (2.21) and setting them equal to the inverse of the equivalent effective areas the widths of each mode are calculated to be:

$$w_{(01)} = 7.159\,\mu\text{m}, \quad w_{(11)} = 6.370\,\mu\text{m}.$$

Making use of the approximation of the Hermite-Gaussian modes can result in further simplifications in the MM-GNLSE. The modes are considered real valued and constant along the frequency spectrum. In addtion, only a single polarisation dirrection is considered. Finally, while LP_{11} is a spatially degenerate mode only one of these modes are investigated *i.e.* $F_{(11)}(x,y) = F_{(11x)}(x,y)$.

Using the aforementioned approximations one sees from (2.39) - (2.40) that $Q_{plmn}^{(1)} = Q_{\text{plmn}}^{(2)}$. Additionally the normalisation coefficient of mode k can be found by [25]:

$$N_{(k)}^2(\omega) \approx \frac{n_{\text{eff}}^{(k)}\epsilon_0 c}{2} \iint_{-\infty}^{\infty} F_{(k)}^2 dxdy, \tag{3.5}$$

where $n_{\text{eff}}^{(k)} = c\beta^{(k)}/\omega$ is the effective index of k mode. Because of the mathematical form of the modes the Q_{plmn} factors are non zero when all the indices are equal or when they form an even number of ones and zeros. Thus the non-zero overlaps take the form of:

$$Q_{0000}^{(1,2)} \approx \frac{1}{3A_{\text{eff}}^{(01)}}, Q_{1111}^{(1,2)} \approx \frac{1}{3A_{\text{eff}}^{(11)}}, Q_{\text{even}}^{(1,2)} \approx \frac{1}{3}\frac{\int F_{(01)}^2 F_{(11)}^2 dxdy}{\int F_{(01)}^2 dxdy \int F_{(11)}^2 dxdy}, \tag{3.6}$$

where the effective index of the mode is approximated to be the same as the material refractive index. A final result of the form of these modes is that the second term in (2.38) vanishes because the overlaps are assuned to be independent of frequency.

By applying (2.41) to (2.37) and introducing the above approximations the nonlinear coefficient of the MM-GNLSE is reduced to:

$$\begin{aligned}\mathcal{N}_\mu(z,t) = j\frac{n_2\omega_0}{c}\sum_{l,m,n}\left(1+\frac{j}{\omega_0}\frac{\partial}{\partial t}\right)Q_{\mu lmn}A_l(z,t)\Big(3\left(1-f_R\right)A_m(z,t)A_n^*(z,t) \\ +3f_R\int h(\tau)A_m(z,t-\tau)A_n^*(z,t-\tau)d\tau\Big).\end{aligned} \tag{3.7}$$

3.1.3 Dispersion Operator

The other fundamental parameters that could not be explicitly calculated because of the unknown refractive index profile were the propagation constants β of the modes. However, through experimental means, the dispersion parameters and dispersion slopes of the modes were measured by the collaborative experimental group. The dispersion and dispersion slope of the modes at a central wavelength $\lambda_c = 1.5508\,\mu$m are:

$$D^{(01)} = 19.8\,\text{ps/nm·km}, \quad D^{(11)} = 21.8\,\text{ps/nm·km}$$

$$S^{(01)} = 0.068\,\text{ps/nm}^2\text{km}, \quad S^{(11)} = 0.063\,\text{ps/nm}^2\text{km}$$

which, by making use of (2.44) and (2.45) results in the calculation of β_2, β_3 for both modes. Additionally the difference in β_1 between the LP_{01} and LP_{11} modes at that central wavelength was experimentally measured and shown to be $\Delta\beta_1 = 100\,\text{ps/km}$. Finally, the difference in β_0 was approximated using the Hermite-Gaussian mode approximation and can be calculated using [28]:

$$\Delta\beta_0 = \frac{2\pi n_0}{\lambda_c}\left(\left(1-\frac{\lambda_c^2}{\pi^2 n_0^2 w_{(01)}^2}\right)^{0.5} - \left(1-\frac{2\lambda_c^2}{\pi^2 n_0^2 w_{(11)}^2}\right)^{0.5}\right), \tag{3.8}$$

where n_0 is the refractive index approximated to be that of silica.

Finally, by making use of the above parameters and ignoring the dependence of higher order expansion coefficients of β the dispersion term of mode μ can be calculated from (2.36):

$$\mathcal{D}_\mu(z,t) = \left(j\Delta\beta_0 - \Delta\beta_1 \frac{\partial}{\partial t} - j\frac{\beta_2^{(\mu)}}{2}\frac{\partial^2}{\partial t^2} + \frac{\beta_3^{(\mu)}}{6}\frac{\partial^3}{\partial t^3} \right) A_\mu(z,t), \tag{3.9}$$

which along with (3.7) can be used to solve the MM-GNLSE numerically for this particular fibre.

3.2 Numerical Method and Implementation

Before the MM-GNLSE can be solved for the TM-GIF system described in Section 3.1 non-variable fibre parameters need to be established. As previously stated the fibre is assumed to be silica. Henceforth the nonlinear coefficients is set as $n_2 = 2.5 \cdot 10^{-20}\,\mathrm{m^2/W}$ [9], the fractional contribution of the Raman effect is set to $f_r = 0.18$ and the time delayed Raman response defined in [30] is used. Additionally, the overlap integrals are calculated by using (3.6) and inputed at the start of the executing code.

A fundamental step in simulating the MM-NLSE for the problem in Figure 3.1 is for the frequency grid to be created. The central frequency of the grid, named Median Frequency here to distinguish it from the Dispersion Central Frequency, is set to be that of the P_1 wave. A linearly spaced grid is then created between the median frequency and P_2. Auxiliary grid points are also added to the grid on frequencies larger than P_1 and less than P_2. This is done to limit the errors that would emerge from the periodic boundaries of Fourier Transforms.

After the grid is created, the initial amplitudes of P_1, P_2 are implemented upon the equivalent frequency domain grid as Kronecker delta functions. Due to the way the grid was established, S can only be situated upon discrete frequencies. By doing this the frequencies of the PC and BS, which are found by (2.47), will be part of the grid.

It is worth mentioning that the MM-GNLSE assumes that the fibre parameters (such as the refractive index profile and radius) are constant throughout propagation. This however is not the case in physical fibres and these parameter fluctuations can lead to intermodal coupling. This in turn can affect the efficiency of the MM-FOPA. While a model could be contrived that incorporates these variations they are neglected in this chapter for simplicity and instead the input parameters were chosen to be varied to fit the experimental results.

After all the above has been set n is solved as is described in Section 2.2.3. The resulting newly formed idlers are identified on the frequency grid and their powers are exported

for post-processing. The program is written in Python while making use of the Python scientific stack libraries previously discussed in Section 2.2.1. The numerical model also makes use of MKL libraries for their acceleration of array arithmetics and FFTs. Finally, the joblib module was used for mult-core evaluation of parameter sweeps on IRIDIS 4.

3.3 Application of the Model

3.3.1 Comparison to Experimental Results

Both the theoretical and numerical methods described above combined to create an adequate model to describe FWM within the TM-GIF. The accuracy of the model, however, is primarily dependent upon the inputted (stable) parameters provided through experimental means. Results from the simulations were initially compared to those of the experiments. However, as discussed in Section 3.1 while some of the fibre parameters are known, others were not and needed to be approximated. This led to the need to alter the input powers and dispersion of the model to fit the experimental results.

The experiments reported an input power of 30.5 dBm in both the first and second pump and the power of the signal was considered to be -24 dBm lower than that of the pump. The first pump (P_1) and the signal (S) were situated in the LP_{01} mode and the second pump (P_2) in the LP_{11} mode. These input powers were quoted by the experimental group. However, losses can occur within the optical setup before the launching of the two modes into the fibre and as stated earlier intermodal coupling is neglected by the computational model. Therefore the input powers of the computational model were changed to fit the experimental results. Using the MM-GNLSE equation, it was estimated that the simulation input powers of P_1 and P_2 should be altered to 27.5 dBm and 26.5 dBm respectively. By extension the input signal power is fixed to 3.5 dBm. Additionally $\Delta\beta_1$ needed to be altered to 95 $^{\text{ps}}/_{\text{km}}$ to better fit the experimental data. The reason that this parameter was altered is that during the length of the fibre the dispersion varies. This is something that is however not captured in the numerical model and therefore needs to be compensated for.

By making use of the previous parameters and using the aforementioned alterations to the pump powers and $\Delta\beta_1$, the system shown in Figure 3.1 was simulated and the results compared to the equivalent experimental results. The wavelength of P_1 is kept constant at $\lambda_{P_1} = 1549$ nm while the signal S is varied for several LP_{11} pump P_2 wavelengths. This in turn varies the position and power of the newly formed PC and BS idlers whose conversion efficiency is defined in this study as the ratio of the outputted signal and idlers.

Figure 3.2 illustrates the CE of the PC and the BS processes for a $\lambda_{P_2} = 1553.5$ nm at a varying signal wavelength. As can be seen the BS obtained from the model provides

a qualitatively accurate description of the CE. In particular the model predicts the peak found at $\lambda_s = 1549.5\,\text{nm}$ which is a result of a dynamic FWM process discussed further within Subsection 3.3.2. The PC on the other hand is accurately replicated for low wavelength bandwidths with deviations arising at longer wavelengths. A better fit between the two approaches is observed for $\lambda_{P_2} = 1554.5\,\text{nm}$ shown in Figure 3.3. The CE of the PC exhibits two high peaks along the wavelength sweep which is observed both in the experiments and the numerical method. This phenomenon is exhibited by the PC in the wavelength regimes investigated and is discussed in Subsection 3.3.2.

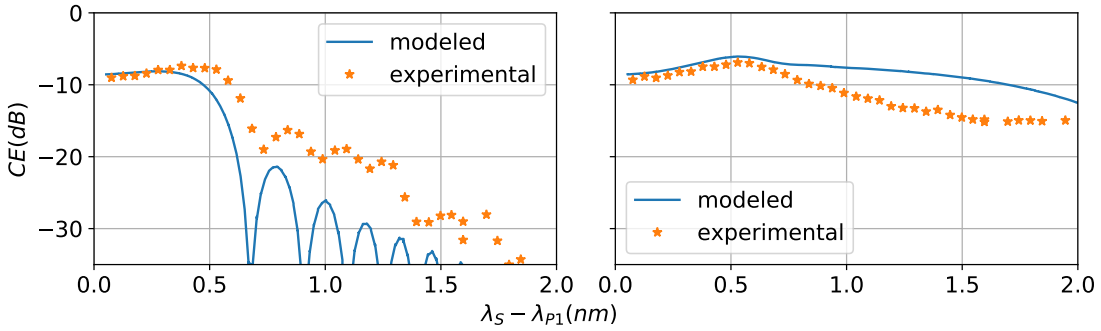

FIGURE 3.2: Comparison between the experimental and modelled conversion efficiency of the phase conjugation idler (left) and the Bragg scattering idler (right) for $\lambda_{P_2} = 1553.5\,\text{nm}$.

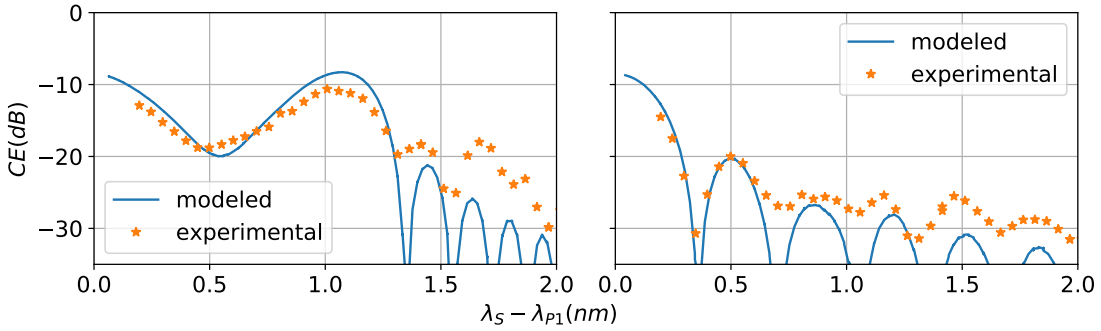

FIGURE 3.3: Comparison between the experimental and modelled conversion efficiency of the phase conjugation idler (left) and the Bragg scattering idler (right) for $\lambda_{P_2} = 1554.5\,\text{nm}$.

As can be seen in both figures the model is qualitatively successful in describing the general behaviour of the conversion efficiency for both idlers. However, some discrepancies in comparison to the experimental results are experienced. While some of these discrepancies could be attributed to experimental errors, the creation of the theoretical model has needed a certain number of approximations. One in particular that has not been adequately addressed is both the accuracy of the second and third order terms of the Taylor expansion of both modes and the influence of higher order terms. By considering (3.1) one can identify that the larger the separation between the pump and signal wavelength the more important higher order terms become. Hence a small change in the second and third order terms will result in vastly different CE results. In addition,

at very large separations, the influence of even higher order terms not considered in this model will vastly perturb the results.

Nevertheless, the computational model does experience success in describing the general trend of the CE for both the PC and BS. In the next subsection it is used to predict the overall behaviour of these idlers over broad wavelength separations answering questions about the behaviour and bandwidth of these idlers.

3.3.2 Numerical Results

The model described throughout this chapter was simulated for varying signal and pump wavelengths. Particular interest to this research was the behaviour of the CE of the PC and BS for varying signal and P_2 pump wavelengths. For the purposes of the simulation the λ_{P_1} is kept constant at 1549 nm while λ_{P_2} and λ_S are considered variable parameters. Finally, the input powers and dispersion parameters are the same as outlined in the previous subsection.

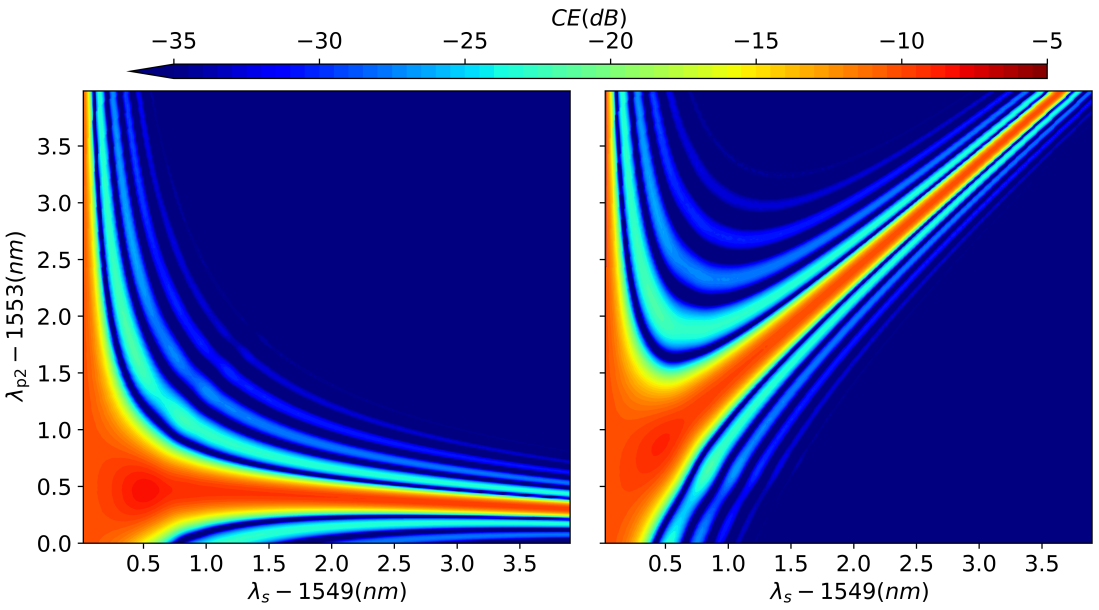

FIGURE 3.4: Conversion efficiency of (left) BS and (right) PC using the MM-GNLSE model [21].

The dependence of the CE of the PC and BS upon the wavelengths of the P_2 pump and the signal is graphically presented in Figure 3.4. Both of the idlers experience high CE at signal wavelengths close to that of P_1. This can be expected because as ω_1 tends to ω_3 then according to (3.1) the phase mismatch of both idlers tends to zero. However, for longer signal wavelengths, the behaviour of the two idlers deviates. The BS experiences high CE for all the signal wavelengths investigated at a relatively constant λ_{P_2}. On the other hand, the high CE trend in the PC has a dependence upon λ_{P_2}. This different behaviour can be explained by using (3.1). For signal wavelengths away from that of

P_1 the first term needs to be cancelled out by those of higher order. In the case of the PC as the signal wavelength increases ω_3 becomes smaller which in turn results in ω_4 becoming larger to satisfy (2.47). Thus for high CE to be maintained there is a need for ω_2 to be altered to counteract the difference in the group velocity of the two modes. It is worth mentioning that this effect is the reason for the two peaks depicted in Figure 3.3. On the other hand, in the case of the BS, ω_1 is decreased which in turn, because of (2.47), results in ω_4 being decreased. This results in the CE being kept higher over a longer bandwidth for a constant λ_{P_2}.

The CE of both the PC and BS exhibit a distinct peak at $\lambda_S < 1550\,\text{nm}$ and $\lambda_{P2} < 1554\,\text{nm}$. This is not an effect of the phase mismatch term and is in fact a result of the influence of the newly formed LP_{01} idler that is created during propagation (depicted in Figure 3.1(b) as I). At those wavelengths it exhibits relatively high power and in turn forms FWM partners that amplify the LP_{11} idlers. This effect is therefore a dynamic FWM process and while it is successfully simulated by the MM-GNLSE it would not be present if each FWM process was simulated independently.

Away from where the CE is highest both the PC and the BS exhibit a series of peaks. At these wavelength separations, the absolute of the phase mismatch is not close to zero; therefore power is exchanged between waves over the length of the fibre instead of only being transferred from the pumps to the signal and idlers. Thus, instead of exhibiting a steady decline in CE when moving away from the phase-matched area (which (3.1) would suggest) there are sudden decreases succeeded by peaks. At the points where the large decreases are observed it can be assumed that most of the energy in the LP_{11} idlers has been back-converted to the pumps and signal. The reason that this behaviour varies with respect to the wavelengths involved is that at non-phase matched regimes, the CE is also dependent on the phases of the waves involved [10] and, the modulation of these phases along propagation is frequency/wavelength dependent.

Since the previously mentioned series of peaks are subject to phase and fibre length it stands to reason that practical applications of the FOPA should only be considered at phase-matched regimes. The most attractive of the two idlers can be considered the BS since the CE remains high for a relatively constant P_2 wavelength. This however does not continue indefinitely because of the difference in β_2 of the two modes and the influence of β_3. Additionally, as the wavelengths considered deviate more from the dispersion central wavelength higher order dispersion terms would need to be considered which would perturb the bandwidth of the BS. While the CE of the PC does not exhibit the same behaviour as the BS for a constant P_2 wavelength it does experience two separate peaks which can be beneficial for conversion to selected wavelengths. Finally, wavelength conversion to both the PC and BS could be efficiently operated over very large bandwidths by varying the frequency of P_2.

3.4 Conclusion

The theoretical and numerical model used to simulate FWM within a 1 km TM-GIF has been presented. Particular interest was taken in the conversion of energy from a signal in the LP_{01} mode to the PC and BS idlers in the LP_{11} mode. Initial simulations were compared to equivalent experimental results which were provided by Dr Francesca Parmigiani and Dr Søren Friis. After this, the system was simulated for variable S and P_2 wavelengths where the behaviour of the CE for both idlers was calculated. The behaviour of the CE was explained by firstly making use of the phase-mismatch parameter shown in (3.1) and secondly by identifying the dynamic FWM processes that influence the results. The results depicted in this chapter show that CEs of above -10 dB can be achieved for a bandwidth of approximately 4 nm (with a stable P_2 pump). CEs at this bandwidth could be achievable for both idlers if the wavelength of the P_2 is varied. These bandwidths are relatively small however if the MM-FOPA is expected to operate in the entirety of the telecommunications C band (≈ 35 nm). The dispersion profile of the fibres utilised can be tailored however such that to extend the operational bandwidth of future MM-FOPAs.

Within the simulations, only a single LP_{11} polarisation is simulated. The reason behind this is that the input pump P_2 is comprised only by a single spatial mode (for example the LP_{11x} mode). Therefore IM-FWM is expected to only occur between the LP_{01} and the LP_{11x} modes. This was also the setup of the collaborative experimental group. However, parameter fluctuations along the length of the fibre can result in energy being transferred to the LP_{11y} mode. This, in turn, can result in IM-FWM being conducted between the LP_{01} and both LP_{11} modes. Such a process could be simulated by using the MM-GNLSE. Further studies of IM-FWM within a TMF could incorporate these fluctuations and spatial modes into the numerical model.

Following the publication of this work in [21] a number of studies have emerged describing multi-mode FOPAs. Signorini et al. [66] simulated and experimentally demonstrated IM-FWM in silicon waveguides. Parmigiani et al.[67] experimentally illustrated broadband wavelength conversion for a three mode fibre. In [68] the authors numerically investigate IM-FWM between two and four spatial modes while limiting their investigation to degenerate FWM ($\lambda_{P_1} = \lambda_{P_2}$). In their research they find that the dispersion parameters (and by extension the CE) is sensitive to refractive index profile variations along the propagation direction particularly for higher order modes. This variation was also studied by Guasoni et al in [22] who also verify that this non-uniformity dramatically decreases the CE of IM-FWM. Furthermore their theory describes linear coupling between fibre modes which is an additional detrimental effect to the application of long propagation multi-mode FOPA systems to telecommunication networks.

These recent studies indicate that despite advances in fibre fabrication techniques random refractive index variations along the propagation direction are still detrimental to

the operation and reliability of multi-mode FOPAs. While these variations are still high for parametric amplification in km fibres the effects can be less prevalent in short length fibres [22]. However, shorter length fibres will also reduce the size of the gain medium which could either be compensated by using large pump powers or a Highly Nonlinear Fibre (HNLF). High powers though cannot be considered cost-effective for applications in telecommunications. HNLFs on the other hand would either require use of materials with a higher nonlinear coefficient, where fabrication techniques are not as refined as in silica [55], or by tailoring the refractive index profile to increase the mode overlaps. An alternative to this is to use a shorter length version of the fibre investigated in this chapter but recirculate a part of the spectrum back into the fibre, inherently forming a FOPO. Such a system is investigated in Chapter 6.

Chapter 4

Frequency-Banded Generalised Nonlinear Schrödinger Equation

In Chapter 2 it was briefly mentioned that solving the GNLSE with the SSFM can become computationally challenging when a large frequency bandwidth is investigated. This is because of the increased number of points required to maintain a high spectral density and the requirement of the FFT algorithm that the frequencies are linearly spaced [49]. An example of such a study is the model presented in Chapter 5 where a FOPO is investigated with large sideband separation and large spectral resolution which would be unfeasible to simulate using the GNLSE. This adversity is prevalent in FOPAs and FOPOs systems where the frequencies of interest are condensed into small frequency bands that can be widely separated over the bandwidth [69]. Therefore it is preferable to establish a numerical method that is able to model the interaction of these frequency bands without incorporating the frequencies between them.

To model such FOPA and FOPO systems the GNLSE is usually split into a number of CNLSE which efficiently model the interaction between the frequency bands [70]. However, these models usually do not take in to account the Raman contribution to the total nonlinearity, inherently attributing the entirety of the nonlinear coefficient to the Kerr effect. This proportional misplacement of the nonlinear effects results in a compounding deviation of the results calculated by using these CNLSEs when compared to those calculated by the GNLSE [10].

A number of studies have taken into account the proportional contribution of the Raman nonlinearity when investigating coupled amplitude equations (where only single frequencies are modelled for each parametric wave). In ref [27] it was proven that the Raman nonlinearity perturbs the effect of the cross-phase modulation between waves propagating within a nonlinear medium. In subsequent years a plethora of coupled amplitude equations have been used to model nonlinear effects during propagation through a fibre. These studies either wished to simulate FWM with sidebands within the Raman gain

bandwidth, and therefore were required to incorporate the contribution of the Raman nonlinearity [71, 72], or investigate Raman nonlinearity with FWM added as a secondary effect [23, 73, 74].

While the coupled amplitude equations of the above studies can be useful in investigating FWM for CWs the GNLSE is required to simulate pulses propagating through an optical fibre. Few studies have used CNLSEs with the inclusion of Raman proportionality factors. In particular, Golovchenko *et al.* [75] took into account the fractional contribution of the Raman nonlinearity when investigating the interaction between three frequency bands in silica fibres. However, the theory is constricted to frequency bands that are separated equally in frequency and the pump is considered to be undepleted. Similar approximations were taken by Lin *et al.* [76, 77] when deriving CNLSEs with applications for silicon waveguides. The non-depleted pump approximation, while useful to FWM applications where power transfer between the parametric waves is minimal, would be detrimental to applications where high conversion is quested for like in the case of the oscillator in Chapter 5. Finally, the constraint that the frequency bands considered need to be equally separated in frequency can limit the applicability of the equations.

In the initial part of this chapter, the SM-GNLSE is used as a starting point to derive a CNLSE (named the BNLSE) that is able to accurately and efficiently simulate nonlinear interactions between small frequency bands separated over a large bandwidth. Unlike previous CNLSEs that include the Raman factor the numerical method shown in this chapter is not constrained by the undepleted pump approximation and by the need for the frequency bands to be equally spaced from each other. Within the derivation of the numerical method, the approximations taken at each step are highlighted and the Raman nonlinearity dependent coefficients are provided. In the second part of the chapter, the BNLSE is validated against the SM-GNLSE and it is shown to be a more accurate method than the CNLSEs that do not include the Raman nonlinearity. It is worth mentioning that within the main body of this chapter referencing to CNLSEs is done with respect to the models that disregard Raman nonlinearity. Finally, the numerical execution times of all the models considered are also measured and compared.

This study has been the subject of an invited conference presentation (listed 6 in Appendix A.2), a journal article (listed 2 in Appendix A.1) and an accompanied published software (listed 2 in Appendix A.3).

4.1 Theoretical Model

4.1.1 Derivation of the Frequency-Banded Generalised Nonlinear Schrödinger Equation

The MM-GNLSE shown in (2.35) can be simplified to the SM-GNLSE when considering single mode propagation in an optical fibre [9]:

$$\begin{aligned}\frac{dA}{dz} = \Bigg[\mathrm{j} \sum_{n\geq 2} \frac{\beta_n}{n!} \left(\mathrm{j} \frac{\partial}{\partial t} \right)^n + \mathrm{j}\gamma \left(1 + \frac{\mathrm{j}}{\omega_0} \frac{\partial}{\partial t} \right) \Bigg((1 - f_r) \left| A(z,t) \right|^2 \\ + f_r \int h(\tau) \left| A(z, t-\tau) \right|^2 d\tau \Bigg) \Bigg] A(z,t) \,,\end{aligned} \tag{4.1}$$

where

$$\gamma = \frac{n_2 \omega}{c A_{\mathrm{eff}}} \tag{4.2}$$

is the nonlinear parameter.

The propagating amplitude A is assumed to be distributed over a continuous frequency grid. To derive the BNLSE the spectrum is split into discrete frequency bands of equal spectral width. Inherently there is no limit to the number of frequency bands the equation can be derived for, for example, a seven-band BNLSE is used in the model described in Chapter 5. However, for clarity, it is derived here for three bands. The amplitude in (4.1) is expressed as [24]:

$$A(z,t) = \sum_{l=-1}^{1} A_l(z,t) \exp(-\mathrm{j}\Omega_l t), \tag{4.3}$$

where the three bands are centred at angular frequencies $\Omega_{-1} < 0$, $\Omega_0 = 0$ and $\Omega_1 > 0$ relative to the central frequency of the central band ω_0.

Applying (4.3) to (4.1) results in terms with exponential dependences. Out of these the exponential terms involving $2\Omega_{\pm 1}$, $|\Omega_{+1}|$, $|\Omega_{-1}|$ *etc* are neglected since they are FWM terms that are not energy conserving in this three-band model. In addition, the Raman response functions are approximated as [24]:

$$\begin{aligned}\int h(\tau) A_m(t-\tau) A_n^*(t-\tau) \exp(-\mathrm{j}\Omega_l \tau) d\tau &\approx A_m(t) A_n^*(t) \int h(\tau) \exp(-\mathrm{j}\Omega_l \tau) d\tau \\ &= A_m(t) A_n^*(t) \tilde{h}(\Omega_l).\end{aligned} \tag{4.4}$$

This assumption indicates that intra-banded Raman effects are neglected or that each amplitude in the band is slowly varying when compared to $h(t)$. For example, for silica fibres this approximation holds if the pulse length is larger than 1 ps [9]. By taking into account these approximations the equations describing the amplitudes A_l can be found

by assembling the terms of $\exp(-\mathrm{j}\Omega)$ for $l = -1, 0, 1$ in (4.1). The three-band BNLSE can therefore be written as [24]:

$$\frac{dA_l}{dz} = \mathrm{j}\sum_{n\geq 2}\left(\frac{\beta_n}{n!}\left(\mathrm{j}\frac{\partial}{\partial t} - \Omega_l\right)^n\right)A_l + \mathrm{j}\gamma_l\left(1 + \frac{\mathrm{j}}{\omega_l}\frac{\partial}{\partial t}\right)\left(N_l A_l + M_l\right), \tag{4.5}$$

with

$$\begin{pmatrix} N_{-1} \\ N_0 \\ N_1 \end{pmatrix} = K \cdot \begin{pmatrix} |A_{-1}|^2 \\ |A_0|^2 \\ |A_1|^2 \end{pmatrix}, \tag{4.6}$$

$$K = \begin{pmatrix} 1 & 2 + f_r\left(\tilde{h}\left(\Omega_{-1}\right) - 1\right) & 2 + f_r\left(\tilde{h}\left(\Omega_{-1} - \Omega_{+1}\right) - 1\right) \\ 2 + f_r\left(\tilde{h}\left(-\Omega_{-1}\right) - 1\right) & 1 & 2 + f_r\left(\tilde{h}\left(-\Omega_{+1}\right) - 1\right) \\ 2 + f_r\left(\tilde{h}\left(\Omega_{+1} - \Omega_{-1}\right) - 1\right) & 2 + f_r\left(\tilde{h}\left(\Omega_{+1}\right) - 1\right) & 1 \end{pmatrix}, \tag{4.7}$$

$$\begin{pmatrix} M_{-1} \\ M_0 \\ M_1 \end{pmatrix} = \begin{pmatrix} \left(1 - f_r\left(1 - \tilde{h}\left(-\Omega_{+1}\right)\right)\right) \cdot A_0^2 A_1^* \exp(-\mathrm{j}(\Omega_{+1} + \Omega_{-1})t) \\ \left(1 - f_r\left(1 - \frac{\tilde{h}(\Omega_{-1}) + \tilde{h}(\Omega_{+1})}{2}\right)\right) \cdot 2A_1 A_{-1} A_0^* \exp(\mathrm{j}(\Omega_{+1} + \Omega_{-1})t) \\ \left(1 - f_r\left(1 - \tilde{h}\left(-\Omega_{-1}\right)\right)\right) \cdot A_0^2 A_{-1}^* \exp(-\mathrm{j}(\Omega_{+1} + \Omega_{-1})t) \end{pmatrix}, \tag{4.8}$$

where ω_l is the central angular frequency and

$$\gamma_l = \frac{n_2 \omega_l}{c A_{\text{eff}}}$$

the nonlinear coefficient of band l.

As can be seen the BNLSE encompasses two types of nonlinear interactions, intra-band and inter-band nonlinear effects. The first are dictated by the SPM terms (shown in the diagonal terms of the K matrix) and the second by the XPM and FWM terms, shown in the non-diagonal terms of the K matrix and all terms of the M matrix respectively. The inclusion of the Raman response functions to the XPM and FWM factors allows the frequency bands to be placed at arbitrary spectral separations from each other (*i.e.* both inside and outside the Raman gain bandwidth). If the frequency separation between all bands is larger than the Raman gain bandwidth, then the $\tilde{h}(\omega)$ terms within (4.7)- (4.8) can be approximated to zero and Raman nonlinearity plays no effect. Though in such a case the fractional contribution remains and is not neglected like in the CNLSE. If on the other hand a band is placed within the Raman gain bandwidth of another band then the associate Raman response functions affect the XPM and FWM factors.

As seen in (4.7) the SPM factors for each band are unity and not Raman dependent. This is because the intra-band Raman effect has been neglected in the derivation of the BNLSE. This approximation can limit the application scope of the model to pulse amplitudes that are slowly varying compared to $h(t)$. This means that within each band intra-band FWM processes have the entirety of the nonlinearity attributed to the

Kerr nonlinearity and therefore would suffer the same downfalls as the CNLSE does between bands if the pulses considered are smaller than that of the Raman response function. Additionally, in such cases, effects like Raman induced self-frequency shifting would not be replicated by this model. One could derive the BNLSE with the inclusion of intra-band Raman effects. However this would create computational challenges in applications of the model to high power system. For example, a high power CW pulse in one of the frequency bands propagating through a silica fibre would result in SRS. If the size of the frequency bands is smaller than 60 THz (which is required in many practical applications to maintain a high spectral density and low execution times) then the model would fail because of the periodic boundary conditions of the FFT algorithm. Thus, particularly for the practical applications of this thesis, it is preferable to limit the applicability of the equation by neglecting intra-band Raman effects.

The reduction of the investigated frequency spectrum to that of the frequency bands can have the adverse effect of not incorporating physical phenomena that are dependent upon the disregarded frequencies. For example spontaneous Raman scattering at frequencies outside the bands is not covered by this model. Furthermore, the time dependency that the components of the M matrix introduce to the model can result in the generation of parametric waves outside the predetermined frequency bands. However, this process requires phase matching, therefore in many situations the generation of these waves can be neglected. As can be seen it is important that an understanding of the modelled system is acquired prior to using the BNLSE in order to avoid neglecting essential physical phenomena. When the model has been used in this thesis the systems were initially investigated by using the GNLSE such that a preliminary understanding could be achieved.

The model is primarily suited to simulate FWM between frequency bands widely distributed along the bandwidth. For such applications energy needs to be conserved between the frequency bands; *ergo* the bands need to be equally spaced in frequency, or $\Omega_{+1} = -\Omega_{-1} = \Omega > 0$. Applying this conjecture to (4.5), (4.7) and (4.8) results in the simplified BNLSE suited to simulating FOPAs and FOPOs:

$$\frac{dA_l}{dz} = \mathrm{j}\sum_{n\geq 2}\left(\frac{\beta_n}{n!}\left(\mathrm{j}\frac{\partial}{\partial t} - l\Omega\right)^n\right)A_l + \mathrm{j}\gamma_l\left(1 + \frac{\mathrm{j}}{\omega_l}\frac{\partial}{\partial t}\right)\left(N_l A_l + M_l\right), \tag{4.9}$$

$$K = \begin{pmatrix} 1 & 2 + f_r\left(\tilde{h}\left(-\Omega\right) - 1\right) & 2 + f_r\left(\tilde{h}\left(-2\Omega\right) - 1\right) \\ 2 + f_r\left(\tilde{h}\left(-\Omega\right) - 1\right) & 1 & 2 + f_r\left(\tilde{h}\left(\Omega\right) - 1\right) \\ 2 + f_r\left(\tilde{h}\left(2\Omega\right) - 1\right) & 2 + f_r\left(\tilde{h}\left(\Omega\right) - 1\right) & 1 \end{pmatrix}, \tag{4.10}$$

$$\begin{pmatrix} M_{-1} \\ M_0 \\ M_1 \end{pmatrix} = \begin{pmatrix} \left(1 - f_r\left(1 - \tilde{h}\left(-\Omega\right)\right)\right) \cdot A_0^2 A_1^* \\ \left(1 - f_r\left(1 - \frac{\tilde{h}(-\Omega)+\tilde{h}(\Omega)}{2}\right)\right) \cdot 2A_1 A_{-1} A_0^* \\ \left(1 - f_r\left(1 - \tilde{h}\left(\Omega\right)\right)\right) \cdot A_0^2 A_{-1}^* \end{pmatrix}. \tag{4.11}$$

The numerical method presented in this section is useful for efficiently and accurately simulating nonlinear and dispersive interactions between frequency bands over large bandwidths. However, as can be deduced from the previous discussions the selection of spectral width and position of these bands is paramount to the success of the model and therefore some understanding of the system is required before the simulation. For example, if simulating degenerate FWM the position and separation of the bands would be determined by firstly investigating phase matching. In addition, when large powers are considered situations would arise where more bands need to be added to capture the influence of cascade FWM processes. The requirement of prior understanding of the system to operate the numerical model is not an attribute only exhibited by the BNLSE and in fact is something done when simulating GNLSEs.

4.1.2 Position of the Frequency Bands

As was discussed in the previous section an understanding of the system is required prior to the application of the BNLSE. An example is where to place the frequency bands in relation to each other when investigating FWM. In this subsection, the phase-mismatch equation is derived which is used to estimate the separation between the frequency bands in this thesis. Initially, the form of the BNLSE applicable only to CWs is depicted. Following this, the coupled amplitude equations presented in [10] are shown. Finally, the analysis presented in [9, 10] is used to derive the phase-mismatch equation which is then used to estimate the separation of the frequency bands within this thesis.

The BNLSE is applicable to pulses that are slowly varying compared to $h\left(t\right)$, which in silica fibres is 1 ps [9]. It therefore stands to reason that the mathematical model can be used for CWs and that the equation could be further simplified when describing such waves. To do this the amplitude is assumed to be CW, *i.e.* $A_l\left(z,t\right) = A_l\left(z\right)$ for $l = -1, 0, 1$. Applying these amplitudes to (4.9) results in the time derivatives vanishing and the equation to be simplified to:

$$\frac{dA_l}{dz} = \mathrm{j}\beta_l A_l + \mathrm{j}\gamma_l\left(N_l A_l + M_l\right), \tag{4.12}$$

where $\beta_l = \beta\left(l\Omega\right)$ is the propagation constant of the wave with $l = -1, 0, 1$. The mathematical model in this form is similar to the coupled amplitude models (with Raman nonlinearity included) found in the literature [71, 72]. Equation (4.12) could also be simplified further by setting the fraction contribution of the Raman nonlinearity to zero resulting in the equations detailed in [10]:

$$\frac{dA_{-1}}{dz} = \mathrm{j}\beta_{-1}A_{-1} + \mathrm{j}\gamma_{-1}\left(\left(|A_{-1}|^2 + 2|A_0|^2 + 2|A_1|^2\right)A_{-1} + A_0^2A_1^*\right), \tag{4.13}$$

$$\frac{dA_0}{dz} = \mathrm{j}\beta_0A_0 + \mathrm{j}\gamma_0\left(\left(2|A_{-1}|^2 + |A_0|^2 + 2|A_1|^2\right)A_0 + 2A_1A_{-1}A_0^*\right), \tag{4.14}$$

$$\frac{dA_1}{dz} = \mathrm{j}\beta_1A_1 + \mathrm{j}\gamma_1\left(\left(2|A_{-1}|^2 + 2|A_0|^2 + |A_1|^2\right)A_1 + A_0^2A_{-1}^*\right). \tag{4.15}$$

By assuming that the pump power at band $l = 0$ is larger than the power of the other bands *i.e.* $P_0 = |A_0|^2 \gg |A_1|^2, |A_{-1}|^2$ and assuming P_0 is constant throughout propagation (undepleted pump) the coupled amplitude equations can be written as:

$$\frac{dA_{-1}}{dz} = \mathrm{j}\left(\beta_{-1} + 2\gamma P_0\right)A_{-1} + \mathrm{j}\gamma A_0^2A_1^* \tag{4.16}$$

$$\frac{dA_0}{dz} = \mathrm{j}\left(\beta_0 + \gamma P_0\right)A_0 + \mathrm{j}\gamma 2A_1A_{-1}A_0^* \tag{4.17}$$

$$\frac{dA_1}{dz} = \mathrm{j}\left(\beta_1 + 2\gamma P_0\right)A_1 + \mathrm{j}\gamma A_0^2A_{-1}^*, \tag{4.18}$$

where $\gamma \approx \gamma_0, \gamma_1, \gamma_{-1}$.

To find the phase-mismatch equation for this model the following analysis is undertaken. Let

$$B_0(z) = A_0\exp\left(-\mathrm{j}\left(\beta_0 + \gamma P_0\right)z\right) \tag{4.19}$$

and

$$B_{(-1,1)}(z) = A_{(-1,1)}\exp\left(-\mathrm{j}\left(\beta_{(-1,1)} + 2\gamma P_0\right)z\right). \tag{4.20}$$

By taking the derivative of (4.20) and applying (4.16), (4.18) and (4.19) one gets

$$\frac{dB_{(-1,1)}}{dz} = \mathrm{j}\gamma B_0^2B_{(1,-1)}^*\exp\left(\mathrm{j}\left(\Delta\beta + 2\gamma P_0\right)z\right), \tag{4.21}$$

where $\Delta\beta = 2\beta_0 - \beta_1 - \beta_{-1}$. The change of power of the side-bands along propagation can then be found by differentiating the power of the side-bands with respect to distance and applying (4.21):

$$\frac{dP_{(-1,1)}}{dz} = 2\gamma\left|B_0^2\right||B_1||B_{-1}|\sin\left(\left(\Delta\beta + 2\gamma P_0\right)z + 2\theta_0 - \theta_1 - \theta_{-1}\right), \tag{4.22}$$

where B_l has been substituted by $|B_l|\exp\left(\mathrm{j}\theta_l\right)$ for $l = -1, 0, 1$. Equation (4.22) shows that the maximum transfer of energy to the side-bands occurs when

$$\left(\Delta\beta\left(\Omega\right)+2\gamma P_0\right)z+2\theta_0-\theta_1-\theta_{-1}=-\frac{\pi}{2}. \tag{4.23}$$

When one of the side-bands power is zero at $z = 0$ then the phases of the parametric waves arrange such that [10]:

$$2\theta_0-\theta_1-\theta_{-1}=-\frac{\pi}{2}. \tag{4.24}$$

A more detailed explanation of this equation is given in Chapter 5. *Ergo*, when such initial conditions are defined then (4.23) becomes the phase matching equation found in [9]:

$$\Delta\beta\left(\Omega\right)+2\gamma P_0=0. \tag{4.25}$$

This equation is solved for Ω in order to estimate the separation between the frequency bands. However, the analysis conducted in this subsection disregarded many of the enhancements of the BNLSE in favour of deriving (4.25). Yet, in conjunction with frequency bands of adequate spectral size the equation provides an elegant estimation of the frequency separation between the bands.

In the next section results from the BNLSE and the CNLSE are compared to those produced by the SM-GNLSE. It is shown that the BNLSE can recreate the equivalent results calculated by the SM-GNLSE something that the CNLSE fails to accomplish.

4.2 Comparison of Coupled Nonlinear Schrödinger Equations

4.2.1 Numerical Method

To compare the accuracy and efficiency of the BNLSE and CNLSE against the SM-GNLSE a numerical method was required. The research required to solve (4.1) for the SM-GNLSE, (4.9) for BNLSE and (4.9) but with $f_r = 0$ for the CNLSE. The fibre considered to simulate these models is a 14 m long LMA5-PM photonic crystal fibre manufactured by NKT Photonics. While the fibre is birefringent only propagation on the slow axis is considered. The fibre parameters were established by Zlobina et al. [78] and are quoted here as $\beta_3 = 6.765 \cdot 10^{-2}\,\mathrm{ps}^3\ \mathrm{km}^{-1}$, $\beta_4 = -1.002 \cdot 10^{-4}\,\mathrm{ps}^4\ \mathrm{km}^{-1}$, $\beta_5 = -3.671 \cdot 10^{-7}\,\mathrm{ps}^5\ \mathrm{km}^{-1}$ and $\gamma = 10\,\mathrm{W\ km}^{-1}$. The dispersion curve of this fibre is depicted in All these parameters are measured at the Zero Dispersion Wavelength (ZDW) of $\lambda_z = 1051.85\,\mathrm{nm}$. The fibre is also said to be silica based, therefore the Raman response function can be interpolated from [30] as discussed in Subsection 2.1.7.

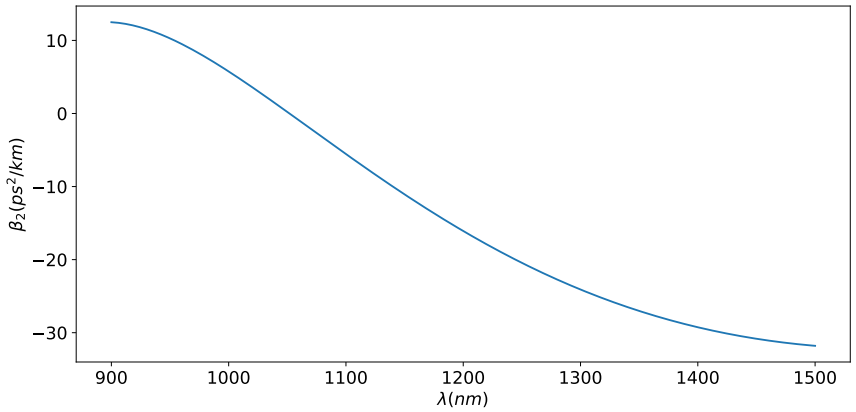

FIGURE 4.1: Dispersion of the LMA5-PM photonic crystal fibre with respect to wavelength.

The aim of this study is to compare the accuracy of the BNLSE/CNLSE against the SM-GNLSE, therefore the frequency grids of all numerical models are required to have the same frequency step df. To achieve this the frequency grid of the SM-GNLSE is created first and then the frequency bands of the BNLSE and CNLSE are selected from it. After this is done the Raman response functions for the BNLSE can be calculated accordingly prior to the pulse propagation.

Since all these equations are Schrödinger type in time and frequency they can be solved by the symmetrized SSFM as described in subsection 2.2.3. However, since the purpose of this section is to compare the results of the three models along propagation it is important for each equation to take the same step in space. The 4^{th} order RK method with constant step size dz is used instead of of the RK Cash-Karp algorithm in order to evaluate the nonlinear part of (2.52) [49]. The exclusion of the adaptive stepping algorithm results in the accuracy of the numerical methods being subject to the predetermined step in space dz. It is therefore required to establish that the SSFM method has converged for all equations solved for the dz picked. All the results shown in this chapter have been simulated for a constant $dz = 10^{-3}$ m. This value was selected because the models had converged for all situations investigated. An example of this convergence is shown in Figure 4.2 which portrays the relative error of idler power (investigated in subsection 4.2.3) for all three models with respect to dz. The relative error is calculated with respect to the idler power of a very small space step, $dz = 10^{-5}$ m.

By taking into account the above modifications the numerical model is solved as shown in Subsection 2.2.3. The source code used in this chapter is written in Python 3.6 and makes use of the NumPy and SciPy libraries. The Intel distribution for Python is also used because of the increased efficiency of the FFT algorithm it provides as discussed in Subsection 2.2.3. Since the aspiration behind this numerical method is to compare the three models on a FOPA minimal optimisation of the source code is required. Therefore, as was detailed in Section 2.2.1, the Numba compiler is nominally used in certain parts

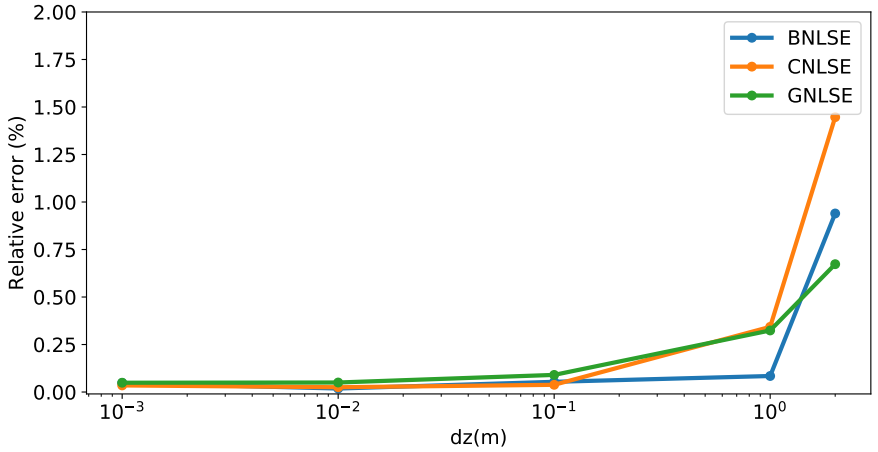

FIGURE 4.2: Relative error of the idler energy (for all the numerical models used) with respect to the space-step. The relative error is calculated with respect to the idler energy of each model for $dz = 10^{-5}$ m.

of the code to accelerate symmetrized SSFM method. The software described here was published under the MIT license and is listed 2^{nd} in Appendix A.3.

4.2.2 Nonlinear Phase Modulation

As previously discussed the primary distinction between the CNLSE and the BNLSE is that the later incorporates the Raman nonlinear effects between the frequency bands. Equation (4.10) indicates that the Raman dependent factors perturb the nonlinear phase modulation of the pulses, something that the CNLSE does not replicate. In this subsection the accuracy of the CNLSE/BNLSE is compared to the SM-GNLSE when investigating nonlinear phase modulation. Throughout propagation the total phase of a pulse can be calculated by $\phi(z,t) = \arg(A(z,t))$. The linear phase modulation along propagation can be calculated by $\phi_L(z,t) = -\beta z$. Therefore the nonlinear phase shift of a pulse along propagation can be calculated by $\phi_{\mathrm{NL}}(z,t) = \arg(A(z,t)\exp(\mathrm{j}\beta z))$.

To compare the nonlinear phase modulation that the three models produce two pulses are launched into the fibre described in the previous subsection. Two Gaussian pulses (pump and signal) with duration of $T_0 = 100$ ps are launched into the start of the fibre. The pump peak power is set at $P_p = 10$ W while that of the signal is set to $P_s = 100$ mW. The pump wavelength is $\lambda_p = 1051.35$ nm which is -0.5 nm from the ZDW. For these input parameters degenerate FWM is phase matched within the Raman gain bandwidth at a frequency separation of $F = 15.47$ THz. When evaluating the BNLSE/CNLSE models the central angular frequency of band 0 is set to that of pump ω_p and the signal is set at band 1. In order to capture any FWM between the pump, signal and newly created idler (set at band -1) the separation between the bands is considered equal, *ergo* the equation depicted in (4.9) is used to solve the BNLSE/CNLSE.

The initial investigation is conducted with a pump to signal frequency separation (and equivalent band separation) of $F = 60\,\text{THz}$ (signal wavelength of 868.59 nm). As can be seen in Figure 2.3 both the imaginary and real part of the Raman term $\tilde{h}(\omega)$ have a negligible effect upon the amplitude of the pulses at this frequency separation. Because the pump power is high relative to the signal power SPM will be the primary nonlinear effect that alters the phase of the pump. As stated earlier the SPM terms in the K matrix in the BNLSE are unity, therefore the nonlinear phase modulation would not change for the three numerical methods. On the other hand, the phase of the signal will be greatly affected by XPM from the pump. Figure 4.3 shows the nonlinear phase of the signal when simulated by the GNLSE (left) and the relative error between it and those calculated by using the CNLSE (middle) and BNLSE (right). The relative error of the CNLSE exhibits a trend of the same shape as the nonlinear phase change of the signal. This is because the XPM components of the K matrix have f_r set to zero which leads to the results calculated by the CNLSE deviating from those calculated by the GNLSE. This issue is not present in the results from the BNLSE which incorporates the Raman fractional contribution where the relative error is much smaller ($< 1\%$). This small numerical deviation is related to the frequency grid spacing of the models. Reducing the grid spacing df however is computationally challenging because of the large number of points that are required to simulate the GNLSE.

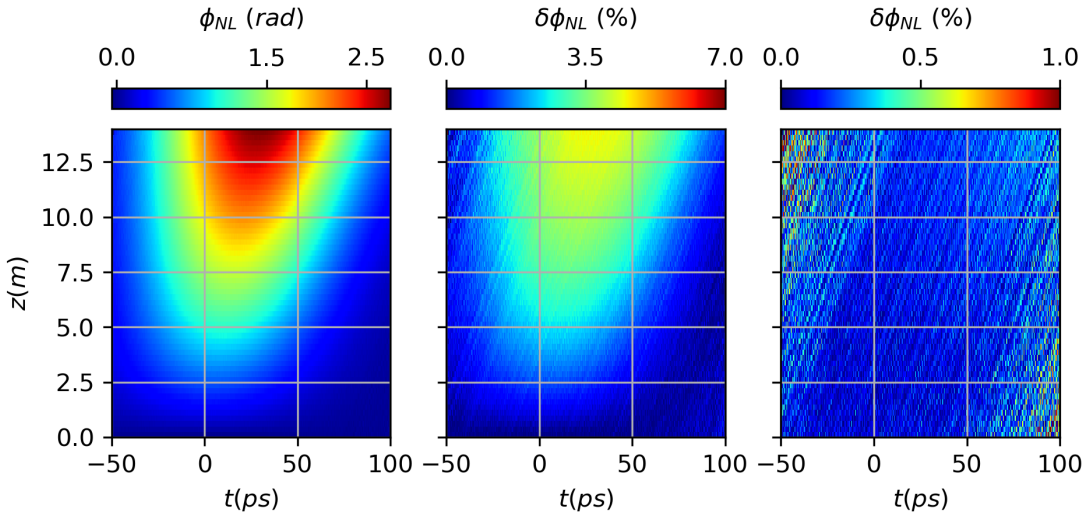

FIGURE 4.3: Nonlinear phase of the signal set at a frequency separation outside of the Raman gain bandwidth ($F = 60\,\text{THz}$) throughout propagation calculated using the GNLSE (left) and the relative error of the CNLSE (middle) and BNLSE (right) when compared to the GNLSE [24].

The successful replication of the nonlinear phase by the BNLSE is due to the inclusion of the fractional contribution of the Raman nonlinearity into the XPM factors. Because of the incorporation of Raman terms into the K and M matrices the BNLSE is also able to replicate the results of the GNLSE even when the pump and signal are set close enough for the Raman factors to perturb the phase. An example of such a case is is

shown in Figure 4.4 where the pump to signal separation is set to $F = 15.2\,\text{THz}$ (signal wavelength of 998.14 nm). As in the previous case, the nonlinear phase calculated by using the CNLSE deviates from that calculated by the GNLSE throughout propagation. The BNLSE, on the other hand, exhibits results very close to the GNLSE. It is worth mentioning that at this frequency separation the signal is set close to phase-matching and therefore an idler is created. Any phase change that this idler applies to the system is replicated by the BNLSE and CNLSE.

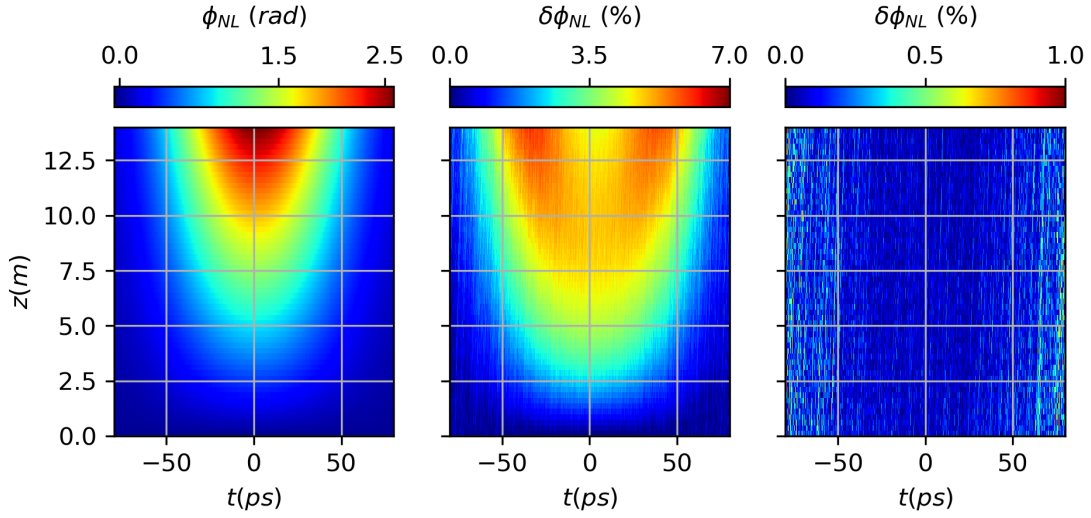

FIGURE 4.4: Nonlinear phase of the signal set at a frequency separation outside of the Raman gain bandwidth ($F = 15.2\,\text{THz}$) throughout propagation calculated using the GNLSE (left) and the relative error of the CNLSE (middle) and BNLSE (right) when compared to the GNLSE [24]. The waves powers and fibre paramaters are referenced in the text.

As can be seen in Figures 4.3 - 4.4 the BNLSE is capable of replicating the results of the SM-GNLSE when the waves are placed inside and outside the influence area of the Raman nonlinearity. It can also be seen that not incorporating the Raman dependent factors into the model, as in the case of the CNLSE, leads to compounding differences in the results when compared to those derived by the SM-GNLSE.

4.2.3 Four Wave Mixing

In the previous subsection it was shown that the addition of the Raman dependent factors to the BNLSE allows the model to replicate the nonlinear phase accumulated during pulse propagation expected from the SM-GNLSE. However, the main incentive behind the derivation of the BNLSE was the deviation of idler powers calculated by using CNLSE when compared to those calculated by using the SM-GNLSE. In this subsection, this deviation is highlighted and it is shown that the BNLSE can replicate the results of the SM-GNLSE.

As with the nonlinear phase modulation, the investigation is conducted for spectral separations between the bands that would result in high and low Raman induced influence between the waves. The input powers and pulse widths are the same as quoted in subsection 4.2.2 and the test is conducted upon the same fibre. In each case, the position of the frequency bands with respect to the central pump is determined by solving the phase mismatch equation (4.25).

The initial simulation has the pump situated at $\lambda_p = 1051.35\,\text{nm}$. The phase-matched frequency separation is found to be $F = 15.5\,\text{THz}$ by using (4.25). Therefore the wavelengths of the idler and signal are 997.15 nm and 1111.78 nm respectively. In the second simulation the pump is placed at $\lambda_p = 1046.85\,\text{nm}$ resulting in a frequency separation of the bands of $F = 42.5\,\text{THz}$ and thus the signal wavelength is 1229.28 nm while the idler wavelength is 911.57 nm. According to Figure 2.3 in the case of the first simulation the Raman induced perturbation will be relatively high while for the second it will be minimal.

For each of these simulations the power of the idler is measured throughout propagation by each of the models considered. The power of the idler is calculated by:

$$P(z) = \frac{1}{T_w} \int_{f_1}^{f_2} \left| \tilde{A}_1(z, f) \right|^2 df, \tag{4.26}$$

where T_w is the temporal width of the simulation window and, f_1 and f_2 are the start and end of the spectral window respectively. In the case of the BNLSE/ CNLSE this is the spectral width of the frequency band and temporal width of the equivalent temporal band.

Figure 4.5 shows the average idler power throughout propagation for all the models considered. Figure 4.5(a) portrays the power of the pulse for the first simulation (with a frequency separation of $F = 15.5\,\text{THz}$) and Figure 4.5(b) that of the second (with a frequency separation of $F = 42.5\,\text{THz}$). In both cases, the disregard of the Raman fractional contribution results in the energies calculated by the CNLSE deviating drastically from those of the BNLSE and SM-GNLSE. On the other hand, as in the case of the nonlinear phase modulation, the BNLSE consistently replicates the results of the SM-GNLSE.

As seen in Figure 4.5(b) the CNLSE's results seem to be closer to those of the BNLSE/SM-GNLSE than those of the Figure 4.5(a). The difference is because of the values exhibited by $\tilde{h}(\pm\Omega)$ at these frequency separations. In particular, for $F = 15.5\,\text{THz}$ $\text{Im}\left(\tilde{h}(2\pi F)\right) < 0$ which means that the Raman effect results in a transfer of energy from the idler to the pump.

For the simulations stated in this subsection the spectral and temporal distributions of the idlers calculated by using the BNLSE and SM-GNLSE are presented here for specific snapshots during propagation. Figure 4.6 is the case of $F = 15.5\,\text{THz}$ while

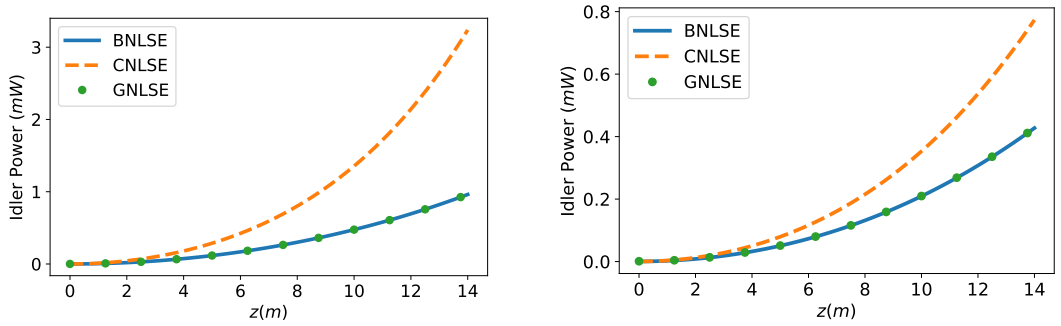

(a) (b)

FIGURE 4.5: Average power of the idler wave with respect to the propagation distance with signal inside, at $F = 15.5\,\text{THz}$, (left) and outside, at $F = 42.5\,\text{THz}$, (right) the Raman gain bandwidth [24]. The waves powers and fibre paramaters are referenced in the text.

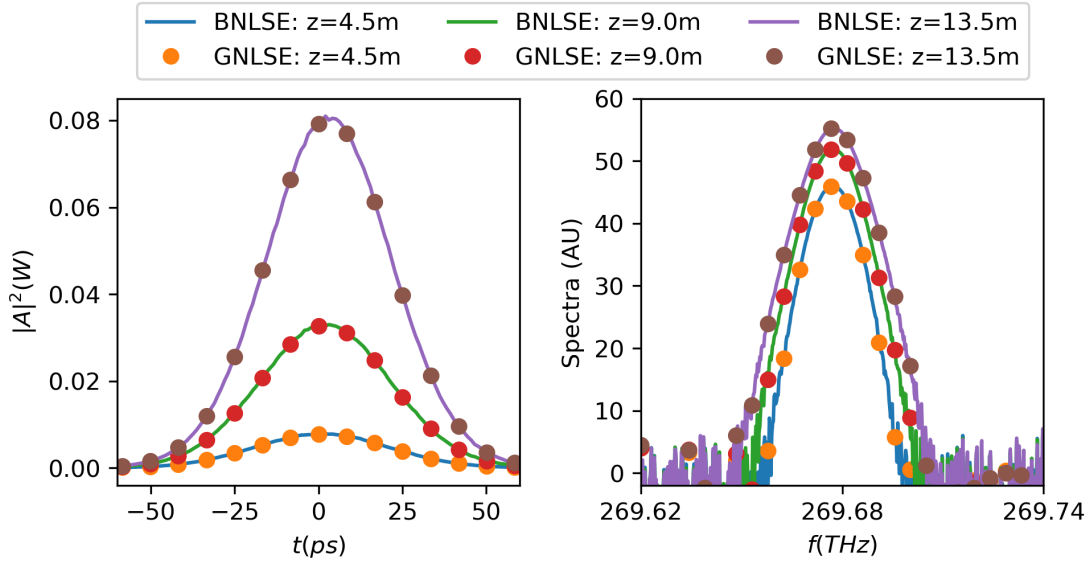

FIGURE 4.6: Temporal (left) and spectral (right, on a logarithmic scale) distribution of the idler wave with signal inside the Raman gain bandwidth, at $F = 15.5\,\text{THz}$ [24]. The waves powers and fibre paramaters are referenced in the text.

Figure 4.7 is for $F = 42.5\,\text{THz}$. As has been seen the pulses and spectra calculated by using the BNLSE reflect those calculated using the SM-GNLSE. Finally, as can be seen in Figure 4.7, the BNLSE predicts the dispersive phenomena of the time shift of the idler with respect to that of the pump.

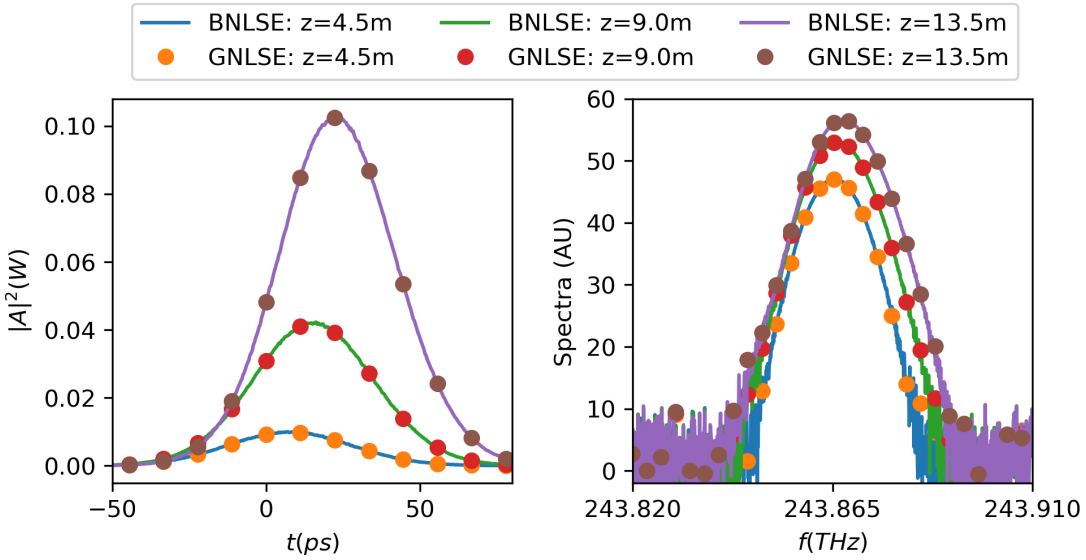

FIGURE 4.7: Temporal (left) and spectral (right, on a logarithmic scale) distribution of the idler wave with signal outside the Raman gain bandwidth, at $F = 42.5$ THz [24]. The waves powers and fibre paramaters are referenced in the text.

4.2.4 Computational Execution Times

In the previous subsections it was shown that the BNLSE provides a distinct enhancement to the CNLSE in terms of accurately replicating the results of the GNLSE. However, the primary incentive behind the use of coupled Schrödinger equations is the decreased numerical execution time and memory demands they can provide. In order to show this, the execution times of all the models used in this chapter are measured for a varying frequency step df. This test is conducted for the inputs of the wideband FWM simulation described in subsection 4.2.3. The frequency window of the GNLSE is set to 170.2 THz and the width of each band of the CNLSE/BNLSE is set to 5.3 THz. The execution times are measured on the desktop machine described in Section 2.2.1.

Figure 4.8 depicts the average execution time (over 100 repetitions) of the CNLSE, BNLSE, GNLSE with $f_r = 0.18$ and GNLSE with $f_r = 0$ with respect to the frequency step df. The reason for considering the GNLSE with and without the Raman factor is because in order to evaluate the Raman dependent term in (4.1) a convolution needs to be calculated at each step. This, in turn, increases the execution time of the GNLSE owing to the increased number of FFTs that are required. It is therefore of interest to evaluate the execution time of both cases and compare them to those measured by using the CNLSE/BNLSE.

For all the frequency steps considered the CNLSE/BNLSE exhibits lower execution times than the GNLSE. The increased efficiency is attributed to the decreased number of points that the CNLSE/BNLSE requires to maintain the same spectral resolution as

the GNLSE. The BNLSE in particular exhibits a 10 times speed-up against the GNLSE with $f_r = 0.18$ for lower df.

As said earlier in order to solve the CNLSE f_r is set to 0 in (4.9). This, in turn, allows the equation to be simplified which in turn results in it being computationally accelerated. This is why the CNLSE is slightly faster than the BNLSE for all df considered. The difference in execution time is reduced however as the number of points are increased since the execution times of the FFT's and matrix arithmetics for larger size matrices become more computationally detrimental than the assortment of Raman factors.

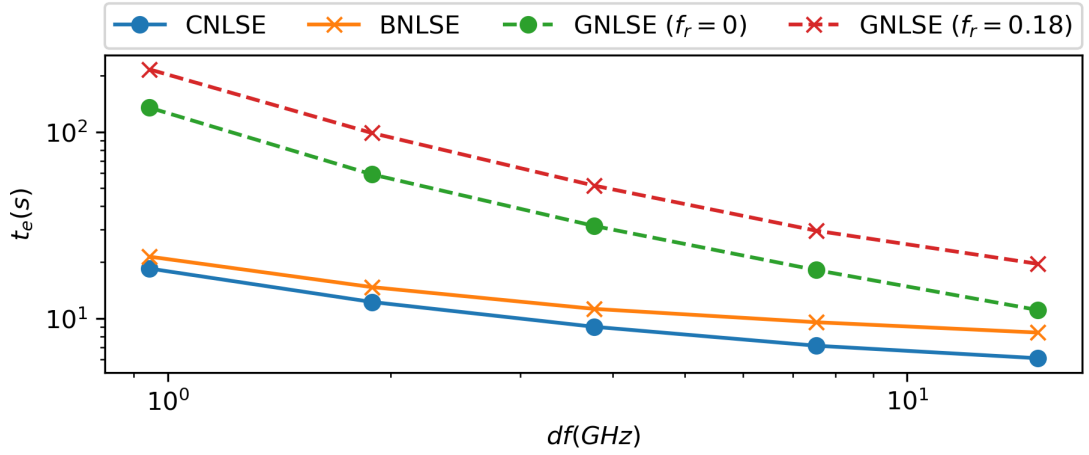

FIGURE 4.8: Average execution times of the SM-GNLSE (with $f_r = 0, 0.18$), CNLSE and BNLSE for a varying frequency step size [24]. The simulation parameters are referenced in the text.

4.3 Conclusion

In this chapter the BNLSE was derived and validated against the GNLSE. By making use of this numerical method the dispersive and nonlinear interactions of waves that are placed over wide frequency separations can be accurately and efficiently simulated. It was also shown that setting the fractional contribution of the Raman nonlinearity to zero results in the numerical method greatly deviating from the equivalent results of the SM-GNLSE and that the BNLSE corrects this by including Raman dependent factors into the XPM and FWM.

Within this chapter, it has been shown that the use of the BNLSE significantly decreases the execution time of a pulse propagation simulation while replicating the results of the GNLSE. It is important to mention that the speed-up shown in Section 4.2.4 is representative of the three-band BNLSE. For higher powers, the number of bands needs to be increased because of the need to simulate cascade FWM processes. This, in turn, results in the increase in the number of matrix arithmetics at every step. Additionally, in order to ascertain that the waves are contained within the frequency band and to

avoid errors stemming from the periodic boundary conditions of the FFTs the width of the frequency band needs to be maintained sufficiently large. However, for each increase of the bands' width, the number of points needs to be increased to maintain the desired spectral resolution. As can be concluded care needs to be taken to establish that the number, spectral width and spectral resolutions are sufficient to the maintain accuracy and efficiency of a simulation.

The BNLSE derived has no theoretical limit on the frequency separation between the bands and has applications in simulations over wide frequency bands. Also, since it was derived from the SM-GNLSE it is only applicable to single mode operations. A fibre, however, is only single mode within certain parts of the spectrum [19]. Thus, it stands to reason that an enhanced BNLSE that incorporates multiple spatial modes would provide a more robust model for simulating wideband interactions between waves. Such an equation could be derived in a similar way as the BNLSE was but by using the MM-GNLSE as a starting point.

The BNLSE derived and validated in this chapter forms a fundamental building block of the numerical model described in Chapter 5. The reasons being that the equation does not have the limitation of the non-depleted pump approximation, it incorporates Raman effects between bands and is efficient in its numerical evaluation. All these enhancements are paramount when investigating FOPOs.

Chapter 5

Single Mode Fibre Optical Parametric Oscillator

FOPAs have long been used for frequency conversion in single mode fibre systems [9]. One of the reasons behind their attractiveness is that they can operate over large bandwidths [79]. However, the efficiency of this broadband operation is subject to phase matching which, as was discussed in Chapter 2, is highly dependent upon fibre parameters such as the diameter and refractive index profile. Because of fabrication errors, all optical fibres exhibit a non-uniformity for these parameters along the propagation axis. This in turn results in the efficiency of FOPAs being reduced, particularly for long length fibres [80]. As was briefly discussed in Chapter 3 the decrease in efficiency can be cut back by using short length HNLFs. The conversion efficiency can also be increased if part of the spectrum outputted from the fibre is recirculated back in to it. This results in the optical power of the oscillating wave increasing at every round trip and the configuration essentially forms a SM-FOPO [81].

In SM-FOPOs, at every oscillation the power of the parametric sidebands is increased and this continues until the losses of the system counteract the parametric gain. The selective recirculation of part of the spectrum can be beneficial in applications of a single pump SM-FOPO configuration. In such a system the oscillator is pumped with a single pump and modulation instability type FWM processes (as shown in Figure 2.2(c)) facilitate the creation of the signal and idler. One of these sidebands is recirculated and the other forms the output. The selective recirculation of one of the sidebands can reduce amplification of other waves such as those resulting from SRS. The use of these oscillators can also be beneficial for energy conversion over large bandwidths since the recirculating sideband is used as a seed (as shown in Figure 2.2(b)) in the FWM process and encourages idler amplification. The oscillation of signals means that the optical system need not be seeded but can be built up from noise. *Ergo*, the operation of the oscillator does not have to be subject to the presence of seeded laser sources at exotic

wavelengths like FOPAs require[82]. Thus, a single pump SM-FOPO can operate over an ultra-large bandwidth subject however to phase matching and material transparency.

The first time a SM-FOPO was investigated experimentally [83] and theoretically [84] was by Nakazawa et al. The apparatus consisted of a ring-type SM-FOPO with a silica fibre as a gain medium and a beam splitter as a way of selecting part of the spectrum to be recirculated. The SM-FOPO was singly pumped (unseeded configuration), and the FWM process occurring in the fibre was equivalent to what is shown in Figure 2.2(c). Within the oscillator, one of the parametric waves was recirculated while the other formed the output. In following years similar types of SM-FOPOs have been extensively studied with both pulsed [85–88] and CW [89–95] pump input.

The FOPO presented in this chapter is pumped by a CW. In order to scrutinise the performance of the system, the CEs and operational wavelengths of CW pumped SM-FOPOs presented in recent studies are detailed here. Xu et al. demonstrated a Raman assisted all-fibre parametric oscillator pumped around 1550 nm. In detail, they quote a maximum internal CE (defined as the ratio of powers of the parametric wave within the oscillator and the inputted pump) approaching 50 % over a tuning range of 240 nm [96]. An internal CE of $\approx$ 30 % was also quoted for the FOPO described by Marchic et al. while converting light over a range of $\approx$ 5 nm from a pump of 1550 nm [81]. An (external) CE of $\approx$ 15 % was achieved by Matos et al. for converting energy over a few nanometres from the pump which was set to $\approx$ 1550 nm [97]. An internal CE of 10 % was achieved by Xu et al. to convert light from a pump of $\approx$ 700 nm to lower wavelengths detuned up to $\approx$ 550 nm [89]. Recently, Zlobina et al. demonstrated a CE of approximately $\approx$ 15 % to convert light from 1050 nm to $\approx$ 900 nm [91] using an all-fibre FOPO. In a continuation of this study the CE was increased to $\approx$ 17 % by replacing the WDMCs that were used to recirculate the signal with polarisation maintaining WDMCs [92]. In all the above studies it was found that the CE of the oscillator is subject to the transmittance of the circulating parametric wave, the power of the pump and nonlinear gain of the fibre.

While a plethora of numerical investigations have targeted FOPAs not many have studied SM-FOPOs [10]. Most of the computational models have simulated each part of the SM-FOPO sequentially that is to say treating the pulse propagation and recirculation parts of the model separately. In the case of a CW pumped SM-FOPO the simplest approach in modelling the pulse propagation part is by using the coupled amplitude equations (4.13) - (4.15) [10, 69, 98, 99]. However, this approach both requires prior knowledge of the wavelengths of the signal and idler and also neglects the fact that the spectral position with the highest gain will change with respect to the power of the parametric waves involved (as can be seen in (4.25)). Therefore to more accurately simulate SM-FOPOs the pulse propagation part of the oscillator can be modelled by using the GNLSE as was shown in [82, 100–103] or coupled GNLSE as shown in [70, 104, 105]. The use of the GNLSE, however, can become numerically challenging when the SM-FOPO

is investigated over large bandwidths. Therefore the use of coupled GNLSEs (or the BNLSE) is more suitable for simulating SM-FOPOs [11, 24].

In this chapter the numerical modelling of a single mode SM-FOPO is presented. Initially the optical apparatus is introduced along with the sub-modules that comprise it. All the numerical models that are used to simulate these sub-modules are presented and it is shown how their accumulation forms the SM-FOPO model. Following this, the validation of each of the numerical modules used is illustrated prior to the simulation of the SM-FOPO. The oscillator is then simulated for different pump wavelengths and powers for a single pump input (unseeded configuration) and with the addition of a seed (seeded configuration). Finally, the CE and RIN of the oscillator is presented and their behaviour is characterised.

The study shown in this chapter has been the subject of two conference presentations (listed 4 and 5 in Appendix A.2), a journal article (listed 3 in Appendix A.1) and an accompanying published software (listed 1 in Appendix A.3).

5.1 Optical System

The SM-FOPO apparatus studied in this chapter is depicted in Figure 5.1. The system comprises of two WDMCs (WDMC1 and WDMC2), two phase modulators (PM_1 and PM_2), a σ loss at position (c) and a HNLF. The oscillator is configured such that, following two sidebands being created/amplified by degenerate FWM in the HNLF, one (signal) is recirculated, and the other (idler) forms the output.

To achieve the recirculation of one of the sidebands the WDMCs are set-up as follows. WDMC1 is defined such that all the optical power is transferred from port (i) to port (iii) at the pump frequency and equivalently from port (ii) to port (iv) for the signal frequency. Furthermore, WDMC2 is arranged such that the idler power is outputted from the SM-FOPO cavity (from port (i) to port (iii)) and that the signal is recirculated (from port (i) port (iv)). The σ loss at position (c) introduces a global (with respect to the spectrum) loss and is used to represent all the losses of the optical system. This loss, in combination with the WDMCs, dictates the transmittance of the signal within the oscillator.

The phase modulators are introduced to the optical apparatus to minimise phase sensitive reductions to the conversion efficiency. PM_1 operates in order to avoid back conversion of the sidebands to the pump which can occur when more waves than the signal are oscillated in the fibre cavity [106–108]. PM_2 is required if the oscillator is seeded. It is introduced to the system in order to ensure that the recirculating signal constructively interferes with the inputted seed within WDMC1. Further details on the operation and modelling of the Phase Modulators (PM) are outlined in subsections 5.2.3, 5.2.4.

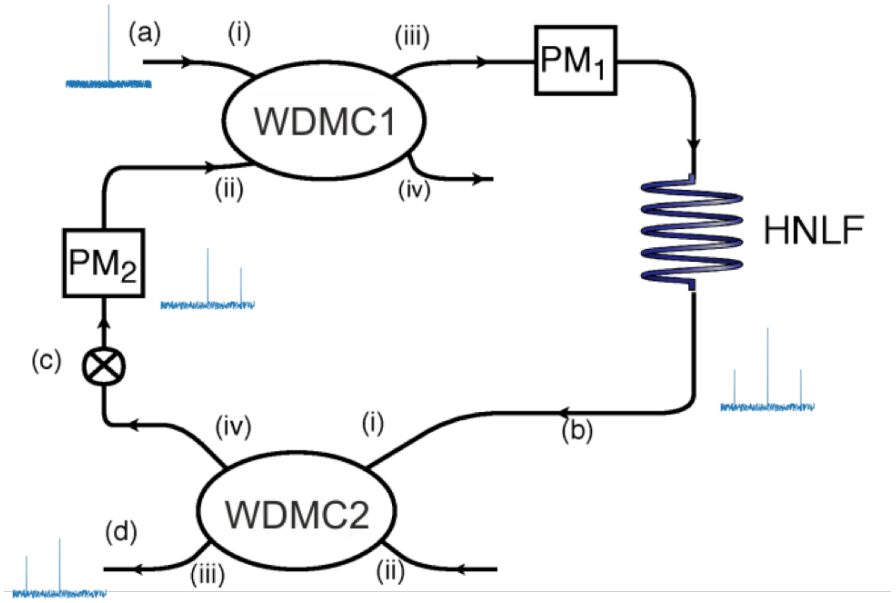

FIGURE 5.1: Optical system of the single mode fibre optical parametric oscillator with two wavelength division multiplexing couplers [11, 109].

Ultimately the configuration of these subsystems would result in the oscillator shown in Figure 5.1 operating as follows. A pump pulse is inputted into the system at position (a). Most of the power of the pump is passed through from port (i) to port (iii) of WDMC1 because of the aforementioned configurations of this WDMC. The spectrum is then passed through PM_1 where optimum phases (with respect to maximizing the gain of the sidebands) of the pump and sidebands are set. The output field from PM_1 then propagates into the HNLF and sideband amplification is achieved through FWM. Afterwards the spectrum is inserted into WDMC2 at port (i), the idler (and part of the pump) is then outputted at port (iii) forming the output of the oscillator at (d). On the other hand the signal (and residual pump) is outputted from WDMC1 at port (iv) and afterwards has a σ loss applied to it at (c). The spectrum then passes through PM_2 where the phase is modulated to make sure that no destructive interference occurs at WDMC1 between the signal and seed (in the case of the seeded oscillator configuration). The spectrum is then combined with the input at WDMC1 and the next oscillation commences.

Finally, assume that the gain of the signal is larger than its losses. At every oscillation, it is expected that the signal will be amplified within the cavity until the losses counteract the gain. The presence of a large signal power within the cavity is beneficial since it will mediate the conversion of energy to the outputted idler from the pump and therefore increase the CE of the oscillator. In the next section, the numerical models used to describe each subsystem of the oscillator are discussed, and it is shown how their aggregation simulate the SM-FOPO as a whole.

5.2 Numerical Model

5.2.1 Pulse Propagation

The SM-FOPO described in the previous section is comprised of multiple subsystems that have to be modelled separately. Principal amongst these is the pulse propagation through the HNLF where the energy from the pump is transferred to the signal and idler.

For this chapter the HNLF is considered to be single mode throughout the investigated bandwidth. While most conventional fibres can have a different number of modes in separate parts of the spectrum only a Photonic Crystal Fibre (PCF) is considered in this study and these type of fibres can be made to be single mode over a substantial bandwidth [89]. Therefore only single-mode pulse propagation models need to be considered. Furthermore, the spectral position and linewidth of the parametric waves generated are dependent upon the gain which is in turn dependent upon the dispersion and power[9]. Because of this, the SM-GNLSE was initially considered a candidate to model the pulse propagation part of the oscillator. However, the parametric waves within an oscillator can be separated over ultra large bandwidths and, as stated earlier, the numerical evaluation of the SM-GNLSE with the SSFM requires a linearly spaced grid. Therefore, to accurately simulate the subsystem a considerable number of grid points may be required, which can very quickly become computationally unfeasible. It is this challenge that led to the derivation of the BNLSE described in Chapter 4. This equation is superbly suited to simulate pulse propagation through the fibre since, as was discussed in the previous chapter, it encompasses the advantages of the SM-GNLSE without incurring the same computational challenges.

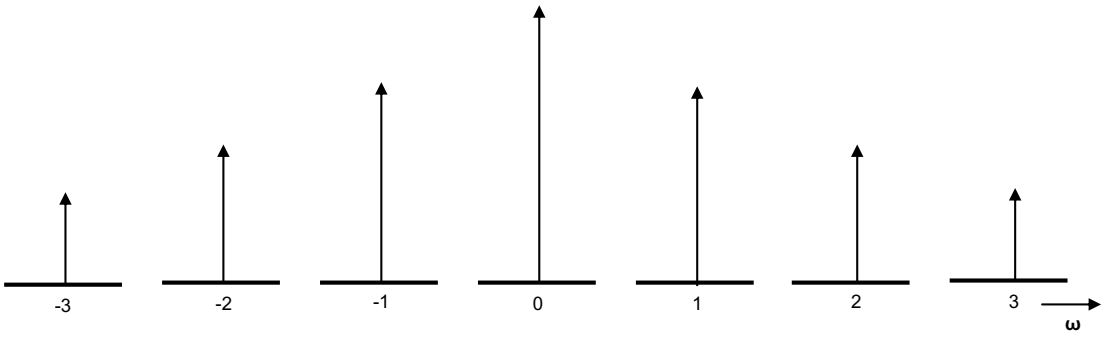

FIGURE 5.2: Equally spaced seven frequency bands of BNLSE used in the single mode SM-FOPO.

Initial investigations upon the system showed that the presence of cascade FWM processes can create instability in the output of the system at every round trip with respect to the number of round trips [102, 103]. Therefore it is vital, particularly when large input powers are investigated, to consider cascade FWM processes within the model.

This is done in this chapter by including more frequency bands in the BNLSE. However, it is worth mentioning that a small increase in the number of frequency bands can result in a substantial increase in the number of matrix multiplications and by extension increase computational execution times. In this chapter 7 bands are chosen as shown in Figure 5.2 allowing the creation of two cascade waves for both the idler and the signal.

As shown in Chapter 4 the amplitude is expressed as the summation over multiple bands. However, the number of bands is raised to 7. Additionally, since FWM is the driving physical phenomena investigated here the separation between the centres of the frequency bands are considered equally spaced. With these adjustments taken in to account the amplitude is expressed as:

$$A\left(z,t\right)=\sum_{l=-3}^{3}A_l(z,t)\exp(-\mathrm{j}l\Omega t). \tag{5.1}$$

Applying (5.1) to (4.1) results in the 7 band BNLSE [11]:

$$\begin{aligned}\frac{dA_l}{dz}=\mathrm{j}\sum_{n\geq 2}\frac{\beta_n}{n!}\left(\mathrm{j}\frac{\partial}{\partial t}-l\Omega\right)^n A_l+\mathrm{i}\gamma_l\left(1+\frac{\mathrm{j}}{\omega_l}\frac{\partial}{\partial t}\right)\times\\ \sum_{l+m=n+k}A_kA_m^*A_n\left\{1-f_r+f_r\tilde{h}\left[(m-l)\Omega\right]\right\},\end{aligned} \tag{5.2}$$

where $\omega_l=\omega_0+l\Omega$ for $l=-3,-2,...,3$. The second sum in the equation iterates over all indices $k,m,n=-3,...,3$ such that energy is conserved in the FWM processes *i.e.* $l+m=n+k$. Finally, as in Chapter 4, the frequency separation between the centres of the bands is calculated by solving (4.25).

5.2.2 Optical Recirculation and Loss

While the 7 band BNLSE is used to simulate the pulse propagating through the fibre the recirculation of the power is done by the WDMCs. In subsection 2.1.3 it was discussed that WDMCs can be used to output specific wavelengths to different parts of an optical system and, as mentioned in subsection 5.1, this attribute is used to recirculate and output the signal and idler within the oscillator system.

As was detailed in subsection 2.1.3 the WDMCs can be modelled by using the SMR. This model assumes that the waves propagate in one direction *i.e.* any back-propagating light is neglected. Additionally, it is assumed that the polarisation of the mode is maintained throughout propagation. These approximations are shared by the SM-FOPO model.

As can be seen from (2.33) the transmittance path of the spectrum is dependent upon the function inside the trigonometric functions which is linearly interpolated here as:

$$\kappa\left(f\right)L=\zeta f+\psi, \tag{5.3}$$

where ζ and ψ can be set depending on the definition of the WDMC system. In the SM-FOPO apparatus the WDMCs are used to change the path of different parts of the spectrum. In this scheme a WDMC is defined by the following constraint. All the optical power inputted into the WDMC through port (i) is outputted via port (iii) at a frequency f_1 and the equivalent occurs from ports (i) to (iv) at a frequency f_2. Because of the setup of the SMR this would also mean that the transmittance between ports (ii) and (iii) is maximum at f_1 (and likewise between ports (ii) and (iv) at f_2). The constraint can be mathematically expressed by using (2.33) and (5.3) as:

$$\begin{pmatrix} P_{(\mathrm{iii})} \\ P_{(\mathrm{iv})} \end{pmatrix} = \begin{pmatrix} \left|A_{(\mathrm{iii})}\right|^2 \\ \left|A_{(\mathrm{iv})}\right|^2 \end{pmatrix} = \begin{pmatrix} \cos\left(\zeta f_1 + \psi\right)\left|A_{(\mathrm{i})}\right|^2 \\ \sin\left(\zeta f_2 + \psi\right)\left|A_{(\mathrm{ii})}\right|^2 \end{pmatrix} = \begin{pmatrix} \left|A_{(\mathrm{i})}\right|^2 \\ \left|A_{(\mathrm{ii})}\right|^2 \end{pmatrix}$$

or

$$\begin{pmatrix} \cos\left(\zeta f_1 + \psi\right) \\ \sin\left(\zeta f_2 + \psi\right) \end{pmatrix} = \begin{pmatrix} 1 \\ 1 \end{pmatrix}. \tag{5.4}$$

By solving this system of equations ζ and ψ can be expressed with respect to the chosen frequencies f_1 and f_2 as:

$$\zeta = \frac{\pi}{2}\frac{1}{f_2 - f_1}, \tag{5.5}$$

$$\psi = -\frac{\pi}{2}\frac{f_1}{f_2 - f_1}. \tag{5.6}$$

When this analysis is applied to (2.33) the SMR for the WDMC can be expressed as

$$\begin{pmatrix} A_{(\mathrm{iii})}\left(f\right) \\ A_{(\mathrm{iv})}\left(f\right) \end{pmatrix} = \begin{pmatrix} \cos\left(K\left(f\right)\right) & \mathrm{j}\sin\left(K\left(f\right)\right) \\ \mathrm{j}\sin\left(K\left(f\right)\right) & \cos\left(K\left(f\right)\right) \end{pmatrix} \begin{pmatrix} A_{(\mathrm{i})}\left(f\right) \\ A_{(\mathrm{ii})}\left(f\right) \end{pmatrix}, \tag{5.7}$$

where $K\left(f\right) = \zeta f + \psi$ and the transmission between ports varies with respect to wavelength and frequency as shown in Figure 5.3.

As seen above only two parameters are required to define the WDMC within the SM-FOPO model, f_1 and f_2 (or equivalent wavelengths λ_1 and λ_2). For the sake of clarity such a WDMC is expressed as WDMC $\left(\lambda_1, \lambda_2\right)$ hereafter. Within the SM-FOPO model (5.7) is used to simulate the waves passing through the defined WDMCs. It is worth mentioning that when there is no input from one of the input ports random quantum noise is inputted in order to make sure that spectral energy is never lower than the noise floor (as describe in subsection 2.1.8).

Finally, the model of the SMR is also used to model the σ loss mentioned in Section 5.1. However, the loss within this subsystem is assumed to be constant with respect to frequency. The SMR can therefore be simplified and the resulting model used to describe

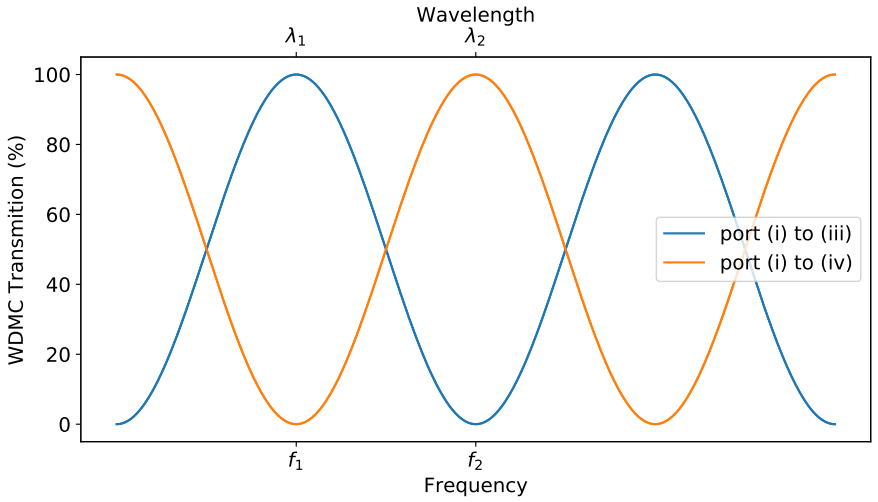

FIGURE 5.3: Transmission between ports in a WDMC.

the application of the σ loss is

$$A_{(\mathrm{ii})}(f) = \sqrt{10^{0.1\alpha}} A_{(\mathrm{i})}(f) + \mathrm{j}\sqrt{1 - 10^{0.1\alpha}}\nu(f), \tag{5.8}$$

where $A_{(\mathrm{ii})}(f)$, $A_{(i)}(f)$ are the output and input from the σ loss respectively, α is the σ loss in units of dB and $\nu(f)$ is the random quantum noise floor as described in subsection 2.1.8.

5.2.3 Phase Modulation for Parametric Amplification

As has been stated in the previous sections FWM is used within the SM-FOPO to transfer energy from the pump to the sidebands one of which is recirculated. This premise assumes that the build-up of recirculating energy within the fibre cavity will mediate energy transfer to the output of the oscillator. However, while power is instrumental in increasing the efficiency of the apparatus the phases of the waves involved can lead to energy being back converted from the sidebands to the pump abating the CE.

To illustrate the importance of phase in the FWM process within the fibre the CW approximation is applied. By making use of (4.13) and (4.15) the derivative of power of the sidebands during propagation can be found by:

$$\frac{dP_{(-1,1)}}{dz} = 2\left|\gamma_{(-1,1)} A_0^2 A_{-1} A_1\right| \cos(\phi), \tag{5.9}$$

where [10]

$$\phi = 2\theta_0 - \theta_{-1} - \theta_1 + \frac{\pi}{2} \tag{5.10}$$

and θ_l are the respective waves $l = -1, 0, 1$. If the powers of all waves involved in the FWM processes are not zero at the start of the fibre ($z = 0$) then (5.9) is maximum

when $\phi = 0$ or

$$2\theta_0 - \theta_{-1} - \theta_1 + \frac{\pi}{2} = 0. \tag{5.11}$$

Ergo, when (5.11) is fulfilled the maximum amount of power is transferred from the pump to the sidebands at every step (assuming phase matching occurring between the three waves). If on the other hand the equation is not satisfied then the sidebands either increase by a smaller amount (when $0 < \phi < \pi/2$) or energy is transferred from the sidebands to the pump (for $\pi/2 < \phi < \pi$).

The above analysis assumes the amplitudes of the waves involved is not zero before propagation through the fibre. In the premise of the SM-FOPO shown in this chapter, such a configuration occurs when not all the idler power is outputted from the cavity at every round trip. If through fine-tuning of the SM-FOPOs parameters all the idler is ousted such that one of the sidebands is zero before propagation through the HNLF then the phase of the newly formed idler will shift to accommodate (5.11). This can be verified by setting one of the sidebands in (4.13) and (4.15) to zero and solving the equations analytically.

In situations where the idler is recirculated along with the signal within the cavity, the relative phases of one of the sidebands needs to be altered to satisfy (5.11). Within the optical system described in this chapter, this is done in PM_1 by applying a phase shift to the idler at every round trip. While this can be considered a non-physical feature to the system its purpose is to simulate the oscillator on or close to resonance.

Finally, the relationship shown in (5.11) is derived for CWs. The model in this chapter, however, simulates the oscillation of frequency bands and therefore the relationship needs to be extended to incorporate frequency grids. From the seven frequency bands $-1, 0, 1$ are selected to be the signal, pump and idler respectively. Each grid point within the frequency bands forms FWM partners with equivalent ones of other bands according to (2.47). Assuming that the pump is CW (*i.e.* represented by a single point in the frequency grid) then the phase modulation that needs to be added to the complex argument of the signal at each grid point of the idler band is:

$$\theta_{\text{mod}} = 2\theta_0 - \theta_{-1} - \text{reversed}\,(\theta_1) + \frac{\pi}{2}, \tag{5.12}$$

where $\theta_{(-1,1)}$ are vectors of the frequency bands complex arguments and the function reversed() reverses the order of the vector. By applying this grid dependent optimisation, the amplification of each point within the frequency bands is maximised. Applying this vector type solution eliminates errors that would stem from the position of the highest gain changing with respect to power as is hinted by the analysis conducted in Section 4.1.2.

5.2.4 Constructive Interference in the Wavelength Division Multiplexing Couplers

In the previous subsection, it was shown that the phases of the waves involved in FWM influence the CE of the SM-FOPO. Likewise, the phases of the waves inputted into the WDMCs can affect their output power and by extension this can alter the efficiency of the SM-FOPO.

Making use of (5.7) the output powers at $P_{(\mathrm{iii})}$ and $P_{(\mathrm{iv})}$ are calculated to be:

$$P_{(\mathrm{iii})} = \cos^2\left(K\left(f\right)\right)\left|A_{(\mathrm{i})}\right|^2 + \sin^2\left(K\left(f\right)\right)\left|A_{(\mathrm{ii})}\right|^2 + \left|\sin\left(2K\left(f\right)\right)A_{(\mathrm{ii})}A_{(\mathrm{i})}\right|\sin\left(\theta_{(\mathrm{ii})} - \theta_{(\mathrm{i})}\right), \tag{5.13}$$

$$P_{(\mathrm{iv})} = \sin^2\left(K\left(f\right)\right)\left|A_{(\mathrm{i})}\right|^2 + \cos^2\left(K\left(f\right)\right)\left|A_{(\mathrm{ii})}\right|^2 - \left|\sin\left(2K\left(f\right)\right)A_{(\mathrm{ii})}A_{(\mathrm{i})}\right|\sin\left(\theta_{(\mathrm{ii})} - \theta_{(\mathrm{i})}\right), \tag{5.14}$$

where θ_{i}, θ_{ii} are the complex arguments of amplitudes $A_{(\mathrm{i})}$ and $A_{(\mathrm{ii})}$ (the frequency dependence has been removed for clarity). These equations show that if the power inputted through both $P_{(\mathrm{i})}$ and $P_{(\mathrm{ii})}$ is not zero and the WDMC is not perfectly aligned for the frequency in question then the output power at $P_{(\mathrm{iii})}$ and $P_{(\mathrm{iv})}$ depend upon the phases of the pulses.

For the oscillator considered in this chapter phase dependency of the WDMCs is negligible in WDMC2 since the input at port (ii) is at the noise floor and therefore the last terms in (5.13) and (5.14) will be insignificant. This is not always the case however for the WDMC1. In the single pump configuration (only a single pump is inputted into the SM-FOPO) the inputted pump at $P_{(\mathrm{i})}$ will be combined within the WDMC with the residual pump from the previous oscillation. However, for the pump wavelengths investigated in this chapter $K\left(f_p\right) \approx 0$, where f_p is the frequency of the pump. Thus, the last terms in (5.13) and (5.14) are negligible for all frequencies when simulating a single pump configuration SM-FOPO.

On the other hand, the phase-dependent power at $P_{(\mathrm{iii})}$ can be detrimental to the CE of the SM-FOPO when the signal of the oscillator is seeded (seeded configuration). This is because the last term of (5.13) is not negligible for the signal frequencies and therefore the oscillating signal can destructively interfere with the inputted seed within WDMC1. Therefore, for this scenario the phase of the signal needs to be modulated. This is done within the SM-FOPO apparatus at PM_2 for every round trip. The modulator asserts that $P_{(\mathrm{iii})}$ is maximum for the signal frequency or that:

$$\theta_{(\mathrm{ii})} - \theta_{(\mathrm{i})} - \frac{\pi}{2} = 0 \tag{5.15}$$

therefore the complex argument of the oscillating signal is modulated by adding θ_m to it where

$$\theta_m = \theta_{(\mathrm{i})} - \theta_{(\mathrm{ii})} + \frac{\pi}{2}. \tag{5.16}$$

Finally, it is worth mentioning that like the phase modulation described in subsection 5.2.3 θ_m is a vector and needs to be calculated and added to the phase of the signal for every grid point. However, as stated earlier, this phase modulation is only required for the seeded oscillator configuration. For this thesis only a CW seed is considered therefore only a single point of the oscillating signal needs to be modulated. However, within the numerical model used in this thesis all the points in the signals frequency band are modulated.

5.2.5 Software and Optimisation

The source code used to simulate the SM-FOPO models the subsystems mentioned above sequentially until a steady state is reached as was described in Section 5.1. The pulse is distributed over 7 frequency bands because of the application of the 7-band BNLSE *i.e.* the frequency array (and equivalent pulse) is modelled as an array of shape $[7, n_t]$ where n_t is the number of frequency points sampled in each frequency band. The numerical models of the WDMCs and PMs are written as described in the previous subsections and also are modified to accommodate the seven frequency bands.

As with the numerical models described in the previous chapters the source code to describe the SM-FOPO is written in Python 3.6. The code makes extensive use of the NumPy and SciPy modules for matrix arithmetics and scientific functions respectively. The h5Py module is used to export data for every round trip at different sections of the SM-FOPO apparatus. After a predetermined number of round trips have passed a post-processing source code is executed which loads the dataset from the previous simulation and, via the Matplotlib module, plots schematics used to analyse the behaviour of the system.

Unlike the FOPA models described in Chapters 3 - 4 a round trip simulation through the oscillator needs to be calculated over thousands or even tens of thousands of times until a convergent state is reached. While the models describing the phase modulators and the WDMCs are not resource intensive the pulse propagation through the fibre can be. Therefore, for the model to be computationally feasible, the pulse propagation method needs to be accelerated. To do this, initially, (5.2) is expanded, and the resulting factors are assembled in order to minimise the number of matrix arithmetics. This process was conducted using SymPy, and the resulting equation is shown in Appendix B.

Initial optimisation of the pulse propagation part of the SM-FOPO was conducted by optimising the nonlinear step of the SSFM (as described in Section 2.2). This acceleration was firstly attempted using the Numba module and afterwards by using Cython to translate the nonlinear integral part into optimised C code. However, on preliminary executions of the source code, the computational times were still significant, and therefore further optimisation was required. In the final version of the source code,

the entirety of the pulse propagation part of the oscillator was written in highly optimised Cython. The code makes use of optimised MKL C functions and also makes use of Cython Memoryviews to map the NumPy arrays to static sections of RAM and C arrays [41].

Finally, the ability to execute on multiple cores and core/nodes is inbuilt into the model by using the joblib and mpi4py modules respectively. The results shown in this thesis were exclusively simulated on IRIDIS 5 since a broad sweep of parameters could be applied and distributed over multiple nodes and cores minimising execution times significantly. The final version of the source code was made publicly available and is listed first in Appendix A.3.

5.3 Model Application

5.3.1 Optical System Parameters

As outlined in Section 5.1 the SM-FOPO simulated in this chapter consists of two phase modulators, a σ loss, two WDMCs and a HNLF. The HNLF chosen is the same as the one investigated in Chapter 4 with its parameters outlined in 4.2.1 whilst the other subsystems are defined here.

Within the scope of the BNLSE the central band ($l = 0$) is the frequency band that the pump is applied to. The pump wavelengths to be investigated are varied within the normal dispersion regime and are set close to the zero dispersion wavelength. By setting the pump wavelengths, the fibre parameters and a pump power of $5W$ to (4.25) the separation between the parametric sidebands Ω can be calculated. Following this, the central frequencies of each band can be determined from $\omega_l = \omega_p + l\Omega$ where $l = -3, -2, ..., 3$. The equivalent central wavelengths of these central frequencies are shown in Table 5.1 with frequency bands $l = -1, 1$ representing the signal and idler respectively. The equation used to calculate the separation between frequency bands uses the undepleted pump approximation and a pump power of 5 W and therefore the wavelength shown in Table 5.1 only serve as an estimation for the position of the bands central frequency/wavelength. In each case simulated the central frequencies/wavelengths are recalculated for the pump power simulated and an adequate spectral width is applied to each band in order to incorporate all the parametric waves.

Given the wavelengths of the signal, pump and idler shown in Table 5.1 the WDMCs are defined as WDMC1 (1048 nm, 1204 nm) and WDMC2 (928 nm, 1204 nm) such that the signal is oscillated and the idler forms the output of the system. The attenuation applied to the oscillating waves by the σ loss is also set to $\alpha = 1.4$ dB. It is worth mentioning that these parameters are similar to what was quoted in the experimental study of an equivalent SM-FOPO by Zlobina et al. [110]. With these definitions in place

TABLE 5.1: Central wavelength position of the seven frequency bands simulated in the SM-FOPO. The wavelengths are calculated by using the fibre parameters highlighted in the main text and a pump power of $5W$.

Central wavelength of band l (nm)						
-3	-2	-1	0	1	2	3
2017	1540.3	1245.9	1046	901.4	791.9	706.1
1861	1478	1225.7	1047	913.8	810.6	728.4
1714.8	1414.8	1204.1	1048	927.7	832.2	754.6
1574.8	1349.3	1180.4	1049	943.9	858	786.4
1435.3	1278.9	1153.2	1050	963.8	890.6	827.8

the transmittance and insertion windows of the SM-FOPO are calculated by using the theory outlined above and graphically depicted in Figure 5.4. The transmittance window represents the percentage of power that is oscillated within the cavity with respect to frequency/wavelength while the insertion window is the percentage of power that can be inputted into the oscillator via WDMC1. The transmittance and insertion percentage for the signal wavelengths shown previously is presented in Table 5.2. From the table it can be seen that the maximum oscillation of signal power occurs at $\lambda_{-1} = 1204.1\,\text{nm}$ while $\lambda_{-1} = 1153.2\,\text{nm}$ allows the highest percentage of signal power to be seeded into the oscillator.

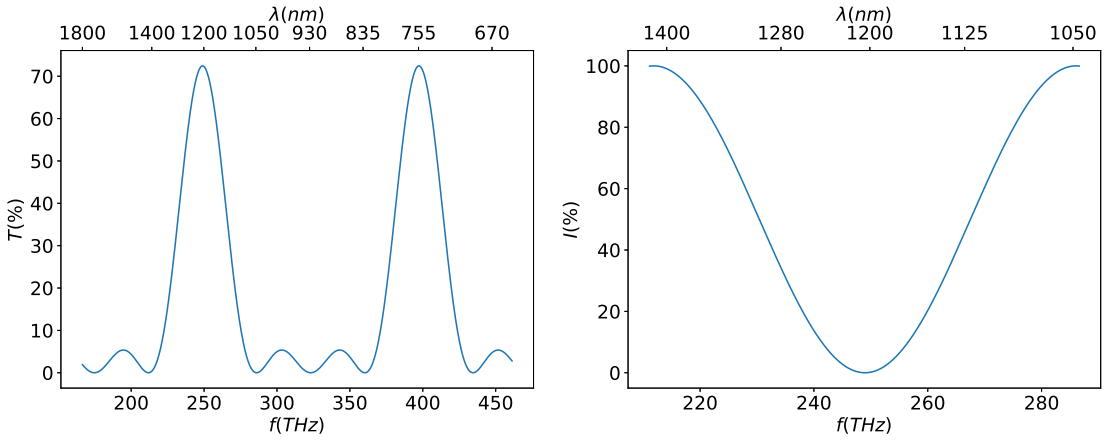

FIGURE 5.4: Transmittance (left) and insertion (right) window of the two WDMC SM-FOPO configuration.

TABLE 5.2: Transmittance and insertion of the signal within two WDMC SM-FOPO configuration. The wavelengths (and equivalent transmission and insertion percentages) are calculated by using the fibre parameters highlighted in the main text and a pump power of $5W$.

λ_0	λ_{-1}	T_{-1}	I_{-1}
1046	1245.9	61.8	12
1047	1225.7	69.4	3.4
1048	1204.1	72.45	0
1049	1180.4	68.45	4.45
1050	1153.2	54.75	20.2

The application of this numerical model to the SM-FOPO had the objective of investigating the output power and CE of the oscillator. To do this the output power is measured at every round trip by using (4.26). The initial increase of power is followed by it fluctuating around an average value which in this thesis is named the convergent state. The physical reasons behind this oscillation of power are described in the following sections however in order to represent the output power of the oscillator the average power of the last 50% of the oscillations is taken (after the system has visibly reached the convergent state). The CE is then defined as:

$$\mathrm{CE} = \frac{\langle P_{(\mathrm{idler})} \rangle}{P_{(a)}}, \tag{5.17}$$

where $\langle P_{(\mathrm{idler})} \rangle$ is the average idler power (of the last 50% of the oscillations) at position (d) of the oscillator and $P_{(a)}$ is the input power at position (a).

Finally, the fluctuation of power per round trip can be interpreted as noise. In this chapter this noise is measured by using the RIN which is defined as:

$$\mathrm{RIN} = 10 \log \left(\frac{1}{df} \frac{\sigma^2_{P_{(\mathrm{idler})}}}{\langle P_{(\mathrm{idler})} \rangle^2} \right), \tag{5.18}$$

where df is the frequency step size and $\sigma_{P_{(\mathrm{idler})}}$, $\langle P_{(\mathrm{idler})} \rangle$ are the standard deviation and mean of the output power over the last 50% of the oscillations respectively.

5.3.2 Validation and Convergence

5.3.2.1 Frequency Resolution

One of the models' parameters that can affect the accuracy of the numerical model of the SM-FOPO is the frequency step-size. This can be because sparse grids might neglect frequencies that may experience gain through FWM. To investigate the effect of frequency step size on CE and RIN of the oscillator a test simulation is executed. Within the investigation, a single CW pump is inputted into the oscillator (single pump configuration), and the output is calculated over a varying frequency step-size. The pump wavelength and power are set to 1046 nm and 6 W, 12 W respectively and the oscillator is simulated as described in the previous sections for 2000 rounds.

To illustrate that a dense frequency grid is required to accurately model the SM-FOPO the CE and RIN of the SM-FOPO are plotted with respect to these step-sizes df in Figure 5.5. For both pump powers, the output power is similar for the sparsest frequency grid, but the results deviate as df is decreased with the two configurations exhibiting vastly different powers for a dense grid. On the other hand, the trend of the RIN results are similar in both cases where lower noise are exhibited for large df and higher

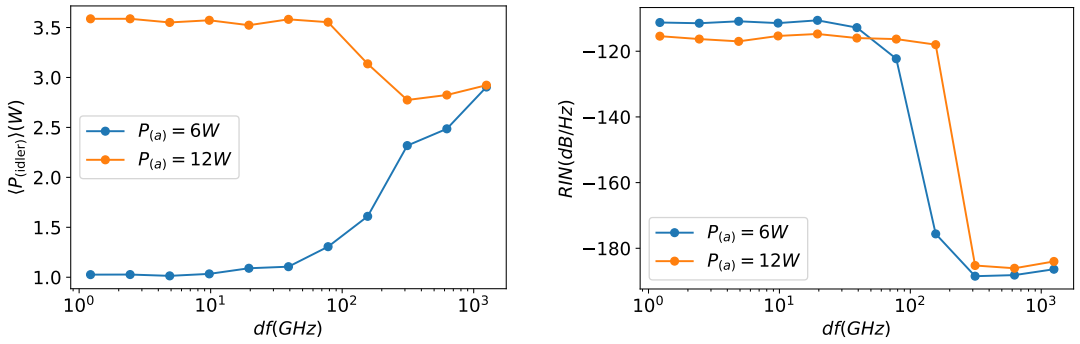

(a) (b)

FIGURE 5.5: SM-FOPO idler output power (a) and RIN (b) with respect to the frequency step-size df. The pump wavelength is 1046 nm and the signal, idler wavelengths can be found in Table 5.1 [11].

values when the grid becomes denser. For both these parameters, it can be seen that as the frequency grid points are increased the results converge and therefore, for all the following simulations in this chapter the frequency step size is set to 4.9 GHz.

As seen in Figure 5.5 the $\langle P_{\text{idler}} \rangle$ and RIN of the oscillator varies greatly with respect to the number of frequency points simulated in each band. To illustrate the reason behind these results the power per oscillation and spectra are shown in Figure 5.6(a) for a range of frequency step-sizes df and $P_{(a)} = 6\,\text{W}$. In all cases investigated the power per oscillation reaches a convergent state after a few hundred round trips. For the sparsest frequency grid ($df = 1.25\,\text{THz}$) the power initially increases and afterwards stabilises close to 3 W while for smaller df the power oscillates around a lower value. The reason behind this deviation can be explained by the spectra shown in Figure 5.6(b). For $df = 1.25\,\text{THz}$ there is only a single frequency point in the gain bandwidth dictated by phase matching and thus the output of the oscillator is a stable CW. As df is decreased and more frequencies are found in the gain bandwidth the power drops and the noise of the oscillator increases and a more realistic model to describe the SM-FOPO is achieved.

Finally, the investigation shown in this subsection indicates that a sparse frequency grid is not applicable in simulating the SM-FOPO. As a result of this, the coupled amplitude equation model usually used to simulate CW SM-FOPOs is not able to incorporate all the physical phenomena and can result in producing inaccurate results. Also, since the frequency grid spacing required is so small the use of SM-GNLSE instead of the BNLSE would be computationally unfeasible with the first requiring over 57000 points in the frequency grid against the later needing 7168 points (and a frequency-band width of 5 THz) to achieve the frequency step of $\leq 4.9\,\text{GHz}$.

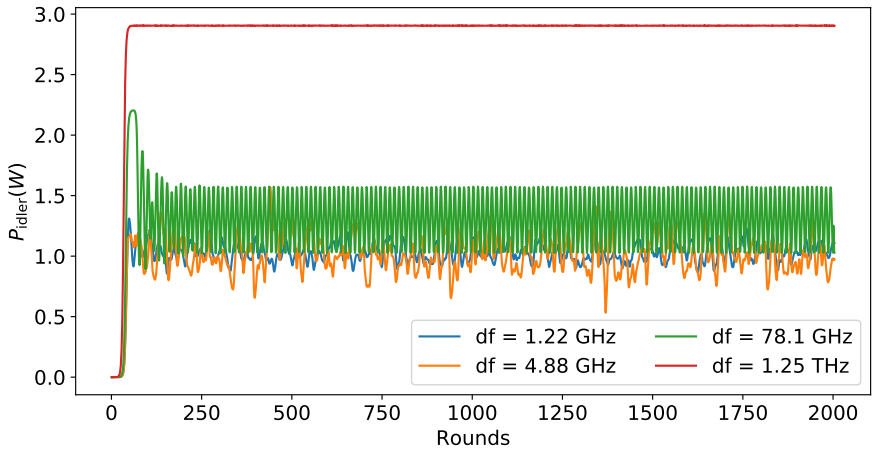

(a)

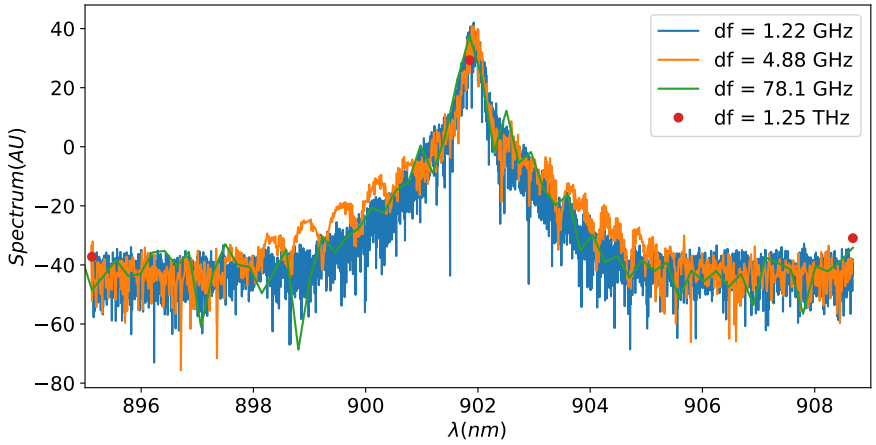

(b)

FIGURE 5.6: Idler output power per oscillation (a) and final idler spectrum at the last oscillation (b) for varying frequency step-sizes. The pump power and wavelength considered for these results is 6 W and 1046 nm respectively and the idler wavelength can be seen in Table 5.1 [11].

5.3.2.2 Four Wave Mixing Phase Modulator

In subsection 5.2.3 it was mathematically shown that the conversion efficiency of a SM-FOPO depends upon the phases of the waves involved. To make sure that the oscillator operates on or close to threshold the phase of the signal is modulated in PM_1. This modulation, however, changes each round trip according to (5.12). To illustrate how this modulation varies for every oscillation the SM-FOPO model is executed for 2000 round trips, a pump wavelength of $\lambda_p = 1046\,\text{nm}$ and a pump power of $P_p = 5\,\text{W}$.

At each oscillation the complex argument of the amplitude in the signals' frequency band is modulated, the amount of which is graphically represented for each frequency in Figure 5.7(a). As can be seen, a distinct pattern is visible for the frequencies in the centre of the frequency band, or in other words where the gain is high and (5.12) is

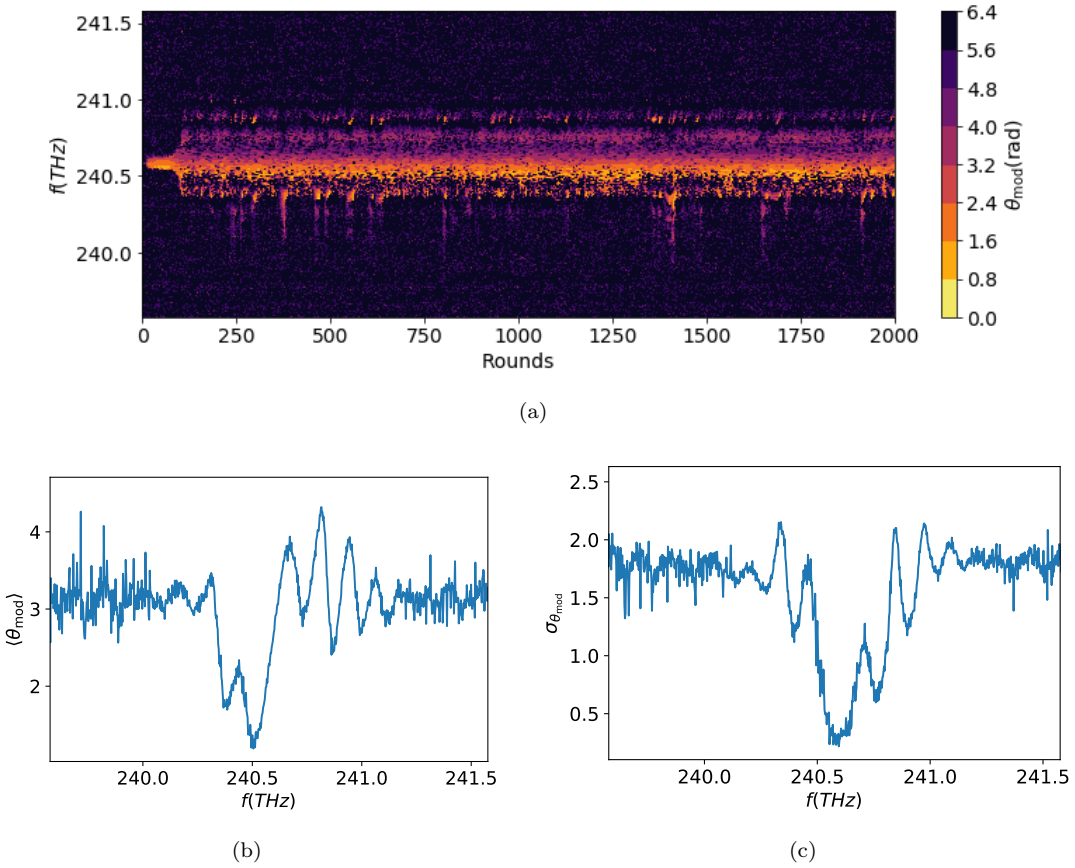

FIGURE 5.7: Modulating complex argument θ_{mod} applied to the signal frequency band upon PM_1. In (a) θ_{mod} is varied with respect to frequency and round trips and, in (b), (c) the mean and standard deviation from that mean over the last 1000 oscillations with respect to frequency. The parameters of the simulation can be found in the text.

applicable. The mean complex argument modulation $\langle\theta_{\text{mod}}\rangle$ and the standard deviation from that mean are shown in Figure 5.7(b) and Figure 5.7(c) respectively. The minimum standard deviation is found to be 0.22 rad at ≈ 1246 nm which coincides with the centre of the signal band (and predicted highest gain wavelength) depicted in Table 5.1.

In a second simulation the phase modulation applied by PM_1 is set to be constant at every oscillation and equal to $\langle\theta_{\text{mod}}\rangle$ shown in Figure 5.7(b). The power of the idler per oscillation is shown in Figure 5.8 along with the power per oscillation with the automatic phase modulation described previously. As can be seen, while initially the powers grow at different rates both results converge to a similar power after a few hundred oscillations.

The automatic phase modulation described in subsection 5.2.3 and exhibited here is a technique to estimate the oscillator's resonance (with respect to the maximum conversion of energy from the pump to the sidebands). Another way to search for the phase modulation that would bring the SM-FOPO to resonance is for each set of parameters to simulate the oscillator for multiple constant phase modulations in order to search for the maximum power conversion to the sidebands. It would be equivalent to varying the oscillator cavity length in a practical application of the SM-FOPO to search for

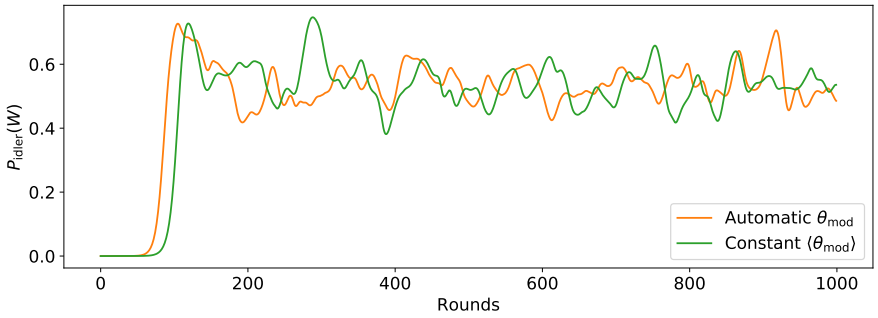

FIGURE 5.8: Idler power per oscillation when the signal phase is modulated automatically and when is modulated by a constant vector. The parameters of the simulation can be found in the text.

resonance. However, such an investigation would be computationally unfeasible since the oscillator model would have to be executed for multiple phase modulations and over thousands of oscillations each time. Such an inquiry would also have to be repeated for each set of parameters. *Ergo* the automatic phase modulation used in PM_1 is the most feasible estimation to simulate the SM-FOPO on or close to resonance.

5.3.2.3 Wavelength Division Multiplexing Coupler Phase modulator

As discussed in subsection 5.2.4 if a pump and a seed are inputted into the oscillator (seeded SM-FOPO configuration) then the oscillating signal may destructively interfere with the inputted seed. To make sure these two waves constructively interfere, and therefore maximise the CE of the SM-FOPO, the oscillating seed is modulated within PM_2 (as shown in Figure 5.1). To investigate how the modulation varies at every round trip the oscillator model was simulated for 2000 round trips, $\lambda_p = 1046\,\text{nm}$, $P_p = 3W$ and $P_s = 100mW$ applied at $\lambda_s = 1246\,\text{nm}$. For these configurations, if the oscillator were not seeded, there would be no idler output power. Or in other words, the oscillator is operating below threshold (with respect to an equivalent unseeded configuration).

In the seeded SM-FOPO configuration the seed is a CW so only a single point in the signal frequency band is required to calculated θ_m from (5.16). The modulating complex argument θ_m that is added to the signal at every round trip is shown in Figure 5.9(a) with respect to the number of oscillations. As can be seen θ_m converges to a constant value of $4.473\,\text{rad}$ within the first 100 round trips. In a subsequent simulation, the signal is modulated at every oscillation by the convergent θ_m value found previously. Figure 5.9(b) depicts the idler power per oscillation for the automatic and constant modulation at PM_2. Initially, the power increases faster for the automatic case, but both simulations converge to the same output power.

As is shown in the following subsection the seeded oscillator is also applied to above threshold configurations. Therefore the validity of the applying PM_2 at these regimes was investigated. The simulation described above was repeated with the automatic

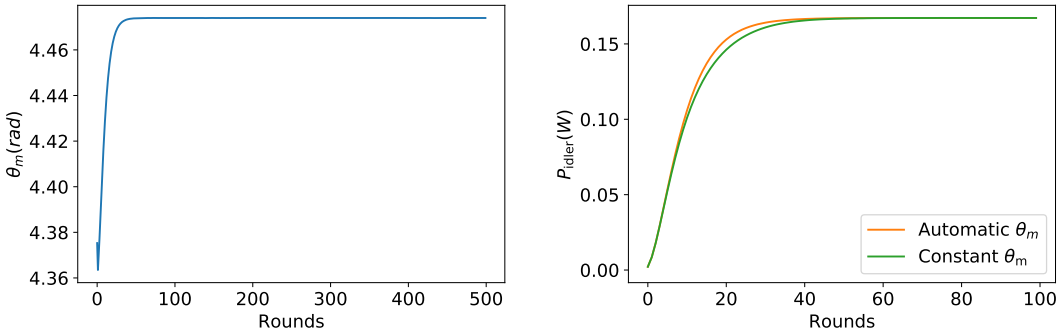

(a) (b)

FIGURE 5.9: Modulating complex argument θ_m variation applied to the signal frequency upon PM_2 (a) and idler output power per oscillation with automatic and constant θ_m (b). The SM-FOPO is operating under the threshold and the parameters of the simulation can be found in the text.

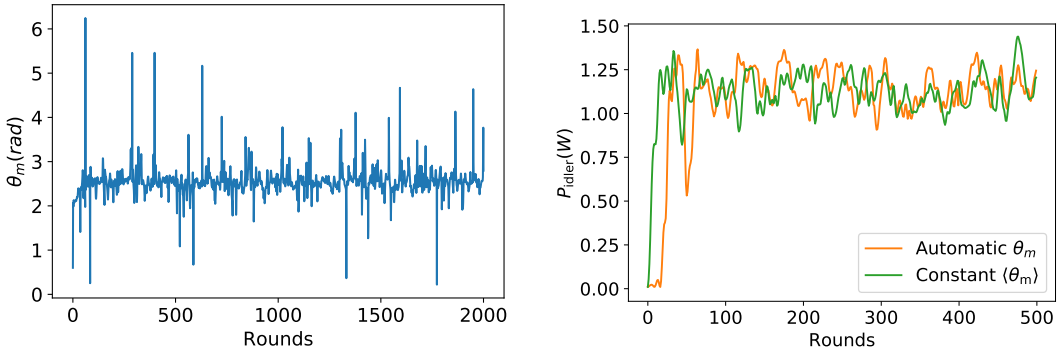

(a) (b)

FIGURE 5.10: Modulating complex argument θ_m variation applied to the signal frequency upon PM_2 (a) and idler output power per oscillation with automatic and constant $\langle\theta_m\rangle$ (b). The SM-FOPO is operating under the threshold and the parameters of the simulation can be found in the text.

phase modulator in PM_2 but with a pump power of $P_p = 5\,\mathrm{W}$. The automatic phase modulation applied within PM_2 is shown in Figure 5.10(a). The average phase modulation of the last 1000 oscillations is $\langle\theta_m\rangle = 2.56\,\mathrm{rad}$ and the standard deviation is $\sigma_{\theta_m} = 0.27\,\mathrm{rad}$. This average is then used to modulate the oscillating signal at every round trip within a subsequent simulation as was conducted in the below threshold case. The idler power per oscillation is then compared to that of the automatic phase modulation in Figure 5.10(b). The power increases faster in the case of the constant phase modulation, but after about 100 round trips both powers reach the same convergent state.

The automatic phase modulation applied within PM_2 forces constructive interference of the seed and oscillating signal within WDMC1. Within both the above configurations it was shown that this modulation could be considered as an equivalent of modulating the oscillating signal by a constant amount. As was discussed previously this could be

achieved experimentally by manually varying the length of the oscillator cavity until maximum CE is observed.

5.3.2.4 Comparison With Experimental Results

As previously mentioned, the oscillator apparatus used in this study is similar to the one experimentally studied by Zlobina et al. in [110]. Also, parameters such as the fibre dispersion parameters were used in the simulations of this chapter. Therefore it is of interest to compare the results from the experimental study with those shown in this chapter.

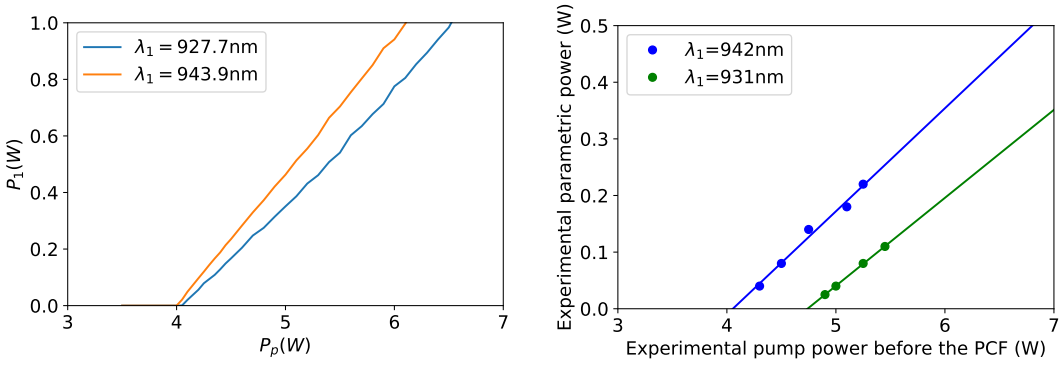

(a) (b)

FIGURE 5.11: Output power of the FOPO studied in this chapter (a) and the one studied by Zlobina et al. in [110] (b). In both figures, the idler wavelength is shown in the legend, and the data shown in (b) has been estimated from Fig 4 in [110].

Figure 5.11(a) depicts the output power (with respect to the pump power) of the FOPO studied in this chapter for two idler wavelengths shown in the legend. In Figure 5.11(b) equivalent experimental data gathered from [110] are shown for similar output wavelengths. Contrary to Figure 5.11(a), the experimental data shown in Figure 5.11(b) is plotted with respect to the pump power before the PCF. Furthermore, the input pump of the simulated study is represented by a Dirac delta function while the CW pump of the experimental study has a linewidth applied to it. Finally, when comparing the two figures, it should be taken into account that the simulated study assumed that the polarisation of the beam does not change throughout the system. This, however, is an approximation and is an effect that can limit the CE of the FOPO [81]. Even with all of these differences between the two studies, similar behaviour can be seen for the idler power in both studies. For example the thresholds from both studies can both be estimated to be between 3.5 W-4.5 W and after the thresholds have been reached the idler power increases linearly with respect to that of the pump.

5.3.3 Conversion Efficiency and Relative Intensity Noise of the Oscillator

5.3.3.1 Unseeded Input

Initial simulations of the oscillator were conducted only for a CW pump input (unseeded SM-FOPO configuration). The stable parameters used such as the WDMCs configuration and fibre parameters have been established in the previous sections. For this configuration, the oscillator is simulated for the pump wavelengths shown in Table 5.1 for various pump powers. As stated earlier, for each of the parameters considered the oscillator is simulated over multiple round trips until a convergent state is reached. Whether the system has reached such a state needs to be evaluated graphically for each numerical simulation. One could potentially define a metric that would automatically detect the convergent state of the oscillator. However, initial investigations found that the behaviour of the parametric power varied greatly for each of the simulations considered. Therefore no single metric could be found that would satisfy all cases and the graphical approach was deemed the optical way to classify whether the convergent state has been reached. At this state the CE and RIN are calculated by using (5.17) and (5.18) respectively. The average idler power in each case is calculated as the average of the last 50% of the oscillations (after the convergent state is reached).

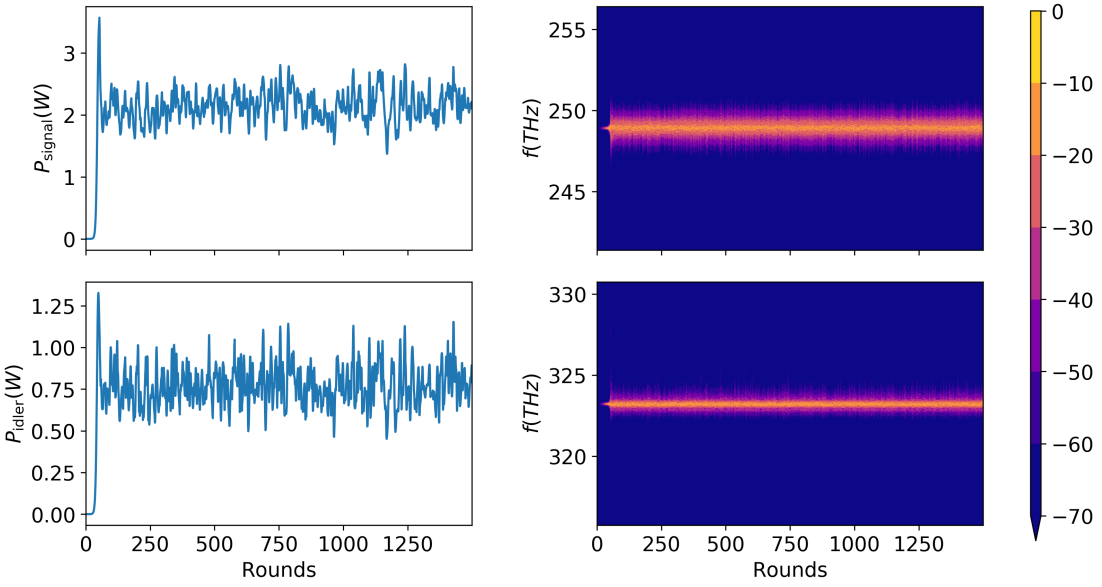

FIGURE 5.12: Power per oscillation (left) and equivalent spectra (right) of the signal at point (b) of the oscillator (top) and and idler at point (d) of the oscillator (bottom). The pump power considered is 6 W, the rest of the parameters are given in the text and the spectra are shown in units of *dB* normalised to the output pump power.

The signal is recycled within the oscillator such that its power is built up within the fibre cavity. As stated earlier a high signal power within the SM-FOPO is favourable for energy conversion to the idler. This can be seen in Figure 5.12 where the oscillator is

simulated for $\lambda_p = 1048\,\text{nm}$ and $P_p = 6\,\text{W}$. As the number of oscillations increases the signal power increases within the fibre cavity and reaches a convergent state of $\approx 2\,\text{W}$. The high signal power then increases the energy conversion from the pump to the idler. This, in turn, results in a higher output power of the oscillator which in this case reaches a convergent state at $\approx 0.75\,\text{W}$. The spectra of the signal and idler are shown in units of dB normalised to the output pump power.

As can be expected the number of oscillations required for the signal and idler to reach their convergent state varies for different input pump powers. At lower input powers the gain of the oscillating signal is less and therefore more oscillations are required. On the other hand, the signal power increases rapidly for high input pump powers, and therefore fewer round trips are needed to reach the convergent state. To illustrate this, selected idler powers and spectra per oscillations are shown here. Figure 5.13 depicts the idler output power of the oscillator (and equivalent idler spectra) with respect to the number of oscillations. These results where simulated for a pump wavelength of $\lambda_p = 1048\,\text{nm}$ and the pump powers are $P_p = 4.2\,\text{W}, 7\,\text{W}$ and $11\,\text{W}$. As previously the spectra are shown in units of dB and normalised to the output pump power. As expected the number of oscillations required in each simulation is higher for lower powers with 6000 round trips required in the case of $P_p = 4.2\,\text{W}$ whereas only 500 round trips are needed for $P_p = 11\,\text{W}$. Additionally, as is expected the idler output power increases with respect to the pump powers, furthermore the bandwidth of the idler broadens for higher powers. This can be attributed to the FWM gain bandwidth broadening with higher pump powers.

To investigate the behaviour of the CE with respect to pump power and wavelength the oscillator is simulated as described above for multiple pump wavelengths and powers. The pump wavelengths considered are shown in Table 5.1 and the pump power is varied from $3.5\,\text{W}$ to $12\,\text{W}$. The SM-FOPO CE for these parameters are shown in Figure 5.14(a). For pump powers under $3.9\,\text{W}$ the oscillator is under threshold for all the pump powers considered. Between $3.9\,\text{W}$ and $4.1\,\text{W}$ threshold is achieved for the pump wavelengths of $\lambda_p = 1046\,\text{nm}, 1047\,\text{nm}, 1048\,\text{nm}$ and $1049\,\text{nm}$ while threshold for $\lambda_p = 1050\,\text{nm}$ is achieved at approximately $4.65\,\text{W}$. The thresholds are partially subject to the transmittance of the signal within the oscillator shown in Table 5.2 where the signal of $\lambda_s = 1153.2\,\text{nm}$ (signal for $\lambda_p = 1050\,\text{nm}$) has the lowest transmittance of signals considered. It is worth mentioning that the threshold for $\lambda_p = 1048\,\text{nm}$ calculated here ($4.05\,\text{W}$) is in excellent agreement with the experimental threshold of $4.1\,\text{W}$ reported by [110]. If the threshold of this simulation was to be estimated by the theory described in [10] which is based on the CW approximation then the threshold would have been expected at the lower value of $3.3\,\text{W}$ [11, 91, 110]. This shows the increased accuracy that the numerical model described in this chapter provides when compared to previous models. Finally, for all the pump wavelengths considered, as the pump power is increased the CE is increased reaching $\approx 30\%$ for the high powers considered.

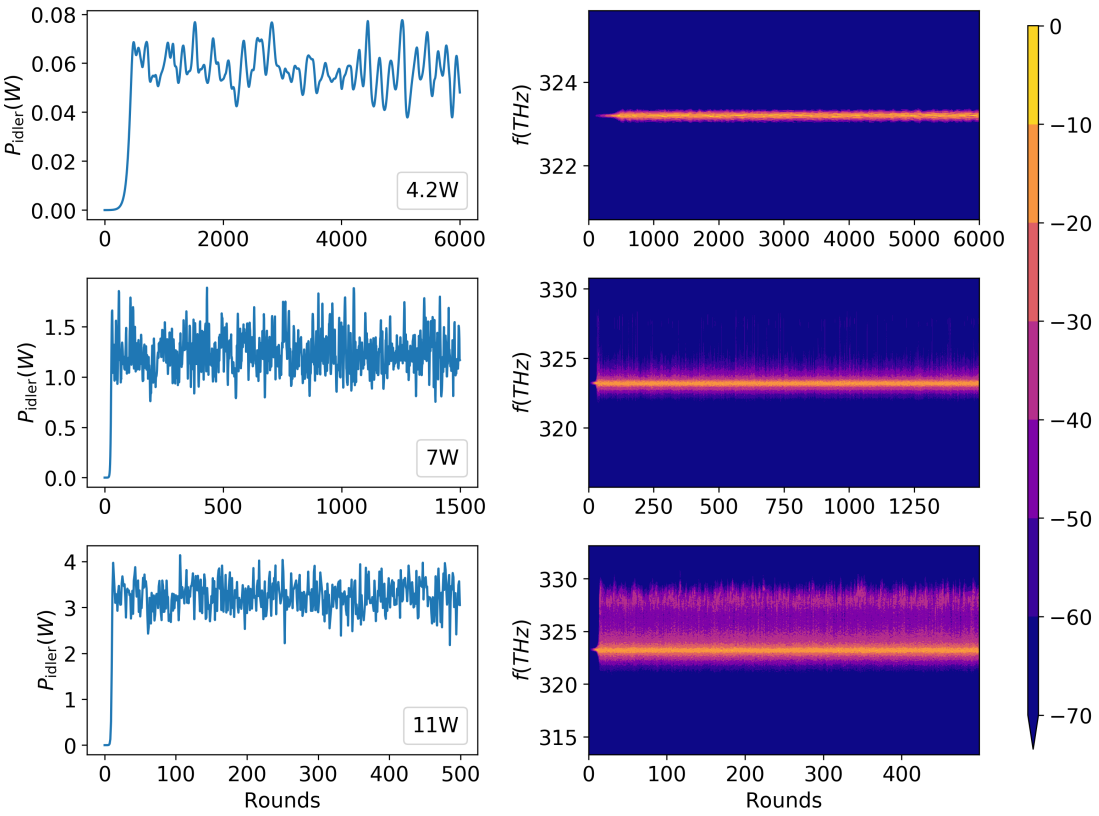

FIGURE 5.13: Power per oscillation (left) and equivalent spectra (right) of the oscillators output idler for different input powers. The pump wavelength considered is $\lambda_p = 1048\,\text{nm}$ (and equivalent signal and idler wavelengths are shown in Table 5.1), the pump powers are shown in the inset of the figures and the spectra are measured in units of dB normalised to the output pump power.

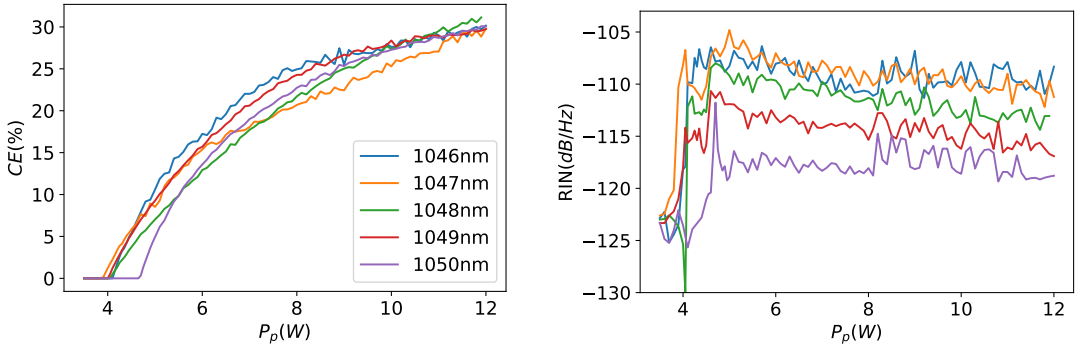

(a) (b)

FIGURE 5.14: Oscillator CE (left) and RIN (right) with respect to the input pump power. The oscillator is pumped only by a CW pump (unseeded configuration). The pump wavelengths are given in the inset of (a) and the equivalent signal/idler wavelengths can be found in Table 5.1.

Figure 5.14(b) depicts the output idler's RIN with respect to the pump power. Below the threshold powers, the RIN is subject to the noise floor applied to the system at $\approx -127\,\text{dB/Hz}$. This RIN is close to what has been measured for an Yb3+-doped fibre

laser (−130 dB/Hz) [111]. As the output power increases, however, the RIN is increased for all the idlers considered. As stated earlier one of the reasons behind the increase of the RIN is the presence of the cascade FWM processes [102]. Besides, while the input pump is CW the parametric signal and idler contain multiple frequencies which are competing for parametric gain, the interference of the frequencies within these gain bandwidth results in an increased RIN of the oscillator. Furthermore, because of the dependence of the idler on the other parametric waves any instability or noise exhibited will be mirrored in the idler, for example, random variations of the signal at every round trip will affect the RIN of the idler [11, 98].

For powers larger than threshold all the pump wavelengths considered show different RIN values with the pump power of $\lambda_p = 1050\,\text{nm}$ exhibiting the lowest values at $\approx -117\,\text{dB/Hz}$. The RIN decreases as the pump approaches the ZDW (which for the fibre considered is $\lambda_z = 1051.85\,\text{nm}$). In degenerate FWM the gain bandwidth of the parametric sidebands increases when the difference between the ZDW and the pump wavelength decreases [9, 10]. Therefore one could postulate that there is a correlation between the decreasing RIN and the sideband's gain bandwidth.

5.3.3.2 Seeded Configuration

In an attempt to decrease the RIN of the output idler a seeded SM-FOPO configuration is considered. In such a scenario a seed, placed at the centre of the frequency band $l = -1$, is inputted into the oscillator along with the pump at every round trip. Like in the previous subsection the pump wavelengths simulated are shown for band $l = 0$ in Table 5.1 and the oscillator is simulated as described above. The seed insertion percentages, *i.e.* the percentage of seed inserted into the oscillator at every round trip, are shown in Table 5.2. As can be seen, there is no seed added to the oscillator for the configuration of $\lambda_p = 1048\,\text{nm}$ and therefore this pump wavelength will not be considered here. For the other pump wavelengths the pump power is varied from $P_p = 0.5\,\text{W}$ until $P_p = 12\,\text{W}$ while the seed signal is kept constant at $P_s = 100\,\text{mW}$. Finally, it is worth mentioning that in this seeded configuration both phase modulators shown in Figure 5.1 are operating.

Figure 5.15 depicts the power and spectra per oscillation for a pump wavelength of $\lambda_p = 1046\,\text{nm}$. The three input powers considered are chosen to be below ($P_p = 2\,\text{W}$), close ($P_p = 4.25\,\text{W}$) and above ($P_p = 8\,\text{W}$) the unseeded threshold power. As previously the idler power and spectra are measured at point (d) of the oscillator as shown in Figure 5.1. Far below the threshold power the signal is CW and therefore FWM between it and the CW pump results in a CW output idler. A result from these pump power regimes ($P_p = 2\,\text{W}$) can be seen in the top figures of Figure 5.15 where the idler converges fast to above 40 mW and the spectrum shows a CW output. Close to the unseeded threshold however ($P_p = 4.25\,\text{W}$) power instabilities (with respect to the round trips)

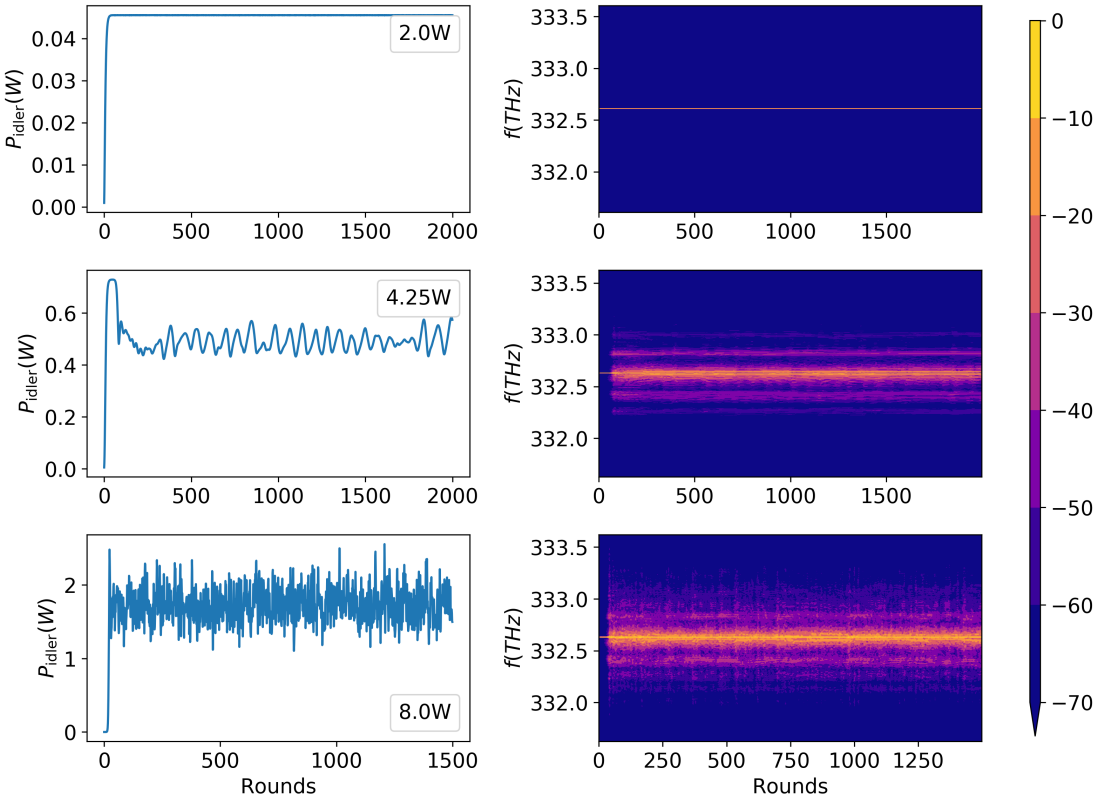

FIGURE 5.15: Power per oscillation (left) and equivalent spectra (right) of the seeded configuration oscillators output for different input powers. The pump wavelength considered is $\lambda_p = 1046\,\text{nm}$ (and the equivalent signal and idler wavelengths can be seen in Table 5.1), the pump powers are shown in the inset of the figures and the spectra are measured in units of dB normalised to the output pump power.

equivalent to those observed in the unseeded configuration start occurring. In this case the idler reaches a convergent state at $\approx 0.5\,\text{W}$ and the spectrum shows a distinct bandwidth. At even higher powers ($P_p = 8\,\text{W}$) the idlers gain bandwidth and power instability is equivalent to what was observed in the unseeded configuration indicating that the seed does not perturb the result in these power regimes.

The CE and RIN for the pump powers considered in the seeded oscillator configuration are shown in Figure 5.16. In Figures 5.16(a), 5.16(b) the CE and RIN is shown for all the pump powers considered while Figures 5.16(c), 5.16(d) are magnified to the lower part of the pump power sweep. Below the unseeded threshold powers, the CE steadily increases with increasing pump power for all pump wavelengths considered and the RIN decreases. The behaviour of the RIN in these regimes can be explained by looking at the top figures of Figure 5.15 where the output power is stable at every oscillation after the convergent state is reached. In these regimes, the mean idler power (with respect to the last 50% of the oscillations) increases with pump power while the standard deviation from that mean remains relatively constant. Therefore according to (5.18) the RIN decreases. For pump powers between 3 W and 5 W the CE of all the pump wavelengths studied experiences a saturation after the initial increase of power. Within this power regime, the RIN

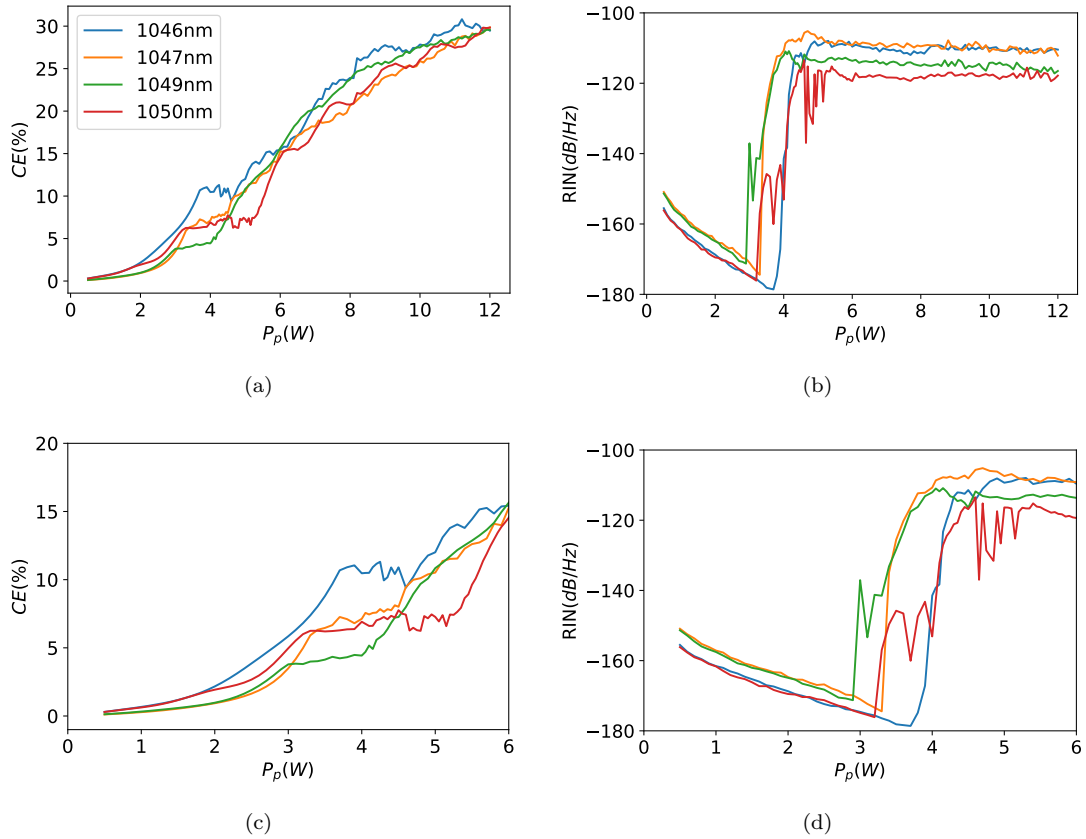

FIGURE 5.16: Oscillator conversion efficiency (left) and relative intensity noise (right) with respect to the input pump power. Top figures show all the pump powers investigated and the bottom ones are magnified to the lower part of the pump power sweep. The oscillator is pumped by CW pump and seed (seeded configuration). The pump wavelengths are given in the inset of (a) and the equivalent signal/idler wavelengths can be found in Table 5.1.

increases rapidly to levels comparable to the unseeded SM-FOPO configuration. After the input pump power surpasses the unseeded thresholds shown in Figure 5.14 then the RIN and CE results become similar to those of the unseeded SM-FOPO configuration.

Contrary to the unseeded SM-FOPO configuration a signal is required for the seeded SM-FOPO to operate. This means that such a system calls for light to be available at the seed's wavelength. These are the same requirements as FOPA have. Though, as stated earlier parametric conversion from the pump to the idler is increased when the signal power is higher. As the signal oscillates within the fibre cavity its power its increased, which in turn increases the CE of the oscillator. Within Figure 5.16, at the under threshold configurations, the CE of the oscillator is under 5 %. Such efficiencies can easily be reached by conventional FOPAs [10]. However, these FOPA systems are inherently composed of HNLFs that has been tailored such that to achieve high CE. Further research into seeded and unseeded SM-FOPOs should simulate various fibres to increase the CE of the system.

Because of the similarity of the results between the unseeded and the seeded SM-FOPO configurations one could postulate that the application of the seed is redundant to SM-FOPOs. However, as was seen in Figure 5.16(d) at the lowest powers investigated the SM-FOPO experiences low RIN. Therefore such a configuration could be used in applications where low noise output is paramount (such as applications in the medical industry).

5.4 Conclusion

In this chapter, the model and results of a SM-FOPO were presented. Each of sub-modules that encompass the SM-FOPO were discussed and it was shown how the oscillator was set up to oscillate a selected part of the bandwidth and output another. The numerical models that are used to describe each of these sub-modules were detailed, and it was shown how their accumulation creates the SM-FOPO numerical model. This numerical method is then applied to a configuration similar to what was experimentally demonstrated in [110]. After initially investigating the validity of each sub-modules numerical method, the CE and RIN of multiple parameters sweeps where investigated. The thresholds calculated were in agreement with those shown in [110].On the other hand the noise of the FOPO was not something investigated in [110]; however, it was found that the RIN was high for many of the parameters sweeps considered in this chapter. The main reason behind this increase in noise was attributed to the gain bandwidth of the parametric signals and idlers. In an attempt to limit the noise a seeded SM-FOPO configuration was considered where low RIN figures were observed for low pump powers, but no change was seen for above threshold powers.

Throughout this chapter, the pump has been considered CW and is numerically described as a Dirac-delta function upon spectra in the frequency domain. Such an application however is an approximation since when CWs are applied to SM-FOPO a pump with suitable linewidth is applied so as to avoid stimulated Brillouin Brillouin scattering [11, 92]. A continuation of this study could add a linewidth to the pump and investigate how this would affect the CE and RIN of the oscillator.

A distinct enhancement that the model described in this chapter provides when compared to other numerical studies of oscillators is the application of the BNLSE for the pulse propagation. The first improvement is with respect to the accuracy of the equation (when compared to other CNLSE) as described in Chapter 4. Secondly, as it was shown in Section 5.3.2, the increased resolution of the frequency bands that the equation provides allows the simulation of accurate and convergent results. Equivalent models where the pulse propagation is simulated by using the coupled amplitude equations [9, 10] would not be able to recreate these results [11]. Finally, the application of the BNLSE

significantly decreases the execution time of the SM-FOPO model for the same frequency resolution when compared to applying the SM-GNLSE for the same frequency step.

Because the oscillator model is solved by simulating each sub-module sequentially for thousands of round trips the computational efficiency of their mathematical models is essential. From all the sub-modules in the SM-FOPO solving of the BNLSE takes most of the execution time. Therefore a considerable effort was applied to accelerate the numerical method that solves it. The compilation of the pulse propagation equation was conducted using Cython and MKL libraries within the Python framework. Also, all the results presented in this chapter were simulated using IRIDIS 5. It is worth mentioning that without both the code acceleration and the HPC application it would not have been possible to simulate the results shown in this chapter within the time confines of this research.

The CE for the unseeded SM-FOPO configuration behaves similarly for all the pump wavelengths considered. The CE increases from zero after the threshold power is reached. The position of this threshold power depends upon the signal transmittance within the fibre cavity. For input powers above the threshold power the oscillator experiences high conversion efficiency with the maximum obtained at $\approx 30\%$. However, it was also shown that a high RIN accompanies this high CE. The simulation of the seeded SM-FOPO configuration showed that below the unseeded threshold power the RIN was low. From these findings, one could postulate that the unseeded SM-FOPO can be used in applications where high power conversion is required and high RIN is not a hindrance. On the other hand, the seeded SM-FOPO could be used in systems that require lower output power and low RIN. It is worth mentioning however that the application of the seed requires the presence of light at the signal wavelengths. This is not a requirement for the unseeded configuration.

As discussed earlier unseeded SM-FOPOs can provide wavelength conversion over a theoretically infinite bandwidth. Their operating wavelengths are only limited by the dispersion of the fibre and the transmittance of the material. Within this chapter CEs of up to 30 % were shown for converting light over 100 nm. However, high RIN was also exhibited. The unseeded SM-FOPO presented in this chapter could be used as a wavelength converter in industries where high RIN is not a hindrance such as manufacturing. To widen the applicability of SM-FOPOs to industries where high RIN is a hindrance (such as the medical industry) the RIN of these systems needs to decreased. Further research is required in designing, simulating and testing unseeded SM-FOPO systems with the aim in decreasing the RIN to noise levels similar to those exhibited by conventional laser sources (such as the Yb3+ doped fibre laser).

Finally, as stated above the recirculation of the idler within the fibre cavity can result in reductions of the CE due to energy being back converted into the pump. To make sure this does not occur the phase of the oscillating signal is modulated at every round

trip. While this approximation yielded high CEs, it can be considered a hindrance in the application of such systems. It is therefore preferable that care is taken for the entirety of the idler to be exported at every round trip [106]. Such an approach is taken in the next chapter with the application of the MM-FOPO.

Chapter 6

Multi-Mode Fibre Optical Parametric Oscillator

In the previous chapter, the operation of a SM-FOPO was investigated for two scenarios. In the first, the oscillator was pumped by a single wave and in the second a signal also seeds it. High CEs were shown in both cases by using a relatively short and highly nonlinear fibre. It was also shown that the RIN was very low for the seeded configuration. In addition, Chapter 3 foresaw the conversion of energy between modes using IM-FWM within a TMF. As was discussed in Section 3.4 recent investigations on IM-FWM have concluded that non-uniformities along the fibre length can result in reductions of the CE of the MM-FOPA. As previously mentioned, a way that this could be addressed would be to make use of shorter length fibres with a higher nonlinear coefficient (or larger overlap areas between the modes) or with the application of higher pump powers. Additionally, one could consider a MM-FOPO where the oscillation of a certain part of the spectrum would allow for parametric conversion in shorter length fibres, therefore limiting the adverse effect the fibre non-uniformities have upon the CE.

As was discussed in the previous chapter, SM-FOPOs have attracted some attention and have been experimentally and numerically investigated in various studies. This, however, is not the case for MM-FOPOs where, to the best of the authors knowledge, there is no study numerical or otherwise that uses MM-FOPOs to convert energy between modes. Fibres that support multiple modes have recently been considered in FOPO systems like the three-hole chalcogenide fibre used in [105]. However, the purpose was to convert energy between wavelengths, equivalent to the work conducted in the previous chapter. Within their numerical model, they ignore IM-FWM and only investigate FWM on the fundamental mode. They support this approach by arguing that the overlap integrals between the modes are much smaller than the inverse effective area of the fundamental mode. While this argument is valid the work does not highlight the potential CE that could be achieved for IM-FWM. In Chapter 3 for example it was shown that FWM

in multi-mode fibres can be used to convert energy between modes and wavelengths efficiently. It is therefore worth investigating the CE of IM-FWM that could be achieved by using a MM-FOPO.

In this chapter a MM-FOPO apparatus able to convert energy from the LP_{01} to the LP_{11} modes is presented. Furthermore, the numerical model capable of simulating such an oscillator is detailed and computational acceleration techniques used in it are discussed. Following this, the oscillator is simulated to investigate the noise and CE of the oscillator, and to highlight how the later can be increased. Finally, the length of the fibre used is varied, and it is shown that MM-FOPOs can be used for high-efficiency mode and wavelength conversion over a larger bandwidth than an equivalent MM-FOPA.

6.1 Multi-mode Fibre Oscillator System

6.1.1 Optical Apparatus

The intent of the MM-FOPO investigated in this chapter is to convert energy from a signal in the LP_{01} to an idler in the LP_{11} mode. This is equivalent to what was accomplished with the MM-FOPA described in Chapter 3. The configuration of the oscillator is shown in Figure 6.1. The system comprises of two Multi-Mode Demultiplexers (MMDUX), a Beam Splitter (BMS), a σ loss, a PM, a TMF and a Multi-Mode Multiplexer (MMUX).

The MM-FOPO is set up to oscillate a LP_{01} signal in the fibre cavity and export all energy that is in the LP_{11} mode at every round trip. Within the oscillator, each of the subsystems are placed to accomplish this. In particular, the MMDUXs serve to split the fibre modes into separate paths while the MMUX is set to combine them so they can propagate together in the TMF. The BMS separates different parts of the spectrum, equivalently to what is accomplished with the WDMCs in Chapter 5. The σ loss serves the same purpose as in the SM-FOPO configuration, that is, to introduce a global wavelength-independent loss to the oscillating signal. Finally, the PM operates equivalently as PM_2 did in SM-FOPO that is to adjust the phase of the oscillating signal so it constructively interferes with the signal of the next oscillation.

The oscillator that is shown in Figure 6.1 is pumped through position (a) with two pumps and a signal situated at separate wavelengths. The first pump (P_1) and the signal (S) are in the LP_{01} mode while the second pump (P_2) is in the LP_{11} mode. This input spectrum is identical to what was pumped in the MM-FOPA in Chapter 3 and is graphically shown in Figure 3.1(a). The spectrum initially passes through MMDUX1 where the modes are split and take separate paths. Light in the LP_{01} mode is inserted into the BMS through port (i), where the entirety of the LP_{01} pump and a percentage of the signal power is outputted through port (iii) and inserted into the oscillator cavity. The residual LP_{01}

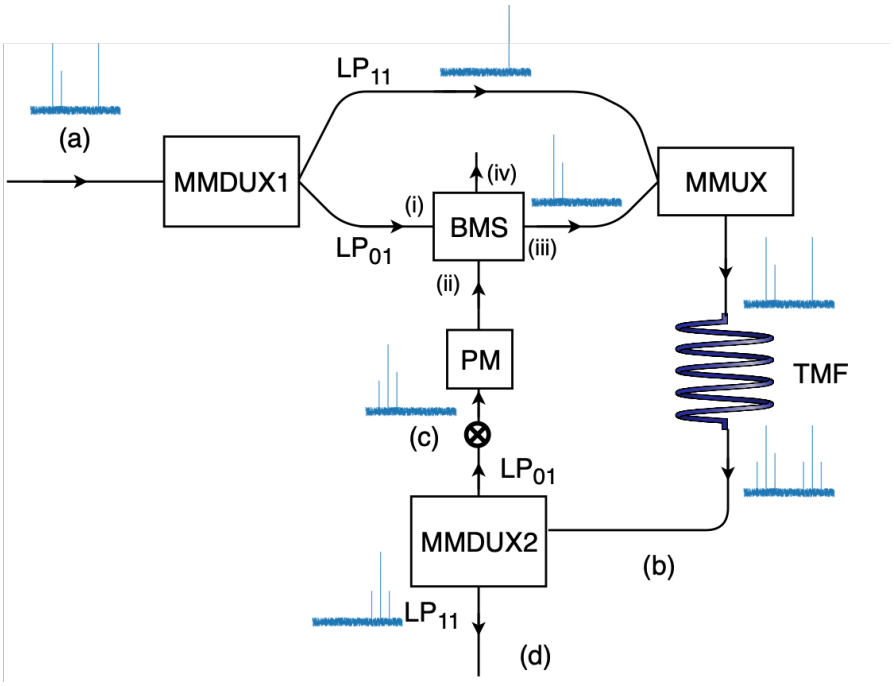

FIGURE 6.1: Optical system of the multi mode fibre optical parametric oscillator [109].

power is outputted from the optical system through port (iv) of the BMS. Following this, the two modes are combined in MMUX prior to them being propagated through the TMF. During the propagation through the fibre the LP_{01} idler I and the LP_{11} idlers BS and PC are amplified through FWM. The spectrum at position (b) of the oscillator is equivalent to what is shown in Figure 3.1(b). Afterwards, the modes are split again in MMDUX2 with the LP_{11} forming the desired output of the FOPO. On the other hand, the LP_{01} mode is passed through a σ loss at (c) which applies a constant loss to the spectrum. Then it is passed through the PM which modulates the phase of the spectrum such that it constructively interferes with the signal of the next oscillation. The spectrum is finally inserted into BMS where it is combined with the input to the fibre cavity, and the next oscillation commences. As was seen in Chapter 5 these oscillations continue until the oscillating signal (and by extension the output idlers) reaches a convergent state.

6.1.2 Insertion and Transmittance of the Oscillator

As can be seen in the previous subsection the FOPO is set up to oscillate the LP_{01} signal while the rest of the waves are expelled from the system at every oscillation. The motivation behind structuring the FOPO to operate in such a way is that, as was described in Chapter 5, oscillation of multiple waves within the fibre cavity can lead to energy being back-converted into the pumps and signal. Therefore, to avoid this complication for the MM-FOPO only the LP_{01} signal S is oscillated.

The selective oscillation of the signal is achieved by making use of the MMDUX, MMUX and BMS as shown in Figure 6.1. The first two subsystems assure that only light in the LP_{01} mode can be oscillated and that the LP_{11} mode forms the output. The BMS on the other hand is responsible for the percentage of S oscillated in the fibre cavity and the ejection of the residual power of P_1 at every oscillation. The operation of the BMS is similar to the WDMCs in Chapter 5 where the path the optical power takes within the system is spectrally dependent. In this chapter the BMS is modelled using the SMR similarly to how the WDMCs where modelled previously. The output amplitudes of at ports (iii) and (iv) can be found by using:

$$\begin{pmatrix} A_{(\mathrm{iii})}(f) \\ A_{(\mathrm{iv})}(f) \end{pmatrix} = \begin{pmatrix} \sqrt{H(f-f_{\mathrm{P}_1})} & \mathrm{j}\sqrt{1-H(f-f_{\mathrm{P}_1})} \\ \mathrm{j}\sqrt{1-H(f-f_{\mathrm{P}_1})} & \sqrt{H(f-f_{\mathrm{P}_1})} \end{pmatrix} \begin{pmatrix} A_{(\mathrm{i})}(f) \\ A_{(\mathrm{ii})}(f) \end{pmatrix}, \tag{6.1}$$

where

$$H(x) = \begin{cases} In[\%], & x < 0 \\ 100\%, & x \geq 0 \end{cases}, \tag{6.2}$$

f_{P_1} is the frequency of P_1 and In is the insertion percentage of the LP_{01} signal into the oscillator. By using this definition, the spectral dependence of the BMS transmission can be calculated and is presented in Figure 6.2. If the signal frequencies investigated f_S are smaller than f_{P_1}, then a percentage In of the signal will be inserted into the fibre cavity. The round trip transmittance of the signal is also dependent upon the σ loss of the oscillator and is found by:

$$T^{+}(f_S)[\%] = 100\% - In[\%] - SP[\%] \tag{6.3}$$

where SP is the σ loss.

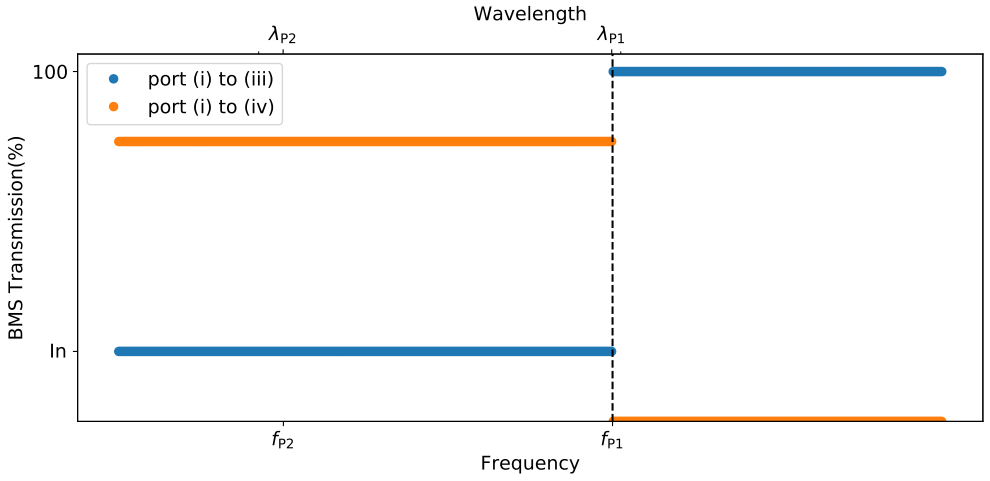

FIGURE 6.2: Transmission between ports in the Beam Splitter.

Finally, it is worth mentioning that in contrast to the optical systems used in the SM-FOPO a more abstract approach has been taken upon the modelling of the subsystems

used to selectively oscillate certain parts of the spectrum. For example, the non-uniform increase of the transmittance of the BMS for frequencies on and above that of the LP_{01} pump may be considered difficult to implement practically. This simplistic approach in building the MM-FOPO model does not, however, negate its value since it is possible to recreate the oscillator system with additional optical systems. Concerning the previous example the recirculation could be achieved by making use of either WDMCs or a Bragg grating with a circulator.

6.2 Numerical Method

The numerical method of the MM-FOPO simulates the spectrum passing through each of the subsystems as was described in Subsection 6.1.1 over a predetermined number of round trips. The models that describe each of these subsystems are highlighted in this section. Following this the operation of the source code is discussed, and attention is drawn to the acceleration techniques used within the final numerical model.

Principal to the operation of the MM-FOPO is the pulse propagation through the TMF. Since the fibre can support more than one mode the MM-GNLSE reported in (2.35) is required to simulate the subsystem. Moreover, the fibre used in this chapter is the one used in Chapter 3, therefore the nonlinear and dispersion part of (2.35) can be simplified to (3.7) and (3.9) respectively. The then simplified MM-GNLSE can be solved by using the SSFM as described in subsection 2.2.3. It is worth mentioning that the MM-GNLSE shown in (2.35) is a set of two coupled equations. Therefore the spectra of the modes are represented separately, that is in two computational vectors of the same length. This representation also allows the propagation of each mode to be considered separately within the other subsystems of the oscillator if so required.

The phase modulation of the signal occurring in PM is inspired by PM_2 described in Subsection 5.2.3. As was shown in the previous chapter the phase of the oscillating signal is modulated by a constant amount at every round trip. Like in the case of the SM-FOPO the constant phase shift applied to the spectrum is calculated at every round trip by using (5.16). In the MM-FOPO the BMS serves the same purpose as the WDMCs did in the SM-FOPO, that is to recirculate a select part of the spectrum. In this model it is simulated by applying (6.1) to the spectrum at every round trip. Similarly, the σ loss is modulated by using the SMR, and at every round trip, the spectrum passing through it is modelled by using (5.8). Finally, the mode splitting and combining in MMDUX and MMUX is achieved by making use of the vectorial nature of the modes as described previously.

As in the previous chapters the source code used to simulate the optical system is written in Python 3.6 while making use of multiple libraries from the scientific Python stack. The operation of the source code used in this chapter is similar to the one used in

Chapter 5 while the definition of the spectrum and the pulse propagation is identical to what was used in Chapter 3. Like in Chapter 5 however the efficient simulation of each of the subsystems is essential since each simulation of the MM-FOPO consists of multiple oscillations and therefore multiple evaluations of the numerical models describing the subsystems. Out of the subsystems described the one with the highest execution times is the solution of the MM-GNLSE. As in the previous chapter, this part of the source code was accelerated by using Cython to translate the Python code into optimised C code. However, the Cython code is further optimised in this chapter by only making use of C/C++ libraries (instead of NumPy and SciPy) during the pulse propagation part of the model. By making use of these optimisations, the numerical model became efficient enough to simulate the MM-FOPO for the cases investigated in this chapter. As with the other models discussed in this thesis the source code is made openly available and is listed third in Appendix A.3. Finally, it is worth mentioning that the source code in this chapter can also simulate the MM-FOPA described in Chapter 3.

6.3 Results

6.3.1 Operation and Power per Oscillation

In the previous sections the apparatus of the MM-FOPO and the numerical model used to simulate it were described. Here this model is used to simulate the oscillator for various parameters in order to investigate the behaviour of the oscillating and outputted waves. Following this the efficiency of conversion from the LP_{01} signal to the LP_{11} idler is evaluated and compared to the equivalent efficiency of the MM-FOPA described in Chapter 3.

The fibre used within the MM-FOPO simulations in this chapter is the same as the one used to show IM-FWM in Chapter 3. The parameters used to evaluate the nonlinear operator (3.7) of the MM-GNLSE have been descried in Subsection 3.1.2 and Section 3.2. The dispersion operator shown in (3.9) can also be evaluated by the values highlighted in Subsections 3.1.3 and 3.3.1. As stated in the previous sections the oscillator is simulated over a predetermined number of round trips until a convergent state is reached. The output power of the two idlers is then calculated as the average power of the last 50% of the oscillations (after the convergent state is reached). The CE of each of the LP_{11} idlers is defined as the ratio of their average output power and the input signal power. The RIN is also calculated by using (5.18).

In order to compare the CE of the MM-FOPO to the MM-FOPA the wavelengths and powers considered in Chapter 3 are rehashed here as inputs to the oscillator. The wavelength of the LP_{01} pump is kept constant at $\lambda_{P1} = 1549\,\text{nm}$ while that of the LP_{11} pump is set to $\lambda_{P2} = 1553.5\,\text{nm}$. The signal wavelength is varied, which in turn varies

the wavelengths of the BS and the PC idlers. The input pump powers of the two pumps are $P_{\mathrm{P1}} = 27.5\,\mathrm{dBm}\,(0.56\,\mathrm{W})$ and $P_{\mathrm{P2}} = 26.5\,\mathrm{dBm}\,(0.45\,\mathrm{W})$ respectively while the input signal power is $P_{\mathrm{S}} = 3.5\,\mathrm{dBm}\,(2.24\,\mathrm{mW})$. It is worth mentioning that like in Chapter 3 the waves considered are CW.

As was seen in the previous chapter fluctuations of the oscillating and output waves with respect to the number of round trips can occur in FOPOs. However, for the parameters considered here, parametric conversion would not occur in the MM-FOPO unless it is seeded. This is compatible with the below threshold seeded configuration discussed in Subsection 5.3.3.2. Therefore the oscillating and output power of the waves is expected to be relatively stable in these regimes. To highlight this, the oscillator is simulated for 200 round trips with a σ loss of 1 dB and an insertion percentage of 20% which leads to the transmittance of the signal being calculated at 59.43%. The powers of the input waves and the wavelengths of the pumps are stated above while the signal wavelength is set to $\lambda_S = 1549.3\,\mathrm{nm}$. The resulting LP_{11} idlers are $\lambda_{\mathrm{PC}} = 1553.2\,\mathrm{nm}$ and $\lambda_{\mathrm{BS}} = 1553.8\,\mathrm{nm}$. As in Chapter 3 the length of the fibre is set to 1 km.

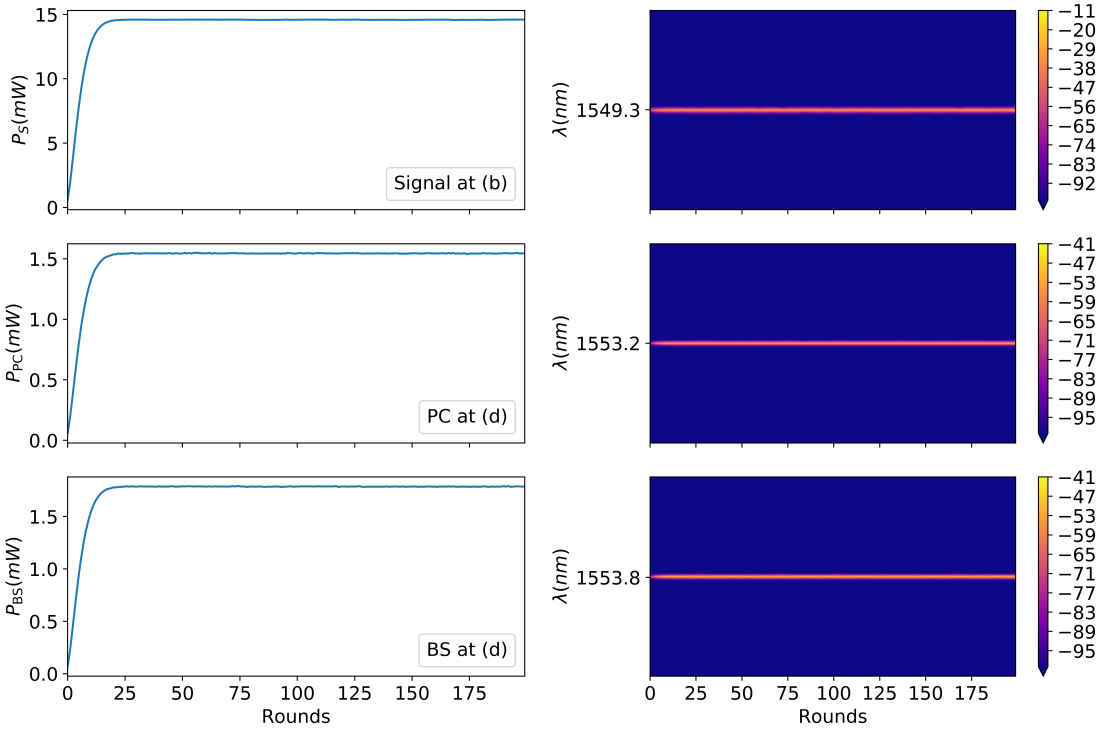

FIGURE 6.3: Power (left) and spectra (right) per oscillation of the signal at position (b) and BS and PC at position (d) of the MM-FOPO. The spectra are in units of dB and are normalised to the power of the LP_{01} pump. The signal wavelength is set to $\lambda_S = 1549.3\,\mathrm{nm}$ which results in a PC and BS idlers of $\lambda_{\mathrm{PC}} = 1553.2\,\mathrm{nm}$ and $\lambda_{\mathrm{BS}} = 1553.8\,\mathrm{nm}$ respectively. The wavelengths and powers of the rest of the input waves are found in the text.

Figure 6.3 depicts the power and spectra per round trip of the oscillating signal at point (b) of the MM-FOPO and the output LP_{11} idlers at point (d). As can be seen, the power of the oscillating signal increases to its convergent state at $\approx 14\,\mathrm{mW}$ after a few

round trips. The increased signal power within the fibre cavity results in elevated output powers of the idlers of $P_{\mathrm{PC}} \approx 1.5\,\mathrm{mW}$ and $P_{\mathrm{BS}} \approx 1.6\,\mathrm{mW}$. After the first few oscillations, the power and spectra of the waves considered become relatively stable. This behaviour was also observed in the below threshold seeded configuration of the SM-FOPO and is seen in all the simulations considered in this chapter.

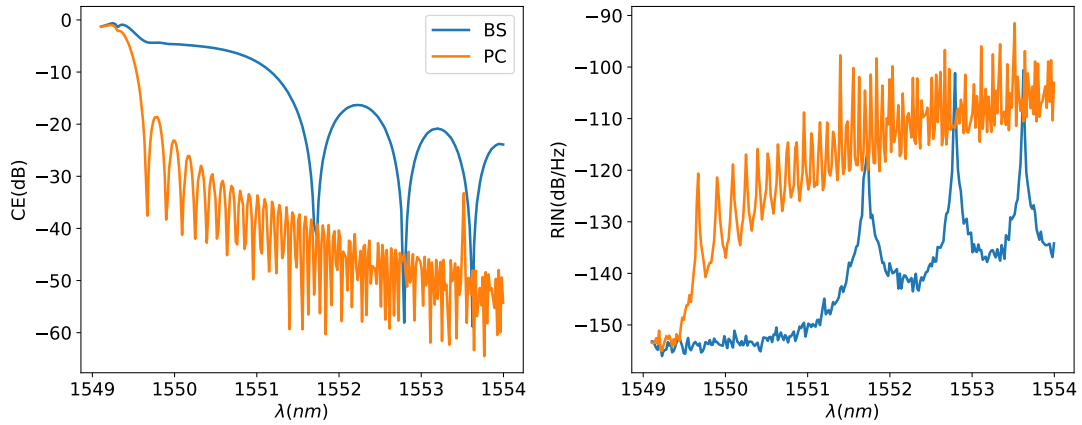

FIGURE 6.4: Conversion efficiency (left) and relative intensity noise (right) of the of the BS and PC of the MM-FOPO with respect to the signal wavelength. The wavelengths and powers of the waves are highlighted in the text.

To investigate the behaviour of the CE and RIN the signal wavelength is varied between $\lambda_S = 1549\,\mathrm{nm} - 1554\,\mathrm{nm}$. This results in outputted BS and PC of $\lambda_{\mathrm{BS}} = 1553.5\,\mathrm{nm} - 1558.5\,\mathrm{nm}$ and $\lambda_{\mathrm{PC}} = 1553.5\,\mathrm{nm} - 1548.5\,\mathrm{nm}$. The CE and RIN of the BS and the PC is shown in Figure 6.4. The trend of the CE is similar to what was observed in the MM-FOPA shown in Figure 3.4 with the oscillator exhibiting CEs $\approx 6\,\mathrm{dB}$ higher. Additionally, for both the idlers the RIN starts at $\approx -155\,\mathrm{dB/Hz}$ with a small signal and $P1$ wavelength separation. As the separation is increased however the RIN increases which is attributed to the decrease in output idler power. This behaviour is expected since, as was seen in Figure 6.3, the output powers of the idlers are relatively stable. *Ergo* the standard deviation of the power is relatively constant with respect to signal-pump wavelength separation. Since this stable output idler power is observed for all the results simulated in this chapter the RIN will not be evaluated hereafter. Instead the focus will be on optimising the CE of the idlers.

6.3.2 Signal Insertion and Loss

In the previous subsection the σ loss and insertion percentage of the signal where set to $1\,\mathrm{dB}$ and $20\,\%$ respectively and kept constant. However, both these parameters are critical to the power of the oscillating signal and by extension the CE of the PC and BS idlers. It is therefore of interest to evaluate where these parameters result in the highest efficiency for the oscillator.

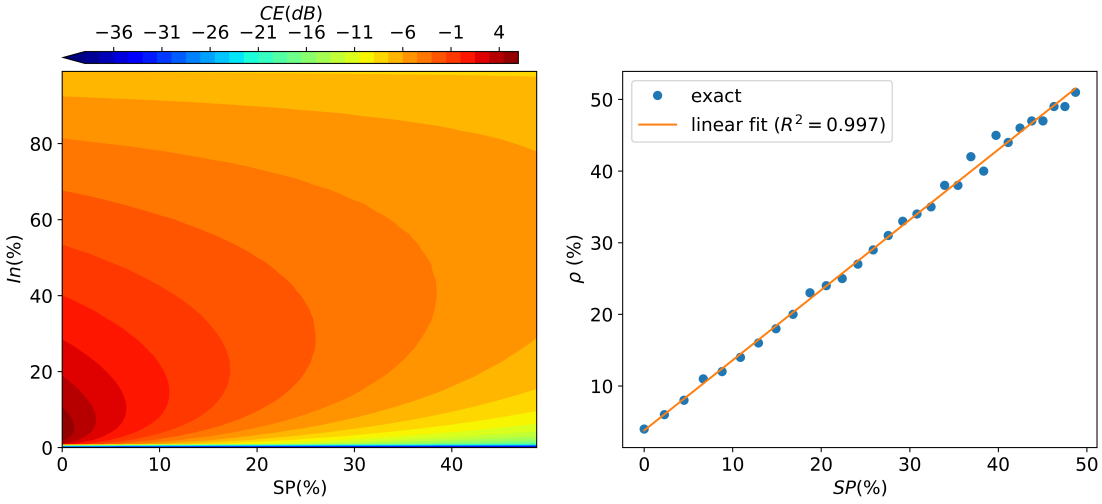

(a)

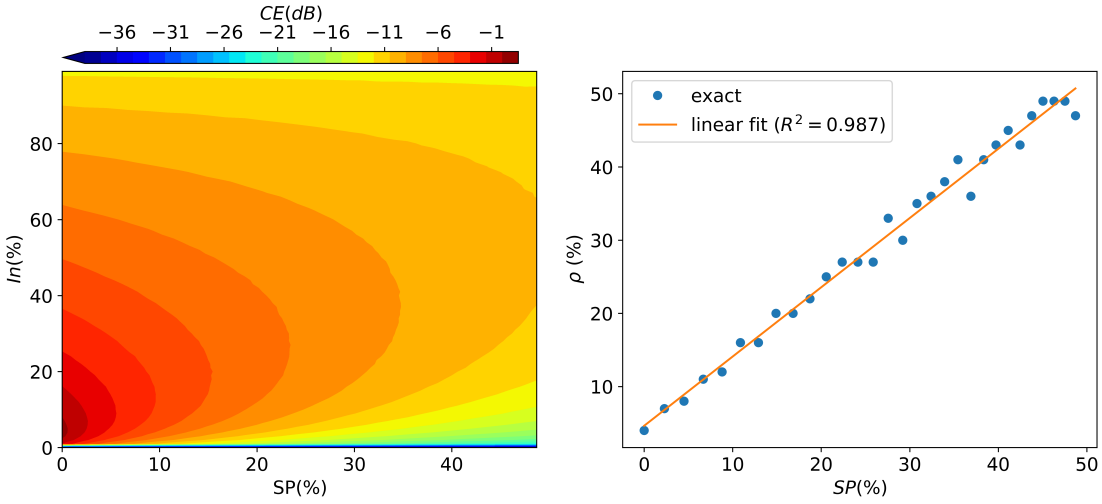

(b)

FIGURE 6.5: On the left, the CE of the BS (a) and PC (b) with respect to the σ loss and signal insertion percentage. On the right hand side the exact and linearly fitted insertion at maximum CE ρ with respect to the σ loss. The signal wavelength is set to $\lambda_S = 1549.5\,\text{nm}$ which results in a PC and BS idlers of $\lambda_{\text{PC}} = 1553\,\text{nm}$ and $\lambda_{\text{BS}} = 1554\,\text{nm}$ respectively. The wavelengths and powers of the rest of the input waves are found in the text.

The MM-FOPO is simulated for 200 round trips for a varying σ loss and signal insertion percentage. The powers and pump wavelengths are the same as quoted in the previous subsection while the signal wavelength is set to $\lambda_S = 1549.5\,\text{nm}$. The CE of the BS and PC with respect to the signal insertion and σ loss percentage are shown in Figure 6.5. As can be expected at 0 % insertion there is no output power in the idlers. As the insertion is increased the CE of both the idlers rises. The insertion where the CE is maximum for every σ loss considered, ρ, is plotted on the right-hand side of the figure with respect to the σ loss. A linear fit is then applied to this best insertion with respect to the σ loss

and is shown to be

$$\rho_{\mathrm{BS}}\left(SP\right) = 0.98SP + 3.82, R^2 = 0.997 \tag{6.4}$$

and

$$\rho_{\mathrm{PC}}\left(SP\right) = 0.95SP + 4.63, R^2 = 0.987 \tag{6.5}$$

for BS and PC respectively. Both of the linear interpolations show a coefficient of determination R^2 close to unity and therefore are considered good fits. In the exact data, at $SP = 0\,\%$ both the idlers experience maximum conversion efficiency at $In = 4\,\%$ which in both cases is close to the constant term in the interpolations. Also, the polynomial coefficient in both cases is close to unity. One could, therefore, speculate that the insertion where the highest conversion efficiency occurs can be approximated by:

$$\rho\left(SP\right) \approx SP + W, \tag{6.6}$$

where W is the insertion percentage where the highest CE occurs at $0\,\%$ σ loss. This hypothesis was investigated and validated for other input wavelengths, some of which are shown in Appendix C.

The analysis described above provides the insertion with the highest CE for a constant signal wavelength. However, within this study as in Chapter 3 the signal wavelength is varied to investigate the bandwidth where the CE of the BS and PC is high. Therefore a signal insertion percentage which is optimal over the investigated bandwidth needs to be established. For the pump wavelengths and wave powers given previously the signal wavelength is varied between $\lambda_S = 1549\,\mathrm{nm} - 1554\,\mathrm{nm}$ resulting in outputted BS and PC idlers of $\lambda_{\mathrm{BS}} = 1553.5\,\mathrm{nm} - 1558.5\,\mathrm{nm}$ and $\lambda_{\mathrm{PC}} = 1553.5\,\mathrm{nm} - 1548.5\,\mathrm{nm}$ respectively. In addition, for each of the signal wavelengths considered the insertion percentage is varied while the σ loss is kept constant at $1\,\mathrm{dB}$. The oscillator is then simulated for 200 round trips as before. The CE of the BS and PC is shown in the left hand side of Figure 6.6. The average CE over the signal wavelengths considered is also shown on the right-hand side of the figure for each of the idlers. This average is then interpolated using a cubic interpolation function, and the insertion where the maximum average CE occurs is found by using the Limited-memory Broyden–Fletcher–Goldfarb–Shanno-B (L-BFGS-B) method [112]. For the BS the maximum average CE is found at $In = 22.9\,\%$ while for the PC it is found at $In = 23\,\%$. As discussed earlier these percentages depend upon the insertion percentage where the highest CE occurs at $0\,\%$ σ loss. Therefore they are dependent upon the input parameters like the waves wavelengths and powers. However in order to investigate the behaviour of the oscillator with respect to the variation of other variables the insertion percentage of the signal is kept constant at $23\,\%$ for the rest of this chapter.

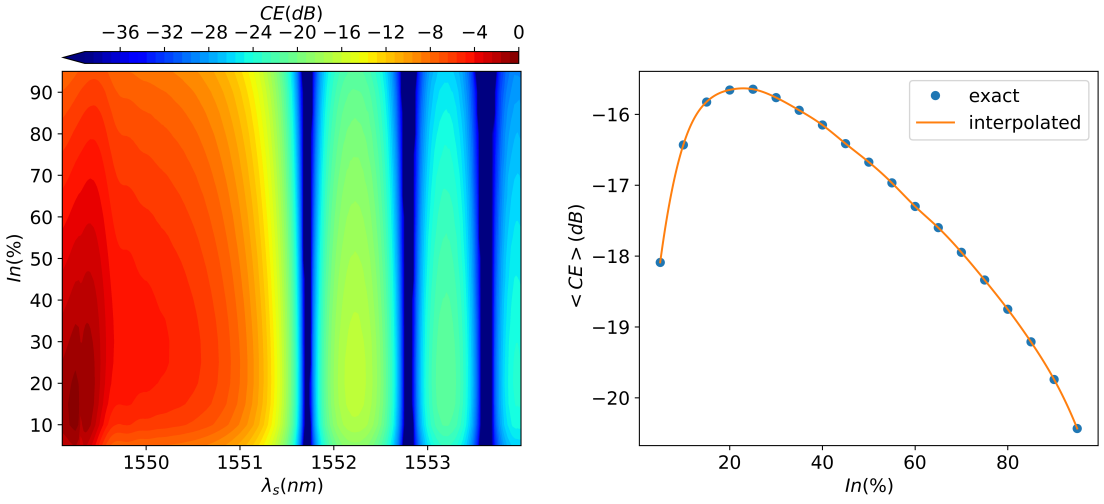

(a)

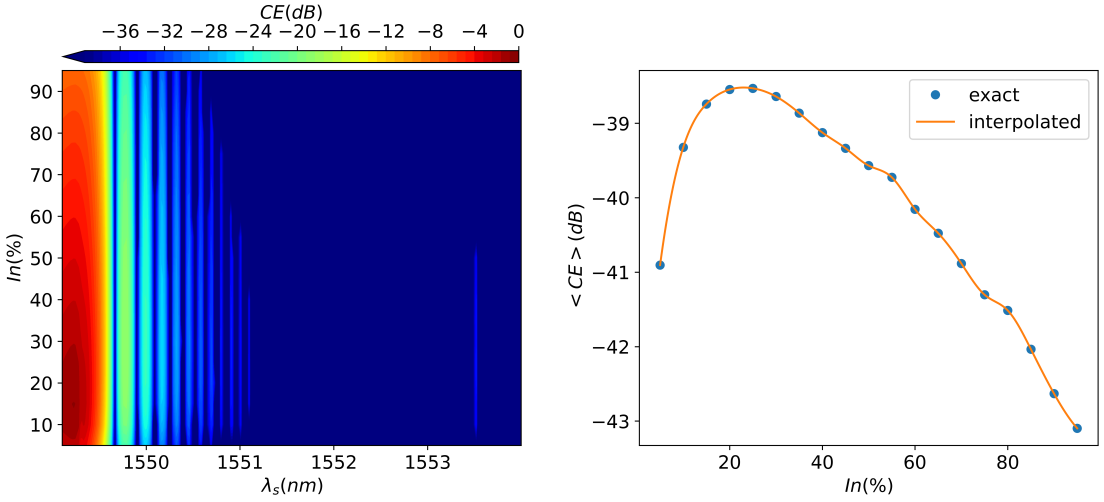

(b)

FIGURE 6.6: On the left, the CE of the BS (a) and PC (b) with respect to the signal wavelength and insertion percentage. On the right hand side the average CE over the signal wavelengths considered is plotted against signal insertion percentage. The signal wavelength is varied between $\lambda_S = 1549\,\text{nm} - 1554\,\text{nm}$ resulting in outputted BS and PC of $\lambda_{\text{BS}} = 1553.5\,\text{nm} - 1558.5\,\text{nm}$ a $\lambda_{\text{PC}} = 1553.5\,\text{nm} - 1548.5\,\text{nm}$ respectively.

6.3.3 Length of the Fibre

In the previous subsections, the operation and transmittance of the MM-FOPO were discussed. However, as has been highlighted multiple times in this thesis the prime motivation for the use of FOPOs over FOPAs is that smaller length fibres can be used for high-efficiency parametric conversion. In this subsection, the MM-FOPO is simulated for a varying length of the TMF in order to illustrate the behaviour of the CE of the two idlers with a varying fibre length. In addition, the same investigation is conducted for the MM-FOPA in order to compare the efficiencies of the two systems. Finally, a MM-FOPO with a smaller length fibre is simulated for varying signal and P2 wavelengths.

The resulting CE of the two idlers is compared to that of the MM-FOPA shown in Subsection 3.3.2.

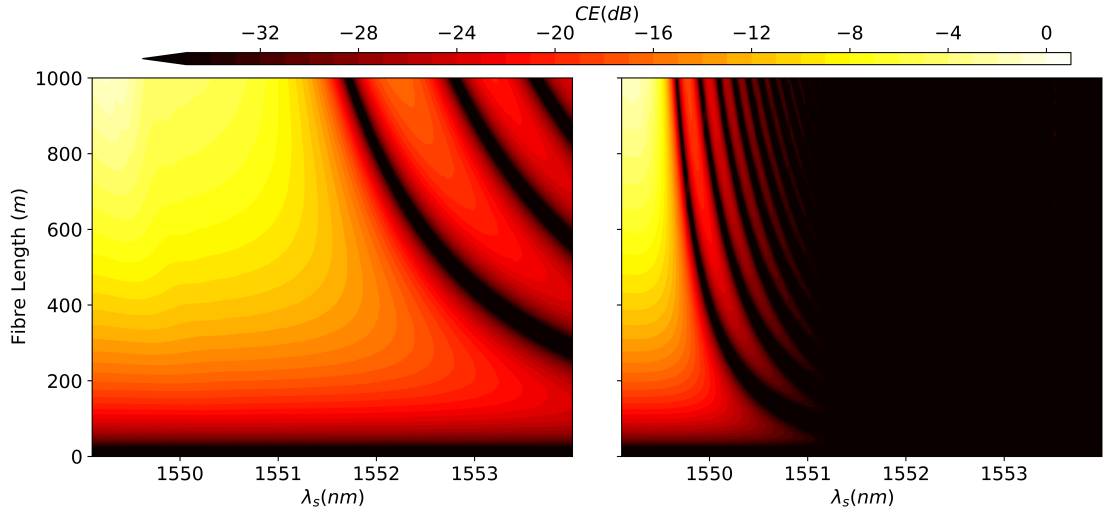

(a)

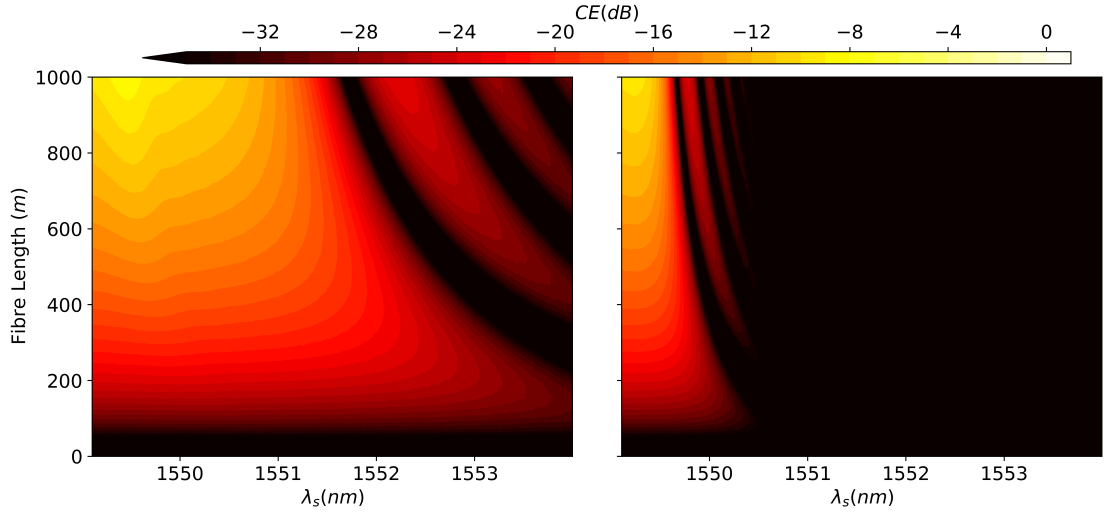

(b)

FIGURE 6.7: Conversion efficiency of BS (left) and PC (right) of the MM-FOPO (a) and MM-FOPA (b) with respect to the signal wavelength and fibre length. The pump powers and wavelengths are quoted in the text.

To examine the bandwidth where the CE of the two idlers is high with respect to fibre length the oscillator is simulated for 200 round trips with the below parameters. The input wave powers are the same as discussed in the previous subsections and the pump wavelengths are set to $\lambda_{P1} = 1549\,\text{nm}$ and $\lambda_{P2} = 1553.5\,\text{nm}$ respectively. On the other hand the signal wavelength is varied between $\lambda_S = 1549\,\text{nm} - 1554\,\text{nm}$ resulting in outputted BS and PC of $\lambda_{BS} = 1553.5\,\text{nm} - 1558.5\,\text{nm}$ and $\lambda_{PC} = 1553.5\,\text{nm} - 1548.5\,\text{nm}$ respectively. Finally the σ loss is kept constant at 1 dB. For these parameters the fibre length is varied from 0 m to 1000 m on a linearly spaced grid.

Figure 6.7(a) shows how the CE of the PC and BS varies with respect to signal wavelength and fibre length. As stated earlier the numerical model described in this chapter is also able to simulate a MM-FOPA. A simulation with the aforementioned input parameters was conducted upon a MM-FOPA, and the behaviour of the CE with respect to fibre length and signal wavelength is shown in Figure 6.7(b). It is worth mentioning that like in the case of the oscillator the CE in each case is defined as the ratio of the idlers output power and the signals input power. This is unlike the definition used for the MM-FOPA described in Chapter 3.

For both the idlers considered, in the case of the MM-FOPO and MM-FOPA, the maximum CE with respect to wavelength decreases as the fibre length is reduced. However, a smaller fibre length exhibits a larger bandwidth where the CE is maintained higher than $-20\,\mathrm{dB}$. This behaviour is present in both the MM-FOPA and MM-FOPO with the oscillator showing large CE bandwidth for fibre lengths of up to $\approx 100\,\mathrm{m}$. The amplifier on the other hand maintains $CE > -20\,\mathrm{dB}$ for a fibre length of $\approx 200\,\mathrm{m}$ over a smaller bandwidth. The increased magnitude of the CE of the oscillator with respect to the amplifier is present for all the signal wavelengths and fibre lengths considered with an average increase of $\approx 6.5\,\mathrm{dB}$ being measured for both the PC and BS. This increase in CE is attributed to the increased signal power that is passed through the fibre within the oscillator when compared to the amplifier.

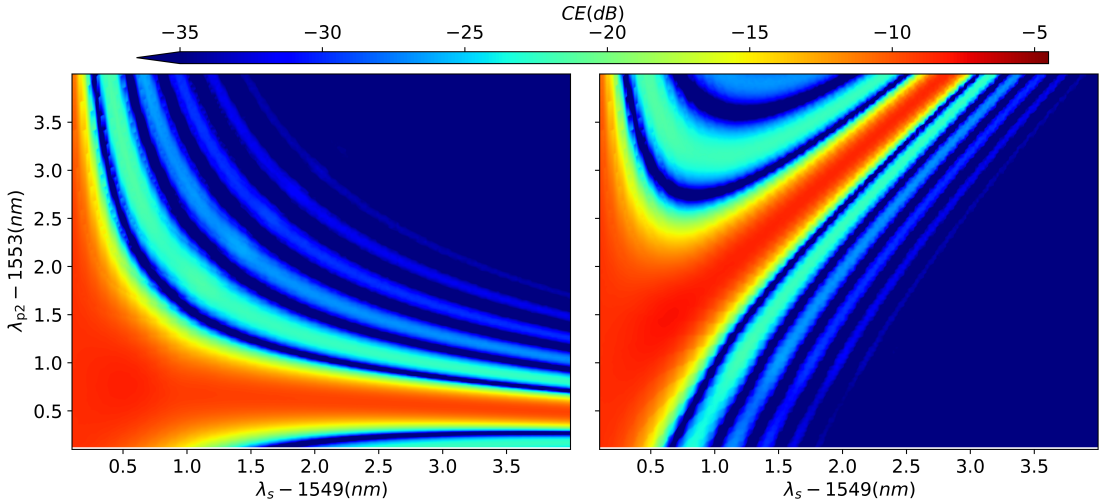

FIGURE 6.8: Conversion efficiency of the BS (left) and PC (right) with respect to the signal and P_2 wavelengths. The parametric conversion is conducted in a MM-FOPO with a $500m$ fibre and the input powers and wavelengths can be found in the main text.

Since large operational bandwidths are observed for smaller length fibres and the application of the MM-FOPO exhibits higher magnitudes of CEs, the oscillator is simulated next for a varying signal and P_2 wavelengths equivalent to the simulation presented in Subsection 3.3.2. The fibre length is reduced to 500 m (half of the original fibre length). The signal and P_2 wavelengths are varied between $1549\,\mathrm{nm} - 1553\,\mathrm{nm}$ and

1553 nm − 1557 nm respectively. The CEs of the BS and PC idlers are shown in Figure 6.8. The efficiencies resulting from the oscillator simulation shown in this figure are equivalent to those presented in Figure 3.4 by using a MM-FOPA. By comparing the two figures, one can first see that the trend of the CEs for the two idlers is similar. In addition, even though half the fibre length is used in the oscillator simulation, similar maximum CEs are observed in both systems. As stated earlier this is attributed to the increase of oscillating signal power within the oscillator cavity. The utilisation of a smaller length fibre demonstrates that high CEs are maintained for a larger bandwidth of the signal and P_2 wavelengths as was indicated earlier. For example, with the P_2 wavelength set to $\lambda_{P2} = 1553.5$ nm the CE of the BS is maintained to levels higher than -10 dB for all the signal wavelengths considered, whereas the CE of the MM-FOPA with the same input parameters exhibits CEs under -10 dB for signal to P_1 separations of over 1.5 nm according to Figure 3.4. This behaviour is repeated for other P_2 wavelengths.

6.4 Conclusion

In this chapter a MM-FOPO system was presented that can convert energy between the LP_{01} and the LP_{11} modes. To the best of the authors knowledge this is the first time such a system has been investigated. The oscillator encompassed multiple subsystems that were assembled in order to oscillate a signal within the oscillator cavity and by doing so increase the energy conversion between the modes. In addition, the numerical models used to simulate each of the subsystems (and by extension the oscillator) was detailed and the steps taken to minimise its execution time of the source code where discussed.

The oscillator was initially simulated to investigate the behaviour of the circulating and output waves. It was found for the input parameters of the oscillator considered in this chapter that the power per oscillation of the signal and outputted idlers was relatively stable at the convergent state. By extension, it was found that the RIN of the output idlers varied primarily with respect to the average output power and not the standard deviation. This was attributed to the MM-FOPO operating below threshold for all the input parameters considered in this chapter. The CE of the idlers simulated with respect to a varying signal wavelength was found to behave similarly to those exhibited by the MM-FOPA detailed in Chapter 3. It is worth mentioning though that the CEs simulated by using the oscillator exhibited higher values for the same input parameters by about 6.5 dB.

The behaviour of the CE with respect to the insertion percentage of the signal and the internal losses of the system was also investigated. It was found that the insertion percentage where the CE is maximum could be approximated by the addition of the internal

losses of the oscillator and the insertion percentage where the highest CE occurs at 0% internal loss. Following this, the length of the fibre was varied, and it was found that the bandwidth where high CE occurs was larger for shorter fibres. This behaviour was also present when simulating a MM-FOPA with the same input parameters. However, as was seen previously the CE calculated by using MM-FOPO is higher than in the MM-FOPA. Finally, the CE of the idlers with respect to the signal and LP_{11} wavelength were calculated for a 500 m length fibre equivalent to what was conducted in Subsection 3.3.2 for the MM-FOPA. The trend and magnitude of the CE where found to be similar for both systems with the oscillator demonstrating larger bandwidths where high CE is maintained due to the smaller length fibre utilised.

In Chapter 5 it was stated that oscillating multiple waves could lead to energy being back-converted from the idlers back to the pump and signal. Therefore the oscillator presented in this chapter was structured to oscillate only one wave, the signal. However, in extensions of this study the oscillation of other waves could be considered. For example the BS idler could be oscillated in the oscillator cavity which could lead to a higher CE of the PC via degenerate FWM between P_2, BS idler and PC idler as the pump, signal and idler respectively.

As stated earlier it was shown that shorter length fibres result in an increased bandwidth where the CE remains high. This phenomenon was observed for the MM-FOPA and MM-FOPO. This demonstrates that the application of short length fibres is beneficial to both systems. The magnitude of the CE to the idlers can also be increased by making use of either higher pump powers, using fibres with a higher nonlinear coefficient or by tailoring the refractive index profile to maximise the overlap integrals between the modes of interest. As was seen in this chapter however MM-FOPOs can also be used to increase the CE bandwidth for the same fibre.

It is worth mentioning that for the MM-FOPO described in this chapter 1 W pump powers are required to generate the LP_{11} idler at the order of milliwatts with an output detuned up to 4 nm. Both the CE and detuning are much smaller than what has been achieved with SM-FOPOs. However, the purpose of the MM-FOPO described in this chapter is to convert light between fibre modes as well as wavelengths. Nevertheless, its efficiency and operating bandwidth would need to be increased for it to be used for wavelength and mode conversion in laser or telecommunication systems. As previously stated, the fibre employed for the MM-FOPO is the same as the one used for the MM-FOPA described in Chapter 3. As stated within that chapter the CE of a MM-FOPA could be improved by utilising a fibre where the overlap integral between the modes is higher. In addition, the dispersion profile of the two modes can be modified to increase the operating bandwidth of the amplifier. Using such a fibre would also increase the CE and operating bandwidth of the MM-FOPO making its application for wavelength and mode conversion more attractive.

Previously within this thesis it was mentioned that recent studies have shown that non-uniformities along the propagation length can reduce the CE of IM-FWM [22]. The application of a MM-FOPO could potentially diminish this effect since the oscillating wave would experience the same non-uniformities at every oscillation. Further studies on MM-FOPOs should aspire to model these non-uniformities within the fibre and seek to compare the CE between the oscillator and an equivalent parametric amplifier.

Chapter 7

Conclusions

7.1 Overview

FOPAs and FOPOs have been presented as attractive devices that can be used for wavelength conversion [10]. These all-fibre systems are utilised to convert light to frequencies other than those that the gain medium of a laser operates within, therefore commissioning applications where light at 'exotic' wavelengths is required. In addition, these parametric systems are used in the telecommunications industry to convert energy between the channels of WDM systems [1]. Within the introduction of this thesis, it was also mentioned that SDM systems and in particular multi-mode fibres are used to increase the number of channels of a single fibre. The fibre based parametric systems discussed in this thesis can also be utilised to convert energy between these fibre modes efficiently. Throughout this research project, numerical models capable of simulating both FOPAs and FOPOs have been presented. These models were then used to investigate the efficiency and noise of these parametric systems along with the underlying physical mechanisms that dictate these values.

In Chapter 3 the model that simulates a MM-FOPA was presented. Within this fibre system, energy is converted from a pump and signal in the LP_{01} mode and a pump in the LP_{11} mode to the BS and PC idlers in the LP_{11} mode. This study was conducted in conjunction with Dr Søren Friis and Dr Francesca Parmigiani who experimentally examined the system. The numerical method built to simulate the MM-FOPA was then validated against the experimental results provided by the collaborators. Following this, the model was used to investigate how the CE of this process behaves for varying wavelengths of the signal and LP_{11} pump. From this simulation, it was found that the output power of the two idlers is predominately dependent upon their phase mismatch parameter. Additionally, cascade FWM processes were also found to contribute to the CE of the two idlers.

A substantial part of this research project focused upon the modelling and application of an all-fibre SM-FOPO system. The oscillator apparatus is comprised of multiple subsystems. By extension, the numerical method of the SM-FOPO is constructed as an accumulation of the models that describe these sub-systems. Each of the sub-models was validated and accelerated such that the oscillating wave could be recirculated hundreds or even thousands of times such that the convergent state could be reached. The model was then used to simulate the oscillator for two configurations. In the first, a single pump is inputted into the systems while in the later the oscillator is also seeded by a low power signal. In the non-seeded configuration, at above threshold pump powers, the oscillating signal is amplified from noise. The increased signal power within the fibre cavity then mediates energy conversion to the desired output, the idler. For all the pump wavelengths considered with this configuration, the CE of the oscillator is primarily depended upon its transmittance through fibre cavity and the power of the pump. The RIN of the output, however, was found to be $\approx -110\,\mathrm{dB/Hz}$ for all the pump wavelength considered. In order to decrease the output noise of the system, a seeded oscillator was suggested. In this configuration the RIN was found to be lowered to levels of up to $\approx -175\,\mathrm{dB/Hz}$. This behaviour was only present however at pump powers below the unseeded thresholds. For pump powers above these thresholds, the RIN is increased to values similar to what was shown in the unseeded configuration. The low noise levels show that the seeded FOPO is suitable for applications where low noise output is essential. However, their application is limited to pump powers lower than that of the unseeded threshold. In addition, light sources at the seed wavelengths are required which may prove challenging. Alternatively, the unseeded SM-FOPO is not limited by these obstacles and could be used in applications where high RIN is not a hindrance. Finally, the optical apparatus required phase modulators such that back-conversion of power to the pump and destructive interference between the oscillating and seeded signal does not occur. The later negative effect can be negated by adjusting the relative phase between the two signals. On the other hand, the energy back-conversion can be avoided by only oscillating one wave within the fibre cavity as was illustrated by [106–108].

During initial investigations into the SM-FOPO apparatus it was found that it was not computationally feasible to use the SM-GNLSE for the pulse propagation part of the model. This challenge led to the derivation of the BNLSE presented in Chapter 4. The equation allows for dense frequency bands, arbitrarily placed within the spectrum to be simulated during propagation through a fibre. Contrary to previous CNLSEs this method is primarily suited for simulations of FOPOs since it is not limited by the undepleted pump approximation and accurately incorporates Raman dependent factors between the bands. Without the use of the BNLSE in the SM-FOPO model the accurate simulation of the parametric conversion would not be possible within the time-frame of this research project. This is because of the spectral density required to resolve the parametric sidebands accurately along with the requirement of the FFT algorithm

for the frequency grid to be linearly spaced. Finally, it is worth mentioning that the equation is not only suitable for simulating FOPAs and FOPOs and can be used to simulate dispersive and nonlinear interactions between waves over large bandwidths.

Following the completion and publication of the MM-FOPA study detailed above research emerged that indicated that the CE of MM-FOPAs is reduced because of fabrication imperfections along the propagating direction of the fibre [22]. As previously stated, FOPOs can be used to alleviate this effect by utilising shorter length fibres for efficient wavelength conversion. In Chapter 6 the conclusions drawn from the SM-FOPO study where used to expand the MM-FOPA system into a MM-FOPO. In this oscillator system only the LP_{01} signal is recirculated within the fibre cavity while the BS and PC idlers still form the desired output as in the MM-FOPA. This study is, to the best of the authors knowledge, the first time a MM-FOPO has been applied for energy conversion between fibre modes. A numerical method capable of simulating the system was created and its execution time minimised. By utilising this model to simulate the MM-FOPO it was found that the CE of the two idlers was increased when compared to the equivalent efficiencies shown by the MM-FOPA model. This increase in output idler power is attributed to the increased power of the oscillating signal that the FOPO provides. The length of the fibre was also varied for the MM-FOPA and MM-FOPO systems. In both cases, it was found that the magnitude of the CE is maintained over larger signal bandwidths for smaller length fibres. This, along with the increased values of the CE exhibited by the MM-FOPO makes such an oscillator attractive for energy conversion between modes and wavelengths over large bandwidths. The MM-FOPO was then finally simulated with varying LP_{11} pump and signal wavelengths for the same input parameters used in the MM-FOPA but with the fibre length being half the original size. The CE of the two idlers was found to be at a similar magnitude to those simulated by the MM-FOPA even though half the fibre was used. In addition, the domains where high CE is maintained were larger than the equivalent MM-FOPA owing to the smaller fibre length used. This increased operational bandwidth of the MM-FOPO could make it attractive for wavelength/mode conversion within the telecommunications industry. However, as previously stated, to increase the CE of such devices fibres with higher nonlinearities and overlap integrals between modes need to be considered. Furthermore, smaller length fibres are expected to increase the operational bandwidth of the parametric device. If the increased nonlinearity of the fibres used counteracts the decrease of the CE that results with the reduction of the fibre length, MM-FOPOs could be devised that could operate over the entire telecommunications C band ($\approx 35\,\mathrm{nm}$).

The numerical investigations of FOPAs and FOPOs that have been presented in this study show that these systems can be used for energy conversion between wavelengths and fibre modes. The efficiency of parametric conversion was found to be primarily dependent upon the input waves powers and the phase mismatch parameter as indicated by the background theory. Particular attention within this thesis was drawn into the

simulation of FOPOs since it has been identified that they can be used for wavelength conversion while using shorter length fibres, therefore, reducing the negative impact fabrication imperfections have upon the CE. As stated earlier these oscillator systems can be used in applications where low noise and output powers is required or for high output power applications whose noise levels are not a hindrance. The efficiency of the oscillators also depends upon the relative phase of the waves involved in the parametric conversion and to avoid energy back-conversion only one of the waves should oscillate within the fibre cavity. The novel MM-FOPO described in this thesis is a system that adheres to these principles for low noise and efficient power conversion between fibre modes.

7.2 Potential Extensions

While the numerical models presented in this research project provide an accurate description of FOPAs and FOPOs they could be expanded to simulate additional systems. In this subsection potential extensions of the research conducted within this thesis are identified.

In Chapter 4 the BNLSE was derived and validated. This equation allows for efficient and accurate simulations of waves separated over ultra-large bandwidths, however it only simulates the propagation of single-mode waves. Yet, optical fibres are only single mode within a certain bandwidth. Therefore simulations over large bandwidth separations should incorporate multiple modes. Further research should attempt to derive a multi-mode BNLSE.

The FOPO systems simulated within this thesis have been pumped and seeded by CW waves and these waves have been modelled as Dirac-delta functions within the frequency spectrum. Interpolating the input with such a function is an approximation since when CWs are inputted into FOPOs a frequency jitter is applied in order to avoid the adverse effects of stimulated Brillouin scattering [92]. Further numerical studies into FOPOs should consider input CW waves with a linewidth and should investigate if and by how much this linewidth affects the CE and RIN of the optical system. Furthermore, instead of CW, pulse waves could be considered as inputs to the oscillators. Investigations into these fibre systems should be optimised such that the pump and oscillating wave overlap within the time domain such that parametric conversion can be maximised [10].

In both the amplifier and oscillator models simulated within the thesis pulse propagation is considered along a single direction within an optical fibre. The signals of the oscillators in particular are recirculated outside of the fibre and always propagate in a single direction. An alternative optical apparatus could have the signal reflected and counter-propagated through the parametric fibre prior to it being reflected again and propagated with the pump for the next oscillation. The selective reflection of the waves

could be achieved by utilising fibre Bragg gratings. Such a bidirectional FOPO would form a more compact and straightforward all-fibre system than the unidirectional oscillators presented in this thesis. However, the theoretical and numerical modelling of the oscillators would diverge from the oscillator models described in this research project since the GNLSE only operates on waves propagating within a single direction.

The study presented in Chapter 6 foresaw the novel investigation of a MM-FOPO with the purpose of energy conversion between modes. Within the apparatus presented the signal oscillated within the fibre cavity, and the BS and PC idlers formed the output. A multitude of MM-FOPO configurations could be designed to oscillate waves other than the signal. For example, the BS could oscillate within the fibre cavity which could increase the power of the output PC via degenerate FWM. Furthermore, FOPOs with more than two modes could be designed to achieved energy conversion between those modes.

Finally, as stated in the introduction, each of the studies conducted within this research project has a published and open sourced source code associated with it. A large portion of this research project was spent on accelerating these numerical models; this was particularly required to simulate the FOPOs. These models have been used to simulate the optical systems they describe for several parameters. However, they could be used for further investigations into FOPAs and FOPOs. These studies could for example consider other fibres as the gain medium in the parametric systems. Alternatively, sections of the source code could be utilised to simulate novel FOPO configurations.

Appendices

Appendix A

Research Project Output

A.1 Journal Articles

1. S. M. M. Friis, I. Begleris, Y. Jung, K. Rottwitt, P. Petropoulos, D. J. Richardson, P. Horak, and F. Parmigiani, "Inter-modal four-wave mixing study in a two-mode fiber," Opt. Express 24, 30338-30349 (2016)

2. I. Begleris and P. Horak, "Frequency-banded nonlinear Schrödinger equation with inclusion of Raman nonlinearity," Opt. Express 26, 21527-21536 (2018)

3. I. Begleris and P. Horak, "Efficiency and intensity noise of an all-fiber optical parametric oscillator," J. Opt. Soc. Am. B 36, 551-558 (2019)

A.2 Conference Proceedings and Presentation

1. **(Conference Publication)** S. M. M. Friis, Y. Jung, I. Begleris, P. Horak, K. Rottwitt, P. Petropoulos, D. J. Richardson, and F. Parmigiani, "Detailed phase matching characterization of inter-modal four-wave mixing in a two-mode fiber," in Conference on Lasers and Electro-Optics, OSA Technical Digest (online) (Optical Society of America, 2016), paper JTu5A.49.

2. **(Conference Publication)** F. Parmigiani, Y. Jung, S. M. M. Friis, Q. Kang, I. Begleris, P. Horak, K. Rottwitt, P. Petropoulos, D. J. Richardson, "Study of Inter-Modal Four Wave Mixing in Two Few-Mode Fibres with Different Phase Matching Properties," ECOC 2016; 42nd European Conference on Optical Communication, Dusseldorf, Germany, 2016, pp. 1-3.

3. **(Conference Proceedings & Oral Presentation)** I. Begleris, S. Friis, F. Parmigiani and P. Horak (2016) Conversion efficiency and bandwidth of intermodal four wave mixing in two-mode optical fibres. At Photon16, United Kingdom. 05 - 08 Sep 2016.

4. **(Conference Publication & Oral Presentation)** I. Begleris and P. Horak, "Cascade simulations of unidirectional fiber optical parametric oscillators," 2017 International Conference on Numerical Simulation of Optoelectronic Devices (NUSOD), Copenhagen, 2017, pp. 169-170.

5. **(Conference Publication & Poster Presentation)** I. Begleris and P. Horak, "Stability of a Fiber Optical Parametric Oscillator With and Without a Seed Signal," in Frontiers in Optics 2017, OSA Technical Digest (online) (Optical Society of America, 2017), paper JW4A.89.

6. **(Conference Publication, Invited)** I. Begleris and P. Horak (2018) Multi-band nonlinear Schrödinger equation for efficient simulation of parametric optical amplifiers and oscillators. In International Conference on Transparent Optical Networks ICTON 2018

A.3 Published Software

1. I. Begleris and P. Horak. (2018, May 4). Compare-CNLSE v1.0 (Version v1.0). Zenodo. http://doi.org/10.5281/zenodo.1241107

2. I. Begleris and P. Horak. (2018, November 20). Computational-Nonlinear-Optics-ORC/Single-mode-FOPO: High resolution SM-FOPO with BNLSE (Version 2.1). Zenodo. http://doi.org/10.5281/zenodo.1492708

3. I. Begleris and P. Horak. (2019, May 4). Computational-Nonlinear-Optics-ORC/mm-fopo-1: First public release (Version 1.0). Zenodo. http://doi.org/10.5281/zenodo.2667311

Appendix B

Seven Band Generalised Nonlinear Schrödinger Equation

This appendix provides the explicit form of the 7-band GNLSE used for the simulations of Chapter 5.

The seven banded generalised nonlinear Schrödinger equation is found by:

$$\frac{dA_l}{dz} = \mathrm{i}\sum_{n\geq 2}\left(\frac{\beta_n}{n!}\left(\mathrm{i}\frac{\partial}{\partial t} - (l-3)\,\Omega\right)^n\right)A_l + \mathrm{i}\gamma_l\left(1 + \frac{\mathrm{i}}{\omega_l}\frac{\partial}{\partial t}\right)\left(N_l A_l + M_l\right), \tag{B.1}$$

where A_l is the envelope function of the pulse in band l, β_n the n^{th} Taylor expansion coefficients of the propagation contant β calculated at the central band ($l = 3$), γ_l and ω_l are the nonlinear coefficient and central frequency of each bandrespectively. N_l is the self-phase modulation and cross-phase modulation matrix found by:

$$\begin{pmatrix} N_0 \\ N_1 \\ N_2 \\ N_3 \\ N_4 \\ N_5 \\ N_6 \end{pmatrix} = \left(J_7 + \begin{pmatrix} 0 & H_5 & H_4 & H_3 & H_2 & H_1 & H_0 \\ H_7 & 0 & H_5 & H_4 & H_3 & H_2 & H_1 \\ H_8 & H_7 & 0 & H_5 & H_4 & H_3 & H_2 \\ H_9 & H_8 & H_7 & 0 & H_5 & H_4 & H_3 \\ H_{10} & H_9 & H_8 & H_7 & 0 & H_5 & H_4 \\ H_{11} & H_{10} & H_9 & H_8 & H_7 & 0 & H_5 \\ H_{12} & H_{11} & H_{10} & H_9 & H_8 & H_7 & 0 \end{pmatrix} \right) \cdot \begin{pmatrix} |A_0|^2 \\ |A_1|^2 \\ |A_2|^2 \\ |A_3|^2 \\ |A_4|^2 \\ |A_5|^2 \\ |A_6|^2 \end{pmatrix}, \tag{B.2}$$

where

$$H_l = \tilde{h}\left((l-6)\,\Omega\right) f_r - f_r + 1, \tag{B.3}$$

f_r is the fractional contribution of the Raman nonlinearity, $\tilde{h}(\omega)$ the Fourier transform of the Raman response function at frequency ω and J_7 is a 7×7 matrix of ones. M_l is the FWM matrix and is described by:

$$\begin{pmatrix} M_0 \\ M_1 \\ M_2 \\ M_3 \\ M_4 \\ M_5 \\ M_6 \end{pmatrix} = K \cdot \begin{pmatrix} A_0^* \\ A_1^* \\ A_2^* \\ A_3^* \\ A_4^* \\ A_5^* \\ A_6^* \end{pmatrix}, \tag{B.4}$$

where

$$K = \begin{pmatrix} 0, & 0, & q_{(1,1)}^{(5)}, \\ 0, & q_{(0,2)}^{(5,7)}, & q_{(0,3)}^{(7,4)}, \\ q_{(1,1)}^{(7)}, & q_{(0,3)}^{(8,5)}, & q_{(1,3)}^{(7,5)} + q_{(0,4)}^{(8,4)}, \\ q_{(1,2)}^{(7,8)}, & q_{(2,2)}^{(7)} + q_{(0,4)}^{(9,5)}, & q_{(1,4)}^{(8,5)} + q_{(0,5)}^{(9,4)}, \\ q_{(2,2)}^{(8)} + q_{(1,3)}^{(7,9)}, & q_{(2,3)}^{(7,8)} + q_{(0,5)}^{(10,5)}, & q_{(3,3)}^{(7)} + q_{(1,5)}^{(9,5)} + q_{(0,6)}^{(10,4)}, \\ q_{(2,3)}^{(8,9)} + q_{(1,4)}^{(7,10)}, & q_{(0,6)}^{(11,5)} + q_{(2,4)}^{(7,9)} + q_{(3,3)}^{(8)}, & q_{(1,6)}^{(10,5)} + q_{(3,4)}^{(7,8)}, \\ q_{(2,4)}^{(8,10)} + q_{(3,3)}^{(9)} + q_{(1,5)}^{(6,11)}, & q_{(2,5)}^{(7,10)} + q_{(3,4)}^{(8,9)}, & q_{(4,4)}^{(10)} + q_{(3,5)}^{(7,9)}, \end{pmatrix}$$

$$\begin{pmatrix} q_{(1,2)}^{(5,4)}, & q_{(2,2)}^{(4)} + q_{(1,3)}^{(5,3)}, & q_{(1,4)}^{(5,2)} + q_{(2,3)}^{(4,3)}, & q_{(3,3)}^{(3)} + q_{(2,4)}^{(4,2)} + q_{(1,5)}^{(5,1)} \\ q_{(2,2)}^{(5)} + q_{(0,4)}^{(7,3)}, & q_{(0,5)}^{(2,7)} + q_{(2,3)}^{(5,4)}, & q_{(0,0)}^{(4)} + q_{(2,4)}^{(5,3)} + q_{(0,6)}^{(7,1)} & q_{(2,5)}^{(5,2)} + q_{(3,4)}^{(4,3)} \\ q_{(1,4)}^{(7,4)} + q_{(0,5)}^{(8,3)}, & q_{(3,3)}^{(5)} + q_{(1,5)}^{(7,3)} + q_{(0,6)}^{(8,2)} & q_{(1,6)}^{(7,2)} + q_{(3,4)}^{(5,4)}, & q_{(4,4)}^{(4)} + q_{(3,5)}^{(5,3)} \\ q_{(2,4)}^{(7,5)} + q_{(1,5)}^{(8,4)} + q_{(0,6)}^{(9,3)}, & q_{(2,5)}^{(7,4)} + q_{(1,6)}^{(8,3)}, & q_{(4,4)}^{(5)} + q_{(2,6)}^{(7,3)}, & q_{(4,5)}^{(5,4)} \\ q_{(2,5)}^{(8,5)} + q_{(1,6)}^{(9,4)}, & q_{(3,5)}^{(7,5)} + q_{(2,6)}^{(8,4)}, & q_{(3,6)}^{(7,4)}, & q_{(5,5)}^{(5)} \\ q_{(2,6)}^{(9,5)} + q_{(4,4)}^{(7)}, & q_{(3,6)}^{(8,5)}, & q_{(4,6)}^{(7,5)}, & 0 \\ q_{(4,5)}^{(7,8)}, & q_{(5,5)}^{(7)}, & 0, & 0 \end{pmatrix}, \tag{B.5}$$

$$q_{(nm)}^{(p_1,p_2)} = A_n A_m \sum_{j=p_1,p_2} H_j. \tag{B.6}$$

Appendix C

Interpolation of Maximum Conversion Efficiency

This appendix shows results from an additional simulation which is used to invetsigate the insertion where the highest conversion efficiency occurs for the MM-FOPO model described in Chapter 6.

A linear fit is applied to the left hand side graphic of Figure C.1. The insertion of the signal with respect to the σ loss is:

$$\rho_{\mathrm{BS}}\left(SP\right) = 0.92SP + 9.82, R^2 = 0.994 \tag{C.1}$$

and

$$\rho_{\mathrm{PC}}\left(SP\right) = 0.93SP + 10.26, R^2 = 0.92 \tag{C.2}$$

for the BS and PC respectively.

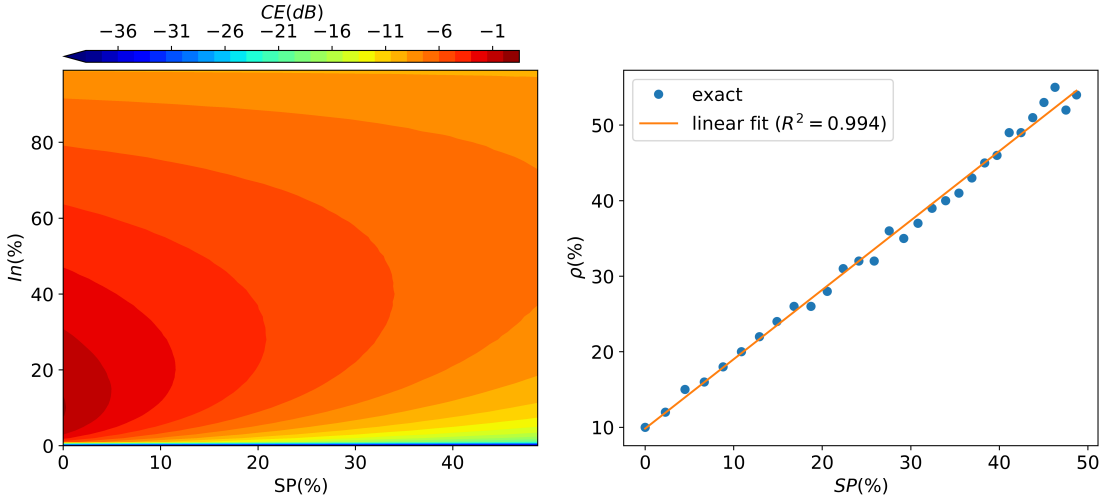

(a)

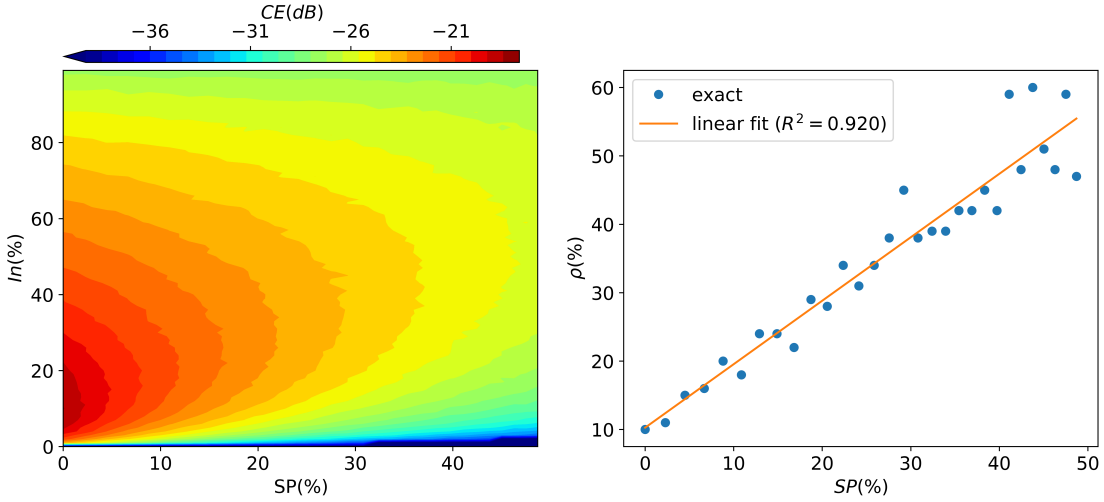

(b)

FIGURE C.1: On the left, the CE of the BS (a) and PC (b) processes with respect to the σ loss and signal insertion percentage. On the right hand side the exact and linearly interpolated insertion at maximum CE ι with respect to the σ loss. The signal wavelength is set to $\lambda_S = 1550\,\text{nm}$ which results in a PC and BS idlers of $\lambda_{\text{PC}} = 1552.5\,\text{nm}$ and $\lambda_{\text{BS}} = 1554.5\,\text{nm}$ respectively. The wavelengths and powers of the rest of the input waves are found in the Chapter 6.

Bibliography

[1] Ivan P Kaminow and Thomas L Koch. *Optical fiber telecommunications IIIB*. Elsevier Inc., 2012.

[2] D. J. Richardson. Filling the Light Pipe. *Science*, 330(6002):327–328, 2010.

[3] Michalis N. Zervas and Christophe A. Codemard. High power fiber lasers: A review. *IEEE Journal on Selected Topics in Quantum Electronics*, 2014.

[4] Rose Mary, Debaditya Choudhury, and Ajoy K. Kar. Applications of Fiber Lasers for the Development of Compact Photonic Devices. *IEEE Journal on Selected Topics in Quantum Electronics*, 20(5):72–84, 2014.

[5] Vartan Ter-Mikirtychev. *Fundamentals of Fiber Lasers and Fiber Amplifiers*. Springer, 2014.

[6] Sergei Popov. Fiber Laser Overview and Medical Applications. In F. J. Duarte, editor, *Tunable Laser Applications*, Optical science and engineering, pages 197–226. CRC Press, 3rd edition, 2016.

[7] Robert W Boyd. *Nonliner Optics*. Academic Press, San Diego, 2nd edition, 2003.

[8] Scott S H Yam, Michel E. Marhic, Youichi Akasaka, Katsuhiro Shimizu, Nobuhiko Kikuchi, and Leonid G. Kazovsky. Raman fiber oscillator as optical amplifier. *IEEE Photonics Technology Letters*, 16(6):1456–1458, 2004.

[9] Govind Agrawal. *Nonlinear Fiber Optics*. Academic Press, 5th edition edition, 2001.

[10] Michel E Marhic. *Fiber Optical Parametric Amplifiers, Oscillators and Related Devices: Theory, Applications, and Related Devices*. Cambridge University Press, 2008.

[11] Ioannis Begleris and Peter Horak. Efficiency and intensity noise of an all-fiber optical parametric oscillator. *J Opt Soc Am B*, 36(3):551–558, 2019.

[12] G Keiser. *Optical Fiber Communications - Second Edition*. McGraw-Hill series in electrical engineering: Communications and information theory. McGraw-Hill Higher Education, Singapore, 3rd edition, 1991.

[13] A D Ellis, N Mac Suibhne, D Saad, and D N Payne. Communication networks beyond the capacity crunch. *Philosophical Transactions of the Royal Society A: Mathematical, Physical and Engineering Sciences*, 374(2062):20150191, 2016.

[14] H Ishio, J Minowa, and K Nosu. Review and status of wavelength-division-multiplexing technology and its application. *Journal of Lightwave Technology*, 2(4):448–463, Aug 1984.

[15] K. Thyagarajan. Erbium-Doped Fiber Amplifiers. In Bishnu P. Pal, editor, *Guided Wave Optical Components and Devices*. Academic Press, 2006.

[16] D. J. Richardson, J. M. Fini, and L. E. Nelson. Space-division multiplexing in optical fibres. *Nature Photonics*, pages 354–362, 2013.

[17] Zhenhua Feng, Liang Xu, Qiong Wu, Ming Tang, Songnian Fu, Weijun Tong, Perry Ping Shum, and Deming Liu. Ultra-high capacity WDM-SDM optical access network with self-homodyne detection downstream and 32QAM-FBMC upstream. *Opt. Express*, 25(6):5951–5961, Mar 2017.

[18] S. Matsuo, K. Takenaga, Y. Sasaki, Y. Amma, S. Saito, K. Saitoh, T. Matsui, K. Nakajima, T. Mizuno, H. Takara, Y. Miyamoto, and T. Morioka. High-spatial-multiplicity multicore fibers for future dense space-division-multiplexing systems. *Journal of Lightwave Technology*, 34(6):1464–1475, March 2016.

[19] Katsunari Okamoto. *Fundamentals of Optical Waveguides*. Academic Press, 2nd edition, 2005.

[20] René Jean Essiambre, Miquel A. Mestre, Roland Ryf, Alan H. Gnauck, Robert W. Tkach, Andrew R. Chraplyvy, Yi Sun, Xinli Jiang, and Robert Lingle. Experimental observation of inter-modal cross-phase modulation in few-mode fibers. *IEEE Photonics Technology Letters*, 25(6):535–538, 2013.

[21] S. M. M. Friis, I. Begleris, Y. Jung, K. Rottwitt, P. Petropoulos, D. J. Richardson, P. Horak, and F. Parmigiani. Inter-modal four-wave mixing study in a two-mode fiber. *Optics Express*, 24(26):30338, 2016.

[22] Massimiliano Guasoni, Francesca Parmigiani, Peter Horak, Julien Fatome, and David J. Richardson. Intermodal Four-Wave Mixing and Parametric Amplification in Kilometer-Long Multimode Fibers. *Journal of Lightwave Technology*, 35(24):5296–5305, 2017.

[23] Nathalie Vermeulen, Christof Debaes, and Hugo Thienpont. The behavior of CARS in anti-Stokes Raman converters operating at exact Raman resonance. *IEEE Journal of Quantum Electronics*, 44(12):1248–1255, 2008.

[24] Ioannis Begleris and Peter Horak. Frequency-banded nonlinear Schrödinger equation with inclusion of Raman nonlinearity. *Optics Express*, 26(17):21527–21536, 2018.

[25] Francesco Poletti and Peter Horak. Description of ultrashort pulse propagation in multimode optical fibers. *Journal of the Optical Society of America B*, 25(10):1645–1654, 2008.

[26] David V. Plant Haiqing Wei. Fundamental equations of nonlinear fiber optics. In *Optical Modeling and Performance Predictions, Proceedings of SPIE*, 2004.

[27] Anders Höök. Influence of stimulated Raman scattering on cross-phase modulation between waves in optical fibers. *Optics Letters*, 17(2):115, 1992.

[28] Amnon Yariv. *Quantum electronics*. Wiley, 1989.

[29] Arti Agrawal B. M. Azizur Rahman. *Finite Element Modeling Methods for Photonics*. Artech House Books, 2013.

[30] Raman gain in glass optical waveguides. *Applied Physics Letters*, 22(6):276–278, 1973.

[31] R. Serber and C. H. Townes. Limits on Electromagnetic Amplification due to Complementarity. In C. H. Townes, editor, *Quantum Electronics*, page 233, 1960.

[32] COMSOL Inc. COMSOL Multiphysic. www.comsol.com, 2017.

[33] K. Jarrod Millman and Michael Aivazis. Python for scientists and engineers. *Computing in Science and Engineering*, 13(2):9–12, 2011.

[34] Travis E. Oliphant. *Guide to NumPy*. CreateSpace Independent Publishing Platform, USA, 2nd edition, 2015.

[35] Oleksandr Pavlyk, Denis Nagorny, Andres Guzman-Ballen, Anton Malakhov, Hai Liu, Ehsan Totoni, Todd A. Anderson, and Sergey Maidanov. Accelerating Scientific Python with Intel Optimizations. In *15th Python in Science Conf. (SciPy 2017)*, number July, pages 1–8, 2017.

[36] SymPy: symbolic computing in Python. *PeerJ Computer Science*, 3:e103, 2017.

[37] Andrew Collette. *Python and HDF5*. O'Reilly, 2013.

[38] The HDF Group. Hierarchical Data Format version 5. www.hdfgroup.org/HDF5, 1997-2019.

[39] John D. Hunter. Matplotlib: A 2D graphics environment. *Computing in Science and Engineering*, 9(3):90–95, 2007.

[40] Siu Kwan Lam, Antoine Pitrou, and Stanley Seibert. Numba: A LLVM-based Python JIT Compiler Siu. *LLVM-HPC2015*, pages 1–6, 2015.

[41] Stefan Behnel, Robert Bradshaw, Craig Citro, Lisandro Dalcin, Dag Sverre Seljebotn, and Kurt Smith. Cython: The Best of Both Worlds. *Computing in Science and Engineering*, 13(2):31–39, 2011.

[42] Message Passing Interface Forum. MPI: A Message-Passing Interface Standard. Technical report, Knoxville, TN, USA, 1994.

[43] Gael Varoquaux and Olivier Grisel. Joblib: running Python functions as pipeline jobs. joblib.readthedocs.org.

[44] Lisandro D. Dalcin, Rodrigo R. Paz, Pablo A. Kler, and Alejandro Cosimo. Parallel distributed computing using Python. *Advances in Water Resources*, 34(9):1124–1139, 2011.

[45] Torvalds, Linus. Git. git-scm.com, 2005-2018.

[46] GitHub. GitHub. github.com, 2008-2019.

[47] OpenAIRE and CERN. Zenodo. zenodo.org, 2019.

[48] Travis CI. Travis CI Documentation. docs.travis-ci.com, 2011-2018.

[49] W H Press, Saul A. Teukolsky, W T Vetterling, and Brian P. Flannery. *Numerical recipes in C the art of scientific computing*, volume 2nd ed. Cambridge University Press, New York, NY, USA, 1992.

[50] E. Fehlberg. Klassische Runge-Kutta-Formeln vierter und niedrigerer Ordnung mit Schrittweiten-Kontrolle und ihre Anwendung auf Wärmeleitungsprobleme. *Computing*, 6(1-2):61–71, 1970.

[51] J. R. Cash and Alan H. Karp. A variable order Runge-Kutta method for initial value problems with rapidly varying right-hand sides. *ACM Transactions on Mathematical Software*, 16(3):201–222, 1990.

[52] J. R. Dormand and P. J. Prince. A reconsideration of some embedded Runge-Kutta formulae. *Journal of Computational and Applied Mathematics*, 6(1):19–26, 1980.

[53] Yizhu Chen, Jinyong Leng, Hu Xiao, Tianfu Yao, Jiangming Xu, and Pu Zhou. High-efficiency all-fiber raman fiber amplifier with record output power. *Laser Physics Letters*, 15(8):085104, jun 2018.

[54] R. H. Stolen, J. E. Bjorkholm, and A. Ashkin. Phase-matched three-wave mixing in silica fiber optical waveguides. *Applied Physics Letters*, 24(7):308–310, 1974.

[55] D.W. Hewak, D. Brady, R.J. Curry, G. Elliott, C.C. Huang, M. Hughes, K. Knight, A. Mairaj, M.N. Petrovich, R.E. Simpson, and C. Sproat. Chalcogenide glasses for photonics device applications. In G S Murugan, editor, *Photonic Glasses and Glass-Ceramics*, pages 29–102. Research Signpost, 2010.

[56] Dong Wu, Li Shen, Haonan Ren, Joseph Campling, Thomas W. Hawkins, John Ballato, Ursula J. Gibson, and Anna C. Peacock. Net optical parametric gain

in a submicron silicon core fiber pumped in the telecom band. *APL Photonics*, 4:086102, 2019.

[57] Mostafa Taghizadeh, Mohammad Kazem Tavassoly, Mohsen Hatami, and Hassan Pakarzadeh. One-pump fiber optical parametric amplifiers: from the pulsed to the continuous wave operation. *Optical Engineering*, 57(5):1 – 6, 2018.

[58] S. Radic and C.J. McKinstrie. Two-pump fiber parametric amplifiers. *Optical Fiber Technology*, 9(1):7 – 23, 2003.

[59] Thomas Torounidis and Peter Andrekson. Broadband single-pumped fiber-optic parametric amplifiers. *IEEE Photonics Technology Letters*, 19(9):650–652, 2007.

[60] Raja Ahmad and Martin Rochette. High efficiency and ultra broadband optical parametric four-wave mixing in chalcogenide-PMMA hybrid microwires. *Optics Express*, 20(9):9572–9580, 2012.

[61] Xi Chen, An Li, Guanjun Gao, Abdullah Al Amin, and William Shieh. Characterization of fiber nonlinearity and analysis of its impact on link capacity limit of two-mode fibers. *IEEE Photonics Journal*, 4(2):455–460, 2012.

[62] Georg Rademacher, Stefan Warm, and Klaus Petermann. Analytical description of cross-modal nonlinear interaction in mode multiplexed multimode fibers. *IEEE Photonics Technology Letters*, 24(21):1929–1932, 2012.

[63] Yuzhe Xiao, Sami Mumtaz, René Jean Essiambre, and Govind P. Agrawal. Theory of intermodal four-wave mixing with random linear mode coupling in few-mode fibers. *Optics Express*, 22(26):32039–32059, 2014.

[64] Sami Mumtaz, René Jean Essiambre, and Govind P Agrawal. Nonlinear propagation in multimode and multicore fibers: Generalization of the Manakov equations. *Journal of Lightwave Technology*, 31(3):398–406, 2013.

[65] René Jean Essiambre, Miquel A. Mestre, Roland Ryf, Alan H. Gnauck, Robert W. Tkach, Andrew R. Chraplyvy, Yi Sun, Xinli Jiang, and Robert Lingle. Experimental investigation of inter-modal four-wave mixing in few-mode fibers. *IEEE Photonics Technology Letters*, 25(6):539–542, 2013.

[66] Stefano Signorini, Mattia Mancinelli, Massimo Borghi, Martino Bernard, Mher Ghulinyan, Georg Pucker, and Lorenzo Pavesi. Intermodal four-wave mixing in silicon waveguides. *Photonics Research*, 6(8):805–814, 2018.

[67] F. Parmigiani, P. Horak, Y. Jung, L. Grüner-Nielsen, T. Geisler, P. Petropoulos, and D. J. Richardson. All-optical mode and wavelength converter based on parametric processes in a three-mode fiber. *Optics Express*, 25(26):33602, 2017.

[68] Elham Nazemosadat, Abel Lorences-Riesgo, Magnus Karlsson, and Peter A Andrekson. Design of Highly Nonlinear Few-Mode Fiber for C-Band Optical Parametric Amplification Elham. *Journal of Lightwave Technology*, 35(14):2810–2817, 2017.

[69] Jonas Hansryd, Peter A. Andrekson, Mathias Westlund, Jie Li, and Per Olof Hedekvist. Fiber-based optical parametric amplifiers and their applications. *IEEE Journal on Selected Topics in Quantum Electronics*, 8(3):506–520, 2002.

[70] Huihui Cheng, Zhengqian Luo, Chenchun Ye, Yizhong Huang, Chun Liu, and Zhiping Cai. Numerical modeling of mid-infrared fiber optical parametric oscillator based on the degenerated FWM of tellurite photonic crystal fiber. *Applied Optics*, 52(3):525–529, 2013.

[71] T. Sylvestre, H. Maillotte, E. Lantz, and P. Tchofo Dinda. Raman-assisted parametric frequency conversion in a normally dispersive single-mode fiber. *Opt. Lett.*, 24(22):1561–1563, Nov 1999.

[72] Jean-Philippe Fève, Paul E Schrader, Roger L Farrow, and Dahv a V Kliner. Four-wave mixing in nanosecond pulsed fiber amplifiers. *Optics Express*, 15(8):4647–4662, 2007.

[73] Paul L Voss and Prem Kumar. Raman-noise-induced noise-figure limit for $\chi^{(3)}$ parametric amplifiers. *Optics Letters*, 29(5):445–447, 2004.

[74] Frédérique Vanholsbeeck, Philippe Emplit, and Stéphane Coen. Complete experimental characterization of the influence of parametric four-wave mixing on stimulated Raman gain. *Optics Letters*, 28(20):1960–1962, 2003.

[75] E. A. Golovchenko and A. N. Pilipetskii. Unified analysis of four-photon mixing, modulational instability, and stimulated Raman scattering under various polarization conditions in fibers. *Journal of the Optical Society of America B*, 11(1):92–101, 1994.

[76] Q. Lin, J. Zhang, P. M. Fauchet, and G. P. Agrawal. Ultrabroadband parametric generation and wavelength conversion in silicon waveguides. *Opt. Express*, 14(11):4786–4799, 2006.

[77] Q Lin, Oskar J Painter, and Govind P Agrawal. Nonlinear optical phenomena in silicon waveguides: modeling and applications. *Opt. Express*, 15(25):16604–16644, 2007.

[78] Ekaterina A. Zlobina, Sergey I. Kablukov, and Sergey A. Babin. Phase matching for parametric generation in polarization maintaining photonic crystal fiber pumped by tunable Yb-doped fiber laser. *Journal of the Optical Society of America B*, 29(8):1959–1966, 2012.

[79] M. E. Marhic, N. Kagi, T.-K. Chiang, and L. G. Kazovsky. Broadband fiber optical parametric amplifiers. *Optics Letters*, 21(8):573, 1996.

[80] J. S. Y. Chen, S. G. Murdoch, R. Leonhardt, and J. D. Harvey. Effect of dispersion fluctuations on widely tunable optical parametric amplification in photonic crystal fibers. *Optics Express*, 14(20):9491, 2006.

[81] M. E. Marhic, K. K.-Y. Wong, L. G. Kazovsky, and T.-E. Tsai. Continuous-wave fiber optical parametric oscillator. *Optics Letters*, 27(16):1439, 2002.

[82] Thomas Gottschall, Tobias Meyer, Michael Schmitt, Jürgen Popp, Jens Limpert, and Andreas Tünnermann. Four-wave-mixing-based optical parametric oscillator delivering energetic, tunable, chirped femtosecond pulses for non-linear biomedical applications. *Optics Express*, 23(18):23968, 2015.

[83] Masataka Nakazawa, Kazunori Suzuki, and Hermann A Haus. The Modulational Instability Laser-part I: Experiment. *IEEE Journal of Quantum Electronics*, 25(9):2036–2044, 1989.

[84] Masataka Nakazawa, Kazunori Suzuki, Hirokazu Kubota, and Hermann A. Haus. The Modulational Instability Laser-part II: Theory. *IEEE Journal of Quantum Electronics*, 25(9):2045–2052, 1989.

[85] S Saito, M Kishi, and M Tsuchiya. Dispersion-flattened-fibre optical parametric oscillator for wideband wavelength-tunable ps pulse generation. *Electronics Letters*, 39(1):2003, 2003.

[86] Yue Zhou, Kim K Y Cheung, Sigang Yang, P. C. Chui, and Kenneth K Y Wong. Ultra-Widely tunable, narrow linewidth picosecond fiber-optical parametric oscillator. *IEEE Photonics Technology Letters*, 22(23):1756–1758, 2010.

[87] G. Van der Westhuizen and J. Nilsson. Fiber Optical Parametric Oscillator for Large Frequency-Shift Wavelength Conversion. *IEEE Journal of Quantum Electronics*, 47(11):1396–1403, 2011.

[88] G K L Wong, S G Murdoch, R Leonhardt, and J D Harvey. High-conversion-efficiency widely-tunable all- fiber optical parametric oscillator. *Optics Express*, 15(6):2947–2952, 2007.

[89] Y. Q. Xu, S. G. Murdoch, R. Leonhardt, and J. D. Harvey. Widely tunable photonic crystal fiber Fabry-Perot optical parametric oscillator. *Optics Letters*, 33(12):1351, 2008.

[90] Y. Zhou, C. Zhang, P. C. Chui, and K. K. Y. Wong. A tunable s -plus l -band continuous-wave single-longitudinal-mode fiber-optical parametric oscillator. *IEEE Photonics Technology Letters*, 23(20):1451–1453, Oct 2011.

[91] Ekaterina A. Zlobina, Sergey I. Kablukov, and Sergey A. Babin. Tunable CW all-fiber optical parametric oscillator operating below 1 µm. *Optics Express*, 21(6):6777–6782, 2013.

[92] Ekaterina A. Zlobina, Sergey I. Kablukov, and Sergey A. Babin. All-PM CW fiber optical parametric oscillator. *Optics Express*, 24(22):25409, 2016.

[93] A Gershikov, E Shumakher, A Willinger, and G Eisenstein. Fiber parametric oscillator for the 2 μm wavelength range based on narrowband optical parametric amplification. *Optics Letters*, 35(19):3198, 2010.

[94] Gordon K P Lei, L. T. Lim, and M. E. Marhic. Continuous-wave fiber optical parametric oscillator with sub-MHz linewidth. *Optics Communications*, 306:17–20, 2013.

[95] S. Yang, X. Xu, Y. Zhou, K. K. Y. Cheung, and K. K. Y. Wong. Continuous-wave single-longitudinal-mode fiber-optical parametric oscillator with reduced pump threshold. *IEEE Photonics Technology Letters*, 21(24):1870–1872, Dec 2009.

[96] R Leonhardt Y Q Xu, S G Murdoch and J D Harvey. Raman-assisted continuous-wave tunable all-fiber optical parametric oscillator. *J Opt Soc Am B*, 26(7):1351–1355, jun 2009.

[97] C. J. S. de Matos, J. R. Taylor, and K. P. Hansen. Continuous-wave, totally fiber integrated optical parametric oscillator using holey fiber. *Opt. Lett.*, 29(9):983–985, May 2004.

[98] K. S. Yeo, F. R Mahamd Adikan, M. Mokhtar, S. Hitam, and M. A. Mahdi. Continuous wave tunable fiber optical parametric oscillator with double-pass pump configuration. *Applied Physics B: Lasers and Optics*, 110(3):353–357, 2013.

[99] Jianpeng Zhao, Bin Luo, Wei Pan, Lianshan Yan, Xihua Zou, Jia Ye, Hongna Zhu, Nianqiang Li, and Zhiyu Chen. Output characterization of a fiber optic parametric oscillator based on multiple four-wave mixing. *Applied Optics*, 54(26):7884, 2015.

[100] Wen Qi Zhang, Jay E. Sharping, Richard T. White, Tanya M. Monro, and Shahraam Afshar V. Design and optimization of fiber optical parametric oscillators for femtosecond pulse generation. *Optics Express*, 18(16):17294–17305, 2010.

[101] Erin S. Lamb, Simon Lefrancois, Minbiao Ji, William J. Wadsworth, X. Sunney Xie, and Frank W. Wise. Fiber optical parametric oscillator for coherent anti-Stokes Raman scattering microscopy. *Optics Letters*, 38(20):4154–4157, 2013.

[102] Ioannis Begleris and Peter Horak. Cascade simulations of unidirectional fiber optical parametric oscillators. In *Proceedings of the International Conference on Numerical Simulation of Optoelectronic Devices, NUSOD*, pages 169–170, Copenhagen, 2017.

[103] Ioannis Begleris and Peter Horak. Stability of a Fiber Optical Parametric Oscillator With and Without a Seed Signal. In *Frontiers in Optics 2017*, pages 3–4, 2017.

[104] Yongzhong Li, Liejia Qian, Daquan Lu, and Dianyuan Fan. Widely tunable femtosecond fiber optical parametric oscillator. *Optics Communications*, 267(2):491–497, 2006.

[105] Hangyu Bai, Xiong Yang, Yizhen Wei, and Shiming Gao. Broadband mid-infrared fiber optical parametric oscillator based on a three-hole suspended-core chalcogenide fiber. *Applied Optics*, 55(3):515, 2016.

[106] K. S. Yeo, M. H. Abu Bakar, F. R. Mahamd Adikan, and M. A. Mahdi. Widely tunable fiber optical parametric oscillators with idler removal filter. *IEEE Photonics Journal*, 9(1):1–9, Feb 2017.

[107] Cesar Jauregui, Alexander Steinmetz, Jens Limpert, and Andreas Tünnermann. High-power efficient generation of visible and mid-infrared radiation exploiting four-wave-mixing in optical fibers. *Optics Express*, 20(22):24957, 2012.

[108] Effect of idler absorption in pulsed optical parametric oscillators. *Optics Express*, 19(3):2815, 2011.

[109] Alexander Franzen. ComponentLibrary - vector graphics library for illustrations of optics experiments. www.gwoptics.org/ComponentLibrary/, 2006.

[110] Ekaterina A Zlobina, Sergey I Kablukov, and Sergey A Babin. High-efficiency CW all-fiber parametric oscillator tunable in 0.92-1 μm range. *Optics Express*, 23(2):833–838, 2015.

[111] Z Feng, C Li, S Xu, C Yang, S Mo, D Chen, M Peng, and Z Yang. Suppression of the low frequency intensity noise of a single-frequency yb3+-doped phosphate fiber laser at 1083 nm. *Laser Physics*, 24(6):065106, apr 2014.

[112] Richard H Byrd, Peihuang Lu, Jorge Nocedal, and Ciyou Zhu. A Limited Memory Algorithm for Bound Constrained Optimization. *SIAM Journal on Scientific Computing*, 16(5):1190–1208, 1995.